Understanding the Conformational Dynamics of the A_{2A} Adenosine Receptor by Single-Molecule Fluorescence

A Dissertation Presented for the

Doctor of Philosophy

Degree

The University of Tennessee, Knoxville

Shushu Wei

May 2024

ACKNOWLEDGEMENTS

First and foremost, I would like to express my sincere gratitude to my advisor, Dr. Rajan Lamichhane, for his invaluable guidance, support, and encouragement throughout my research.

Special thanks to my committee members: Dr. Barrera Olivares, Dr. Barry Bruce, Dr. Gladys Alexandre, and Dr. Jaan Mannik, for their valuable insights, feedback, and encouragement for my project. Also, the Special appreciation goes to Dr. Ed Wright in the BCMB department and Jaydeep Kolape in the Advanced Microscopy and Imaging Center for their technical support and patient guidance in utilizing the Mass Photometer and Transmission Electron Microscopy.

I am grateful to our collaborator, Dr. Matthew Eddy, and the members of his laboratory, particularly Naveen Thakur, Niloofar Gopal Pour, and Arka Prabha Ray, for their invaluable research support, which made this project possible. I also extend my thanks to Hugo Gutiérrez-de-Terán from Uppsala University for providing molecular dynamics simulation data.

I appreciate all my colleagues for their support and assistance throughout my research and life, including current and former lab members: Dr. Sriram Tiruvadi Krishnan, Dr. Ting Lui, Eugene Agyemang, Susmita Khanal, Alyssa Gonneville, and Asmita Chaudhary. Additionally, I would like to extend my gratitude to David Lohry from Dr. Fernandez's lab, as well as Justin Westerfield, Katherine Stefanski, and Yujie Ye from Dr. Barrera's lab, who helped us set up our lab at the beginning.

I would like to express my great appreciation to my friend Alyssa Ward from Dr. Barrera’s lab. Not only for her brilliant inspiration during the single molecular study and her professional guidance with the Mass Photometer and Transmission Electron Microscopy, but also for her warm and generous heart, which has helped and inspired me constantly.

Additionally, I extend my heartfelt gratitude to Alyssa's family, Randy Ward, Teresa Ward, and Chynna Ward, whose care and affection have made me feel truly at home.

Furthermore, I am grateful for my friend, Dr. Phoebe Vance, for her patience, encouragement, and wise advice along my life's journey, helped me become more confident and mature as a person.

I am deeply thankful to my parents and grandparents for their unwavering love and support, which has given me the confidence and support to complete my studies.

Lastly, I want to recognize the supportive environment fostered by the BCMB department at the University of Tennessee. Moreover, I am thankful for the grant from NIH R35GM142946 and the start-up funds from the College of Arts and Sciences, University of Tennessee, Knoxville, which have enabled the progress of my project.

ABSTRACT

G protein-coupled receptors (GPCRs) are one of the largest transmembrane receptor families. The wide expression and diverse signal transduction functions make them an ideal target for characteristic drug design. The A_{2A} adenosine receptor (A_{2A}AR), a representative of class A GPCRs, has been extensively used to reveal the structural information of class A GPCRs. As a purinergic receptor, A_{2A}AR is activated by adenosine in the human body, triggering cyclic adenosine monophosphate (cAMP) and immunosuppression pathways. A_{2A}ARs are highly expressed in the brain and are crucial in regulating glutamate and dopamine release. As a result, the A_{2A}AR became a potential therapeutic target for treating neurodegenerative diseases. In recent years, A_{2A}ARs have been identified in specific cardiac cells where they regulate myocardial oxygen consumption and coronary blood flow. Accordingly, the A_{2A}AR-targeted drug design and optimization has become increasingly valued. However, the dynamic nature of A_{2A}AR structures poses challenges in drug design. Therefore, the study of structural dynamics provides valuable information for ligand identification and drug prediction. In this work, we used total internal reflection fluorescence (TIRF) imaging to visualize the real-time dynamics of ligand binding and activation of the A_{2A}AR at the molecular level. We observed reversible and sequential dynamic behaviors in A_{2A}AR transmembrane helix VII (TM VII). Furthermore, the constitutively activating mutations (CAMs) didn't show the ligand-specific conformational dynamics like the wild type A_{2A}AR, but CAMs and the Mini-Gs shifted conformational equilibrium towards the intermediate state, while D52N, a constitutively inactivating mutation, had the opposite effect. We also successfully

stabilized the A_{2A}ARs in native membrane environment and incorporated them into nanodiscs using the polymers styrene maleic acid (SMA) and di-isobutylene maleic acid (DIBMA). This allowed us to observe more transition events between active-like conformational states between transmembrane helices IV and VI upon agonist and Mini-G_S binding. Overall, this work has filled the gap in understanding A_{2A}AR structural dynamics at the single-molecule level, emphasizing the significance of intermediate states in A_{2A}AR dynamics and paving the way for future A_{2A}AR-targeted drug design strategies.

TABLE OF CONTENTS

LIST OF TABLES

LIST OF FIGURES

CHAPTER I. INTRODUCTION

1.1 G Protein-coupled receptor overview

G protein-coupled receptors (GPCRs) belong to the largest family of membrane proteins with seven transmembrane α helical structures. On the basis of their structural homology and functional similarity, GPCRs have been classified into six primary groups, including rhodopsin-like receptors (Class A), secretin-like receptors (Class B), metabotropic glutamate receptors (Class C), fungal mating pheromone receptors (Class D), cyclic adenosine monophosphate receptors (Class E), and frizzled and smoothened receptors (Class F) (**Figure 1**) [1-3]. What draws significant attention are the GPCRs expressed in vertebrates, compressing Class A, B, C, and F, encoding more than 1000 GPCRs [4, 5]. Since the GPCR proteins are widely distributed and functionally significant in the human body, they have been considered effective therapeutic targets for various diseases [3, 6].

Among the GPCR classes, Class A GPCRs have the largest number of known members, providing numerous potential drug targets. Among these, the most representative and well-studied are β1-adrenoceptor (β1AR), β2-adrenoceptor (β2AR), and A_{2A} adenosine receptor (A_{2A}AR) [7, 8]. Structurally, Class A GPCRs typically contain short and disorder N-terminal regions [9]. Class B GPCRs have also been studied as promising targets for various diseases, such as neurodegeneration, cardiovascular, metabolic disease (diabetes), and psychiatric disorders [3]. Through structural diversity and phylogeny analysis, Class B GPCRs are categorized into two subclasses: secretin and adhesion. In the secretin subclass, a featured structure is the large N-terminal extracellular domain (ECD), which involves interactions with peptide ligands [10-12].

Class C GPCRs play crucial roles in various physiological processes, including synaptic transmission, gustatory sensation, and the regulation of calcium homeostasis. The distinguishing future of this classification is the ECD which initiates the homo- or hetero-dimerization. Structurally, the ECD is further divided into a cysteine-rich domain (CRD) and a ligand-binding domain (LBD), with the orthosteric binding site located within a Venus flytrap domain (VFTD), responsible for the ligand recognition and binding [13-15]. The exploration of Class F GPCRs has gained increasing attention in recent years. These receptors include the Frizzleds (FZD1-10) and Smoothened (SMO) two subclasses [16, 17]. Notably, only the latter subclass has been currently confirmed as a drug target [18]. Structurally, these receptors contain a CRD accompanied by a linker domain (LD) on the ECD. The Class F GPCRs play important roles in regulating central processes, such as proliferation, differentiation, cellular polarity, and migration during embryonic development and adult tissue homeostasis [19]. As for the Class D and Class E GPCRs, they belong to the non-mammalian category, and only extremely limited structures have been revealed [20]. The Class D GPCRs are expressed in fungi, where they regulate survival and reproduction [20, 21]. On the other hand, the Class E GPCRs are cAMP receptors from slime molds [22] (**Figure 1**).

1.2 G Protein-coupled receptor signaling

Based on the types of stimuli, the human GPCRs can be classified into 2 different types. Most of them are non-sensory, also known as endoGPCRs, responding to endogenous signals, such as lipids, peptides, neurotransmitters, and nucleotides, which

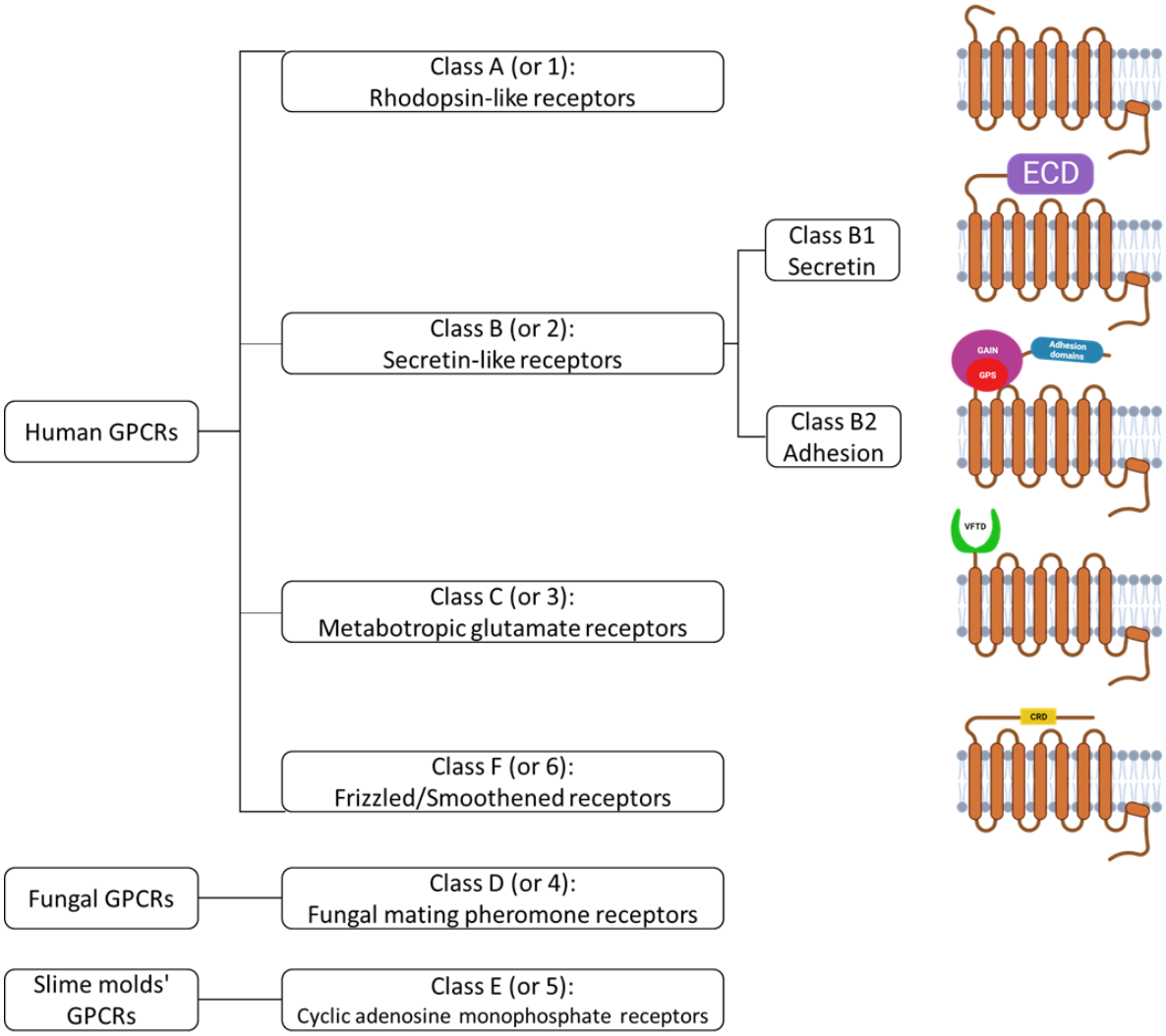

Figure 1. Classification and structural characterization schemes of GPCRs.

This scheme illustrates the classification of the GPCRs superfamily. Based on the expression system, classes A, B, C, and F are expressed in humans, while Class D GPCRs are exclusively expressed in fungi, and Class E is expressed in slime molds. The structural representation of human GPCRs' classes is depicted in this figure. It is important to note that the identified crystal structures of Class D and E GPCRs are limited, and this limitation prevents a comprehensive conclusion regarding the structural schemes.

are referred to as endoGPCRs [23]. Chemosensory GPCRs (csGPCRs), on the other hand, respond to taste, smell, pheromones, and other external stimuli [24]. The ligands of GPCR are generally categorized as agonists, antagonists, and inverse agonists, each eliciting distinct biological responses upon binding. Due to their dynamic structural characteristics, GPCRs have been shown to exhibit a conformational equilibrium between their active and inactive states [25]. Agonists can either induce or stabilize the active state of the receptor. In contrast, antagonists, including natural antagonists, do not exhibit effects on their own but can block the access of other ligands. Inverse agonists, however, reduce the constitutive activity of the receptor [26] (**Figure 2**). Consequently, comprehending the structural dynamics of GPCRs is imperative for advancing basic science studies and facilitating rational drug design.

GPCR signaling is a complicated process, inducing the activation of a huge diversity of signaling pathways that regulate many different cellular functions. The signaling of GPCRs communicates through different transducers, mainly involving β-arrestins, heterotrimeric G proteins, and GPCR kinases. During the GPCR signaling process, ligands interact with an extracellular ligand binding site, resulting in conformational change throughout the GPCR across the cell membrane to induce diverse intracellular responses. This conformational shift can initiate an interaction between the GPCR and heterotrimeric guanine nucleotide-binding proteins (G proteins). This promotes the exchange of GTP for GDP, leading to the dissociation of Gα with Gβγ subunits that initiate downstream signaling and finally result in various physiological responses of tissues and organisms [27, 28] (**Figure 3**).

1.3 G Protein-coupled receptor and drug design

The superfamily of GPCRs plays a pivotal role in over 80% of plasma membrane signal transduction processes. As the largest protein superfamily in the human genome, more than 800 GPCRs have been identified, predominantly expressed in the central nervous system (CNS) where they mediate crucial functions in various neuronal activity [29, 30]. In addition, except for their involvement in neurodegenerative diseases related to neuronal function, GPCRs also contribute significantly to the treatment of cancer and inflammatory conditions, establishing them as promising therapeutic targets for drug design. The development and optimization of GPCR-targeted drugs rely heavily on understanding their structural details and conformational dynamics [31]. Currently, approximately 35% of FDA-approved drugs target GPCRs, underscoring their substantial pharmaceutical relevance [32].

Although the GPCRs are the focal point for target drug design, more than half of the non-sensory GPCRs, especially orphan GPCRs lacking known endogenous ligands, remain largely unexplored in the clinical study [33]. Hence, revealing the structural properties and exploring the pharmacology and functions of orphan GPCRs could contribute to the discovery of unexpected targets in the future for treating various disease. Furthermore, in recent times, the trend in GPCR-targeted drug discovery leans towards searching and designing drugs with greater selectivity than existing ones [33]. This evolving trend indicates that GPCRs as not only significant in current drug design but also as a frontier for the discovery of highly specific therapeutic treatments.

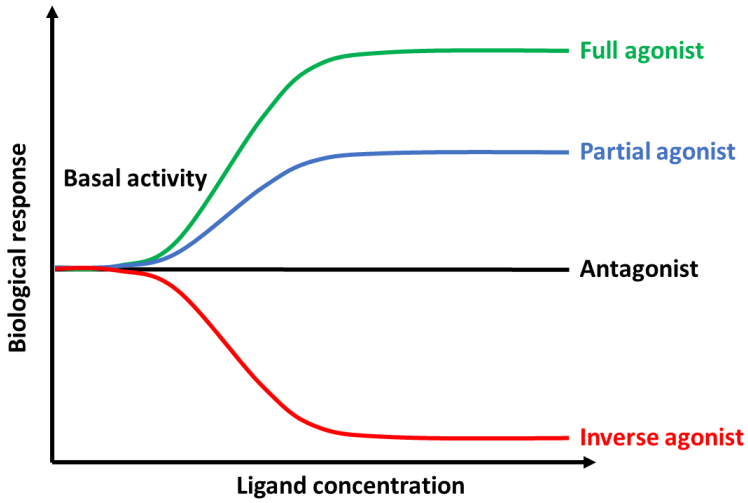

Figure 2. Functional responses of different GPCR ligands.

The full agonist (Green) and partial agonist (Blue) induce a positive biological response of GPCR. The inverse agonist induces a negative biological response. The antagonist (Black) won't alter the biological response, but it can block the access of other ligands.

Figure 3. A scheme of GPCRs signaling pathway.

(A) Inactivated GPCR and G protein heterotrimer. (B) Ligand binding stimulates GPCR, causing a conformational change and interaction with Gα. GDP is replaced by GTP, inducing G protein activation. (C) GTP-bound Gα separates from βγ sub-unites and interacts with the protein effector, leading to the production of the second messenger by the effector. (D) GTP hydrolysis into GDP, and the GPCR undergo the phosphorylated by GRK. (E). GDP-bound Gα reassemble with βγ subunit, returning the G protein to the inactive state. β-arrestin interacts with the phosphorylated GPCR, leading to GPCR internalization, followed by degradation, or recycling back to the plasma membrane.

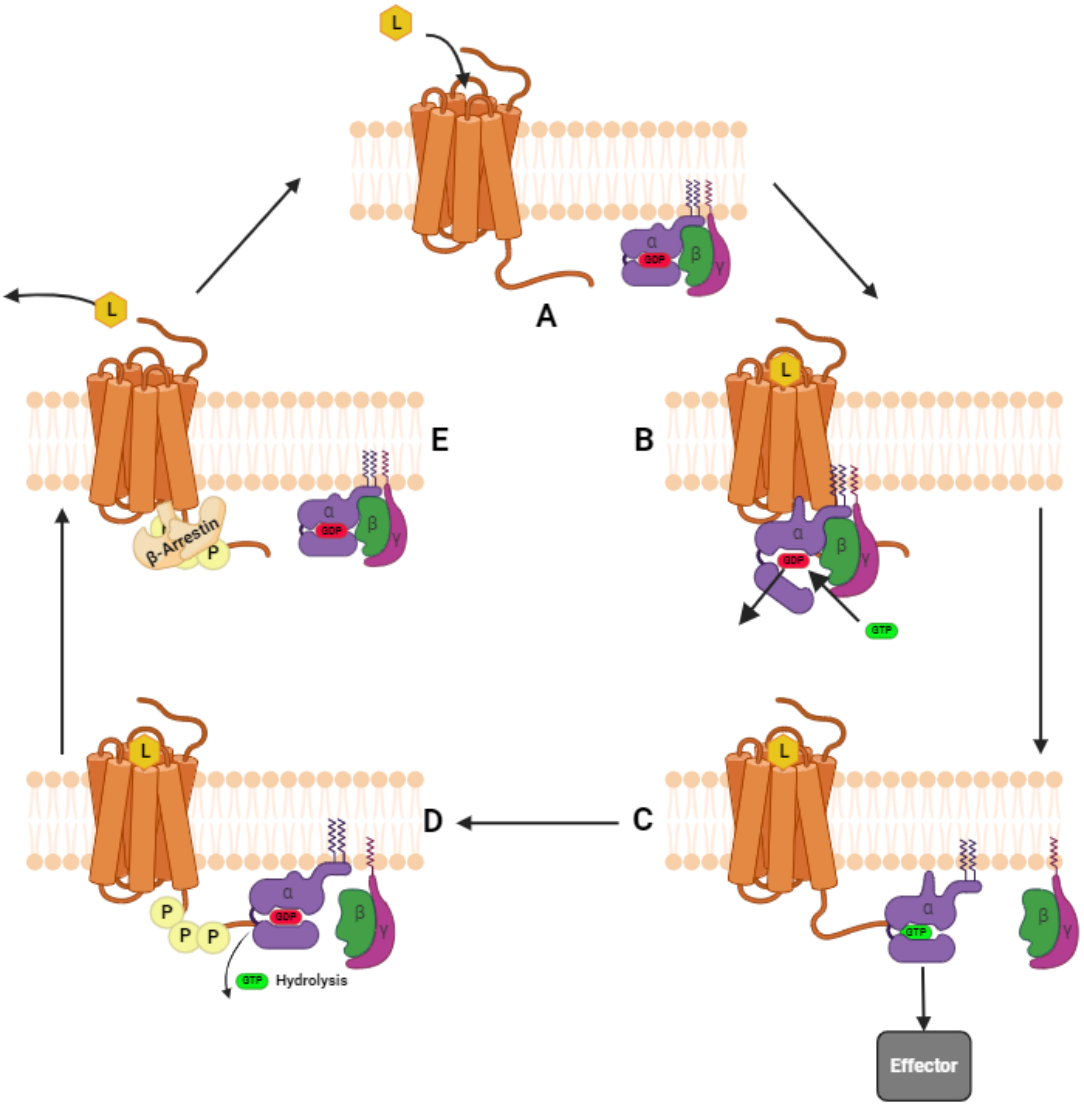

Figure 3. A Scheme of GPCRs signaling pathway.

1.4 Adenosine receptors

Cell surface receptor adenosine receptors (ARs) belong to the Class A GPCR family, comprised of four subtypes: A_1, A_{2A}, A_{2B}, and A_3, each distinguished by unique encoded genes. Responsive primarily to the key neuromodulator adenosine, ARs can influence diverse tissues and cell types throughout the human body [34]. And because of this feature, ARs are considered potential targets in a wide range of diseases, encompassing arrhythmia, ischemia, sleep disorders, pain, dementia, Parkinson's disease, renal failure, asthma, type 2 diabetes, glaucoma, inflammation, and cancer [35-37].

Within the four subtypes of adenosine receptors (ARs), A_1Rs and A_3Rs interact with Gi proteins, leading to the inhibition of adenylyl cyclase (AC) and subsequently reduced cyclic AMP (cAMP). In some cases, A_1Rs interact with Go proteins. On the contrary, most of the A_2Rs are associated with Gαs (Gs) proteins, leading to the activation of the AC and cAMP production (**Figure 4**) [38]. Additionally, subtypes of the A_2R, distinguished by adenosine binding affinity, are categorized as high-affinity (A_{2A}AR) or low-affinity (A_{2B}AR) [39]. In terms of expression and localization, A_{1A}ARs, A_{2A}ARs, and A_{3A}Rs show slight differences. The A_1Rs and A_2Rs are widely distributed in various tissues throughout the human body, including the brain, heart, stomach, bladder, liver, and adipose tissue [40]. By contrast, The A_3Rs which have the lowest affinity to the adenosine, show higher expression in the lung and liver [37]. On the other hand, unlike the A_1Rs and A_3Rs, the A_2Rs are predominantly expressed in the brain, especially the striatum. The A_2Rs have also been identified with lower expression concentrations in the

cerebral cortex and hippocampus [41]. Compared with A_{2B}ARs, A_{2A}AR is also present in the periphery immune cells, blood platelets, blood arteries, and vasculature. Although the expression of A_{2A}ARs in these tissues is not as high as in the brain, it still plays crucial roles and serves as a potential drug target in various tissues [35, 36].

1.5 A_{2A} Adenosine receptor

My Ph.D. research primarily centered on the A_{2A} adenosine receptor (A_{2A}AR). It is a seven-transmembrane helix membrane protein consisting of 412 amino acids, serving as a representative Class A GPCR (**Figure 5**). Over the years, its crystal structures have been extensively studied over the years for targeted drug prediction and design. As an adenosine receptor, A_{2A}AR is activated by the endogenous ligand adenosine to modulate various physiological activities [42]. The most well-established signaling pathway associated with A_{2A}AR involves the activation of the cAMP/ protein kinase A (PKA) pathway. During the A_{2A}AR-mediated signaling, the adenosine binding to A_{2A}AR stimulates the coupling of $G\alpha_S$, triggering the synthesis of cyclic adenosine monophosphate (cAMP). This cascade leads to the activation of PKA and multiple downstream targets, influencing various immunosuppressive pathways (**Figure 4**) [39, 42]. A_{2A}AR is now at the center stage for increasing the therapeutic methods for various clinical symptoms. The expression of A_{2A}AR in the vasculature and brain plays important roles in regulating inflammatory, glutamate, and dopamine release. Besides, different A_{A2}AR ligands are used to study the therapeutic potentials for drug abuse disorders [42]. In recent years, A_{2A}AR has been highlighted for targeted drug discovery for many neurodegenerative diseases, such as

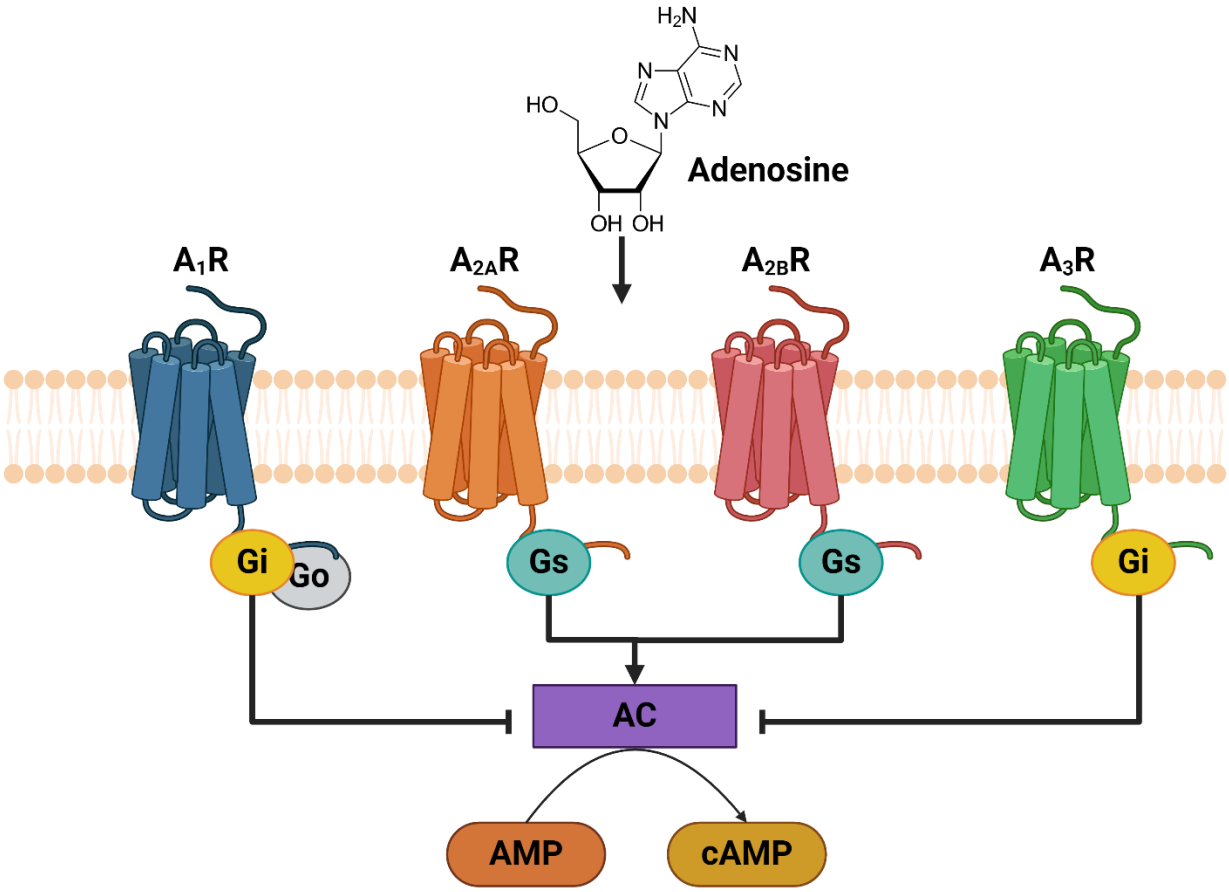

Figure 4. Adenosine receptors classification and signaling.

Adenosine receptors are classified into four subtypes: A_1, A_{2A}, A_{2B}, and A_3. Adenosine, as an agonist stimulus for adenosine receptors, is produced both intracellularly and extracellularly. During activation, A_1AR and A_3AR interact with the Gi protein, leading to the inhibition of adenylyl cyclase (AC). On the other hand, the activation of A_{2A}AR and A_{2B}AR induces adenylyl cyclase activation, resulting in cAMP production and subsequent activation of various downstream pathways.

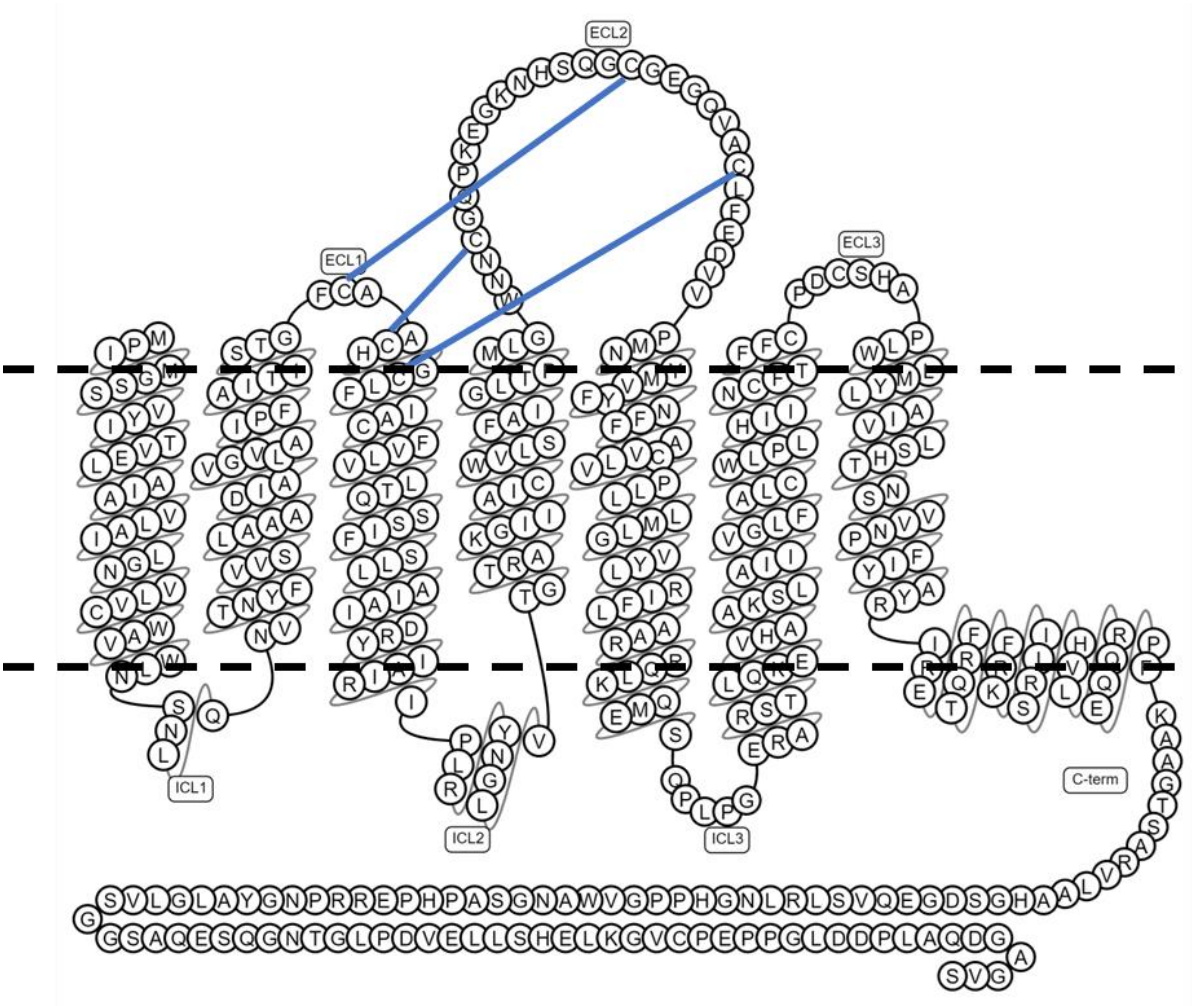

Figure 5. A_{2A}AR secondary structure.

The human A_{2A}AR has a total of 412 amino acids. Its secondary structure incudes seven transmembrane helices, accompanied by a short helix VIII and a solubilized C-terminal. The transmembrane area is represented by black dash lines, and disulfide bonds are highlighted in blue.

Parkinson’s disease (PD), Alzheimer's disease (AD), Depression, and anxiety disorder [43]. Excitingly, in 2019, the very first A_{2A}AR-targeted drug, Istradefylline which is a treatment for PD, has been proved by the US Food and Drug Administration (FDA) [44]. It exhibits neuroprotective properties in the treatment of motor symptoms and mitigating the adverse effects of antiparkinsonian drugs. Most important is that istradefylline is a nondopaminergic drug, and the clinical trials exhibit better effects and less severe side effects compared with the traditional levodopa/carbidopa (L/C) treatment for PD [45, 46].

1.6 Structural complexity of A_{2A} Adenosine Receptor

Although A_{2A}AR has excellent potential to become a multifunctional clinical therapeutic target, the conformational flexibility of GPCR and its complicated relationship for receptor-receptor and receptor-effector interactions is a nonnegligible barrier for GPCR-targeted drug discoveries. A_{2A}AR’s function depends critically on its ability to transition among distinct conformations [43, 47]. Therefore, understanding the effects of different ligands, the interaction between residues, and G protein binding on the conformational change of A_{2A}AR is crucial for related drug developments.

As a transmembrane GPCR, the dynamic and unstable nature poses a significant challenge to the structural identification and study of A_{2A}AR. The first crystal structure of A_{2A}AR with its interaction of the antagonist, ZM, was revealed by Jaakola in 2008 [48]. Subsequently, over the past decade, with advancements in crystallization strategies, more than 30 crystal structures of A_{2A}AR with various ligands and binding partners, such as mini Gs, an engineered GTP binding domain of the Gα subunit [35]. Additionally, A_{2A}AR is unique among GPCRs, with structures reported for more than just inactive and

active states [35]. The crystallography revealed both inactive structures complexed with an antagonist and intermediate-active structures bound to an agonist at the orthosteric site, with mini Gs observed at the intracellular site (**Table 1**). Based on existing crystal structures of A_{2A}AR, it is evident that, during activation, the transmembrane helices VI (TM VI) and VII (TM VII) undergo the most significant conformational changes. Specifically, TM VII moves away from the helix bundle, while TM VII moves in the opposite direction (**Figure 6**) [49]. And the diverse conformations of these conformational states also indicate the complexity of A_{2A}AR dynamics [49, 50]. 19F NMR has now provide an efficient method to characterize the conformational states in A_{2A}AR when interacting with different ligands and partners, providing a high-resolution overview of A_{2A}AR dynamics [51, 52]. Despite this, the molecular-level dynamic details are still missing. So, we employed single-molecule total internal reflection fluorescent (TIRF) microscopy to fill in the blanks and reveal A_{2A}AR dynamics at the molecular level.

1.7 Constitutively mutants of A_{2A}AR

Dring the transmembrane signaling process, the transmembrane structure of GPCRs undergoes a series of conformational changes, eliciting intracellular responses. Structural studies have highlighted some motifs with conserved sequences within Class A GPCRs, including the sodium binding pocket, PIF, CWxP, NPxxY, and DRY motifs [28, 53]. These conserved motifs, although structurally distinct, link the bottom of the orthosteric ligand binding site to the intracellular G protein binding pocket in a three-dimensional dimension [28, 54]. Typically, any alteration or disruption of these motifs

Table 1. Crystal structures of A_{2A}AR.

PDB ID	Conformational state	Ligand	Ligand type	Binding partner	Resolution (Å)
3EML	Inactive	ZM241385	Antagonist	No	2.6
3PWH	Inactive	ZM241385	Antagonist	No	3.3
3REY	Inactive	XAC	Antagonist	No	3.3
3RFM	Inactive	Caffeine	Antagonist	No	3.6
4EIY	Inactive	ZM241385	Antagonist	No	1.8
3UZA	Inactive	T4G	Antagonist	No	3.3
3UZC	Inactive	T4G	Antagonist	No	3.3
3VG9	Inactive	ZM241385	Antagonist	Fab2823	2.7
3VGA	Inactive	ZM241385	Antagonist	Fab2824	3.1
5IU4	Inactive	ZM241385	Antagonist	No	1.7
5IU7	Inactive	6DY	Antagonist	No	1.9
5IU8	Inactive	6DZ	Antagonist	No	2.0
5IUA	Inactive	6DX	Antagonist	No	2.2
5IUB	Inactive	6DVD	Antagonist	No	2.1
5K2A	Inactive	ZM241385	Antagonist	No	2.5
5K2B	Inactive	ZM241385	Antagonist	No	2.5
5K2C	Inactive	ZM241385	Antagonist	No	1.9
5K2D	Inactive	ZM241385	Antagonist	No	1.9
5JTB	Inactive	ZM241385	Antagonist	No	2.8
5UIG	Inactive	8D1	Antagonist	No	3.5
5UVI	Inactive	ZM241385	Antagonist	No	3.2
5MZP	Inactive	Caffeine	Antagonist	No	2.1
5MZJ	Inactive	Theophylline	Antagonist	No	2.0
5N2R	Inactive	PSB36	Antagonist	No	2.8
5NLX	Inactive	ZM241385	Antagonist	No	2.1
5NM2	Inactive	ZM241385	Antagonist	No	2.0
5NM4	Inactive	ZM241385	Antagonist	No	1.7
6AQF	Inactive	ZM241386	Antagonist	No	2.5
6GT3	Inactive	AZD4635	Antagonist	No	2.0
6PS7	Inactive	ZM241385	Antagonist	No	1.9
6ZDR	Inactive	ZM241385	Antagonist	No	1.9
6ZDV	Inactive	ZM241385	Antagonist	No	2.1
7T32	Inactive	ZM241386	Antagonist	Fab	3.4
8CIC	Inactive	ZM241386	Antagonist	No	2.1
8CU6	Inactive	LJ-4517	Antagonist	No	2.8
8CU7	Inactive	LJ-4517	Antagonist	No	2.1
3QAK	Active like	UK-432097	Antagonist	No	2.7
2YDO	Active like	Adenosine	Agonist	No	3.0
2YDV	Active like	NECA	Agonist	No	2.6
4UG2	Active like	CGS21680	Agonist	No	2.6

Table 1 (continue). Crystal structures of A_{2A}AR.

PDB ID	Conformational state	Ligand	Ligand type	Binding partner	Resolution (Å)
4UHR	Active like	CGS21680	Agonist	No	2.6
8WDT	Active like	PhotoNECA	Agonist	Fab94-1	3.3
5G53	Active	NECA	Agonist	Mini-Gs	3.4
6GDG	Active	NECA	Agonist	Mini-Gs	4.1

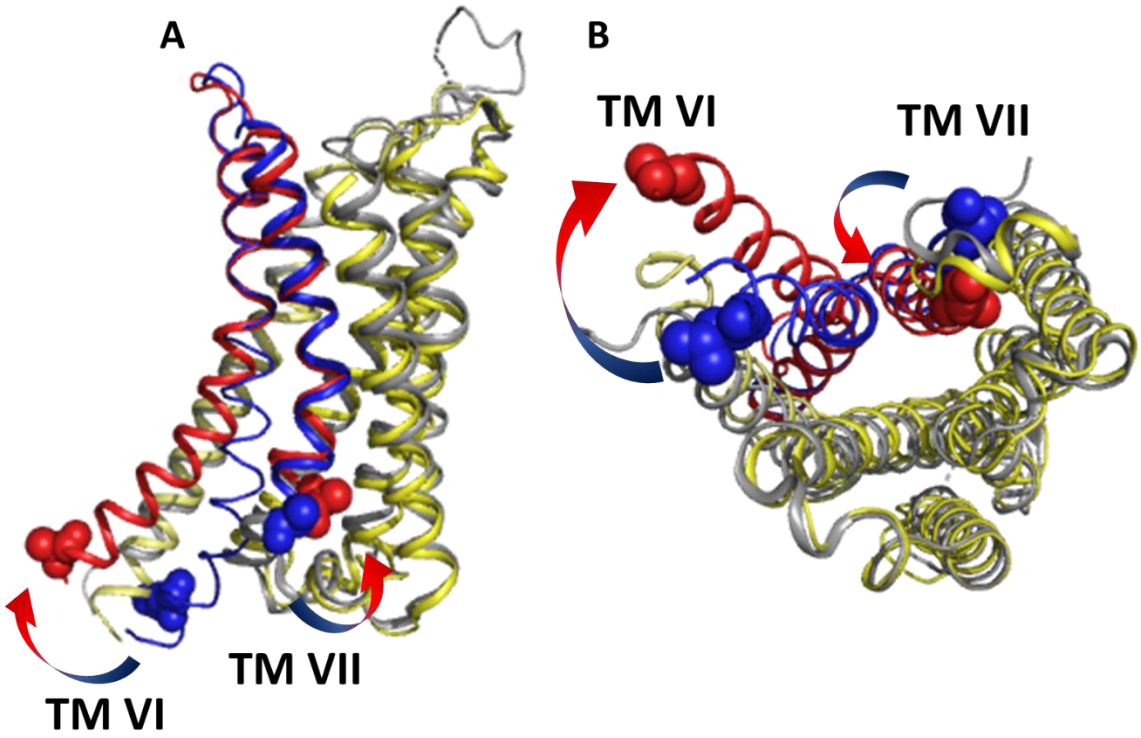

Figure 6. A_{2A}AR crystal structures during the activation.

(A) The front views show the overlay of A_{2A}AR in its fully active state (yellow with red TM VI and TM VII, PDB 6gdg) and inactive state (gray with red TM VI and TM VII, PDB 3eml) crystal structures. (B) The bottom views depict A_{2A}AR crystal structures. During the activation of A_{2A}AR, significant conformational changes were revealed in TM VI and TM VII. TM VI moves away from the protein bundle, while TM VII moves toward the bundle.

result in the alternating activity of the receptor. Several residues within these motifs of Class A GPCRs have been shown to modify constitutive activities, highlighting their significance in the Class A GPCR targeted drug. Notably, in the case of A_{2A}AR, structural alterations which relate to the conserved motives play a crucial role in drug design efforts targeting attentional diseases, influencing both therapeutic efficacy and the occurrence of side effects [55].

Currently, the impact of some A_{2A}AR mutations, such as I92N, R291Q, and D52N, located in different conserved motifs, has been investigated on receptor dynamics [49, 56]. In 2022, Cui and his group revealed that the I92N mutation forms hydrogen bonds with surrounding residues in the agonist bound A_{2A}AR by crystallography and the MD simulation. These interactions help to maintain the intermediate structure of A_{2A}AR when in the absence of G protein [57]. The study of residue R291 in A_{2A}AR was limited, but it has been reported that positively charged R291 residue in A_{2A}AR interacts with negatively charged phospholipid headgroups [58]. In this case, the single residue mutation R291Q is predicted to decrease the TM VII-membrane interaction and increase the A_{2A}AR basal activity correspondingly [56]. In 2017, White and Eddy reported that the agonist-bound structures of another human A_{2A}AR mutant, D52N, disrupt allosteric sodium effects. This mutation suggests a possibility of thermal stability enhancement of A_{2A}AR. However, it is noteworthy that A_{2A}AR D52N demonstrated no cAMP accumulation upon agonist stimulation [59]. While these mutants have been revealed to alter the G protein signaling, the detailed dynamic information remains unclear. Therefore, examining the conformational dynamics of TM VII at the single-molecule level in these A_{2A}AR mutants

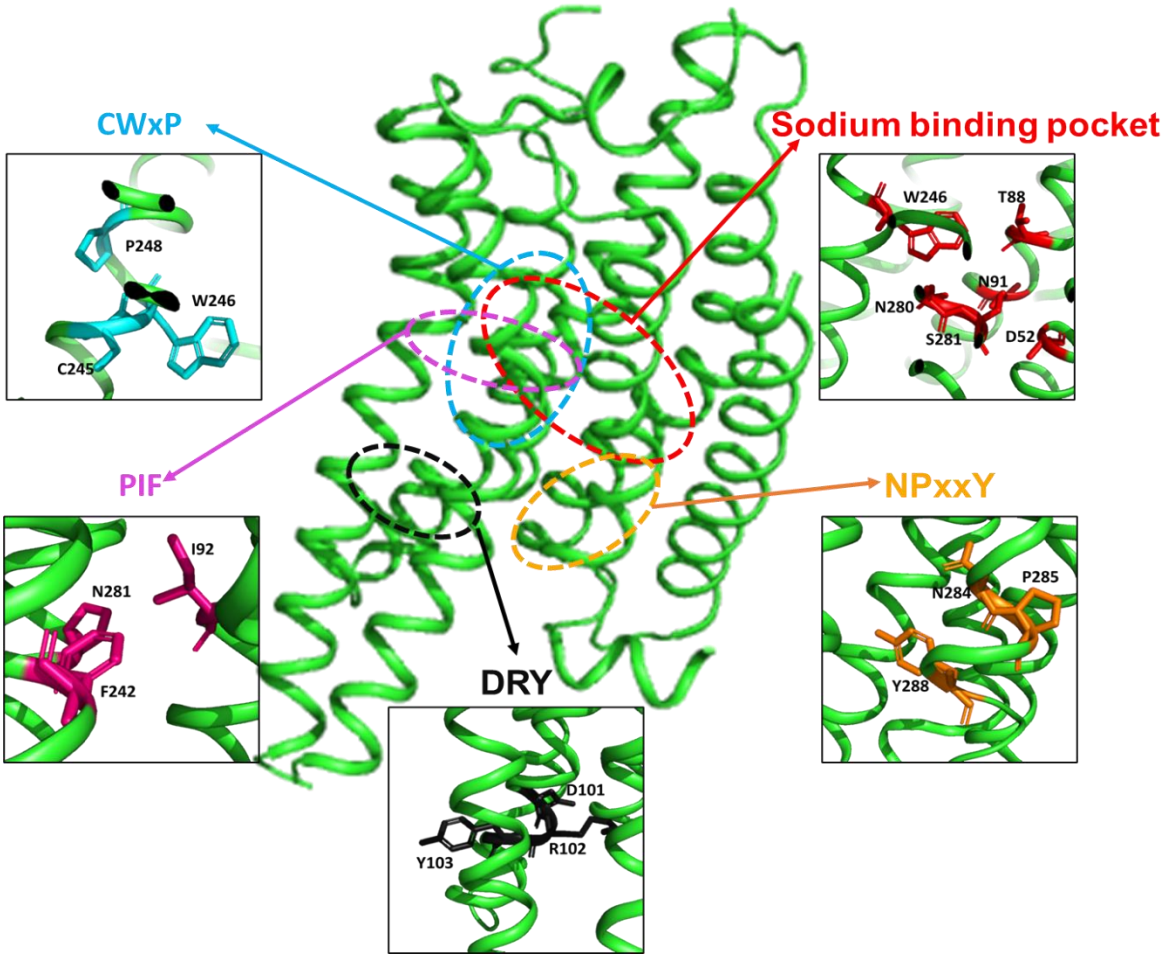

Figure 7. Class A GPCR conserved key motifs.

The Class A GPCRs have conserved motifs, and this figure illustrates an example with $A_{2A}AR$ (PDB 6gdg). In $A_{2A}AR$, the conserved motifs include the sodium binding pocket (red, D52, T88, S91, W246, N280, and S281), CWxP motif (cyan, C245, W246, L247, P248), PIF motif (pink, P189, I92, F242), NPxxY motif (yellow, N284, P285, Y288), and DRY motifs (black, D101, R102, Y103).

may reveal more detailed information and provide valuable information beneficial for predicting the next generation of drugs.

1.8 Membrane environment influences A_{2A}AR

In general, ligand stimulation and G protein coupling are the most common factors that alter the equilibrium between different conformational states in A_{2A}AR. However, as a transmembrane protein, the compositions and properties of the surrounding membrane can also play modulatory effects on the A_{2A}AR conformational dynamic [60, 61]. Therefore, it is necessary to understand the influence of the membrane environment on the receptors during targeted drug design. The environmental contexts within different locations or under pathological conditions can show identical features. For example, the disorder of the central nervous system diseases, such as Alzheimer's disease and schizophrenia, can cause relevant changes in membrane composition [62, 63]. Thus, it influences ligands and G protein interact with GPCRs and results in alterations of intracellular signaling which contribute to different drug behaviors [64]. The changing of lipid components implies that the changing of membrane physical properties which not only altered by diseases but also depends on eating habits and aging [65]. The physical properties on the membrane surface are influenced by the phospholipids headgroup, while the membrane fluidity is altered by the presence of different alkyl chains and unsaturated bonds in the lipid tail groups [66]. Previous research has uncovered that high membrane fluidity not only benefits ligand binding but also induces a shift in the conformational equilibrium towards the active form in a model GPCR, such as the 5-HT2B receptor, embedded in an artificially manufactured nanodiscs [60]. This effect is due to an

increase in electrostatic interactions with increased fluidity. Moreover, membrane fluidity can lower the energy barrier between conformational states by forming intramolecular interactions between helices, This, in turn, stabilizes the GPCR-ligand complex [65, 67].

As a crucial component of mammalian cell membranes, cholesterol plays a significant role in regulating the structural and functional aspects of membrane proteins [68]. Therefore, another focal point in the study of membrane composition is the influence of cholesterol on GPCRs. Previous computational including MD simulations confirmed the existence of the GPCR cholesterol consensus motifs (CCMs) and the influence of cholesterol on GPCR signal regulation. Moreover, cholesterol interacts with A_{2A}AR in several sites rather than one [69, 70]. It indicates that changes in cholesterol content affect the functional conformations of A_{2A}AR. Various health disorders, including Alzheimer's disease, are strongly associated with changes in the distribution and metabolism of cholesterol, whether influenced by genetic or environmental factors [62, 71, 72]. Additionally, certain pathological conditions affect cholesterol levels, leading to functional consequences in GPCR signaling [72]. For instance, membrane cholesterol depletion leads to a reduction of the downstream signaling activity of the A_{2A}AR [69]. Recently, the predictions from coarse-grained and all-atom simulations have validated A_{2A}AR-specific interactions with cholesterol. The local environments of both the inactive state and the partially active state of the receptor were observed to be deficient in cholesterol [67]. Furthermore, the NMR revealed that cholesterol and various lipids combination plays distinct roles to the A_{2A}AR's activation, especially, since cholesterol and anionic lipids share complementary roles [68]. Considering the complexity of the

mammalian plasma membrane, composed of multiple lipid species, understanding how the A_{2A}AR structure responds to different ligand bindings and cholesterol concentrations within its native membrane environment becomes a crucial topic for discussion.

1.9 Detergent-free polymer lipid particle purification retains local membrane environment

In GPCR studies, the highly dynamic conformation of GPCRs poses challenges in separating them from the complex membrane environment, usually resulting in instability and functional loss of GPCRs. While the traditional detergent-based membrane protein purification has made significant progress in the past decades, the increased stability and functionality of GPCRs are accompanied by substantial time and cost investments. Current studies about the effects of cell membranes on GPCRs structure are mainly from the purified GPCRs stabilized in artificial membranes [73]. The synthetic membrane scaffold proteins (MSPs) nanodisc environment used in GPCRs' transmembrane structure studies includes POPC, POPS, and PE, but the native cell membrane where A_{2A}AR expressing has more complex environment, such as cholesterol and more heterogeneous lipids [64, 74]. Moreover, a previous study mentioned that A_{2A}AR in nanodisc retains pharmacological activity, but its dynamic information may be disrupted by the destruction of the original close-associated lipids and lateral pressure. This evidence imply that the local environment plays an important mechanism to modify the activity of GPCRs [75]. Polymer lipid particles provide such a convenient GPCR purification technology that can also preserve the local membrane environment. This

implies that a protein retained within its native membrane environment in a polymer lipid particle maintains high stability, preserving its native folding and functional availability [76].

As a relatively mature detergent-free polymer purification method, poly (styrene-co-maleic acid) (SMA) and diisobutylene maleic acid (DIBMA) become promising ways to explore structural changes of transmembrane proteins [77] (**Figure 8**). Compared to the traditional nanodisc sample preparation, these polymers can be incorporated into the cell membrane and bind the transmembrane protein with its local environment to form nanosized SMA lipid particles (SMALPs) [78]. Although SMALP is sensitive to low pH and divalent cations, the excellent stability and high GPCR purification rate of SMALPs make it still a popular way to study in vitro GPCR functions and properties [78]. As one of the representatives of class A GPCR, A_{2A}AR-SMALP has also been studied. However, the majority of these studies focus on ligand binding capacity and thermal stability of A_{2A}AR in SMALPs [79, 80]. The remaining ligand binding capacity and thermal stability make A_{2A}AR-SMALP an available platform for structural studies [81]. Although SMA has been utilized to study GPCRs' structure and function, its sensitivity to divalent cations and the limited disc size can constrain the structural dynamics of the membrane [82]. Compared to SMALPs, DIBMALPs exhibit superior tolerance to divalent cations, particularly calcium ion (Ca^{2+}) and magnesium ion (Mg^{2+}) [77]. The larger size of the discs allows DMALPs to stabilize more membrane components around the A_{2A}AR. However, this increased disc size comes with certain drawbacks, including lower yield and stability [77]. And in our study, we used DIBMALPs for investigating the dynamic information of A_{2A}AR in its native membrane environment on molecular level.

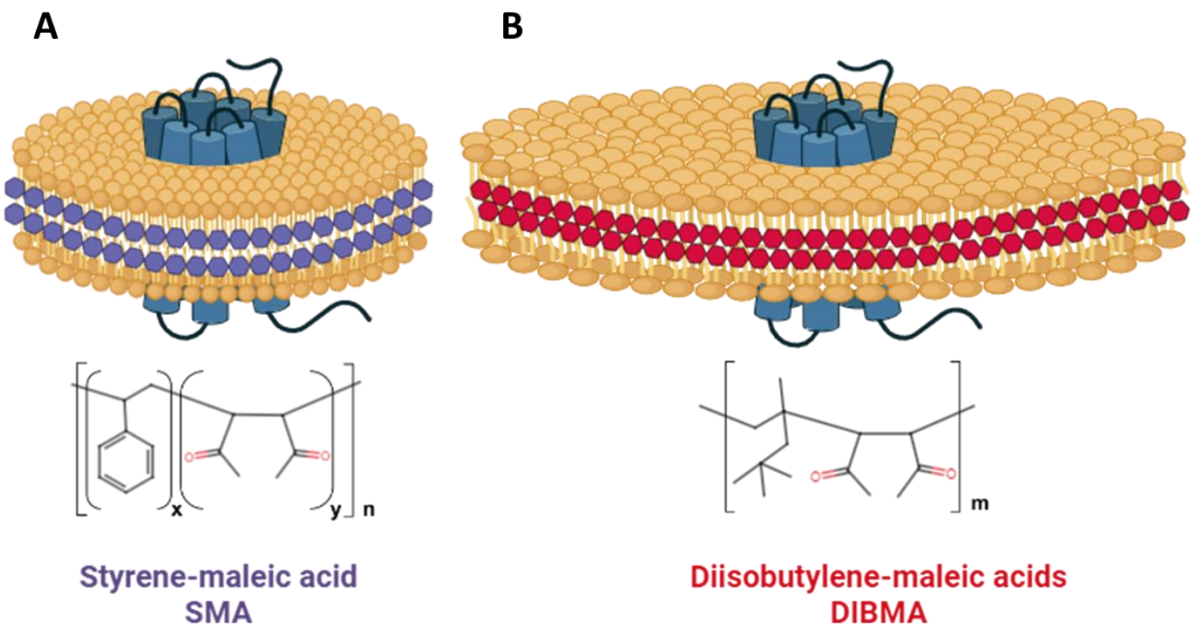

Figure 8. Native membrane polymer lipid particles.

SMA is the polymer of styrene and maleic acid, and DIBMA is the polymer of diisobutylene and maleic acid. These two are the most commonly used polymers to capture membrane proteins in their native membrane environment. Comparing the two, the (A) SMA lipid particle (SMALP) has higher yield, better purity, and stability. (B) The DIBMA lipid particle (DIBMALP) has higher tolerance to divalent cations and a larger disc size with a less ordered lipid environment.

1.10 Significant of single molecule study

Currently, different techniques, like X-ray crystallography, cryogenic electron microscopy (cryo-EM), and nuclear magnetic resonance (NMR), have been used to investigate the structure of A_{2A}AR complexes when bound with different ligands and coupled with a G protein [51, 83, 84]. However, none of them are capable of monitoring molecular-level dynamic conformational changes on biologically relevant timescales. Moreover, the information on the path connecting different states and the order in which they are populated are also missing in traditional spectroscopic methods. This limits our ability to develop drugs targeting A_{2A}AR with finely tuned therapeutic effects. Therefore, we have adopted a single-molecule fluorescence (SMF) approach that provides detailed dynamic information on different receptor conformations at the molecular level.

1.11 Single-molecule TIRF

Total internal reflection fluorescence (TIRF) microscopy is an advanced optical technique specifically designed to excite fluorophores within a narrow axial region [85]. Over the past two decades, it has developed as a single molecular technique, significantly enhancing resolution and eliminating out-of-focus fluorescence. The principle of TIRF is the utilization of optical physics to create an evanescent wave field (100~150nm) for fluorophore excitation, avoiding direct laser excitation. When a laser passes through two materials with different refractive indices, transitioning from high to low indices and reaching a critical angle for total internal reflection, an evanescent wave field is generated (**Figure 9**) [85-87].

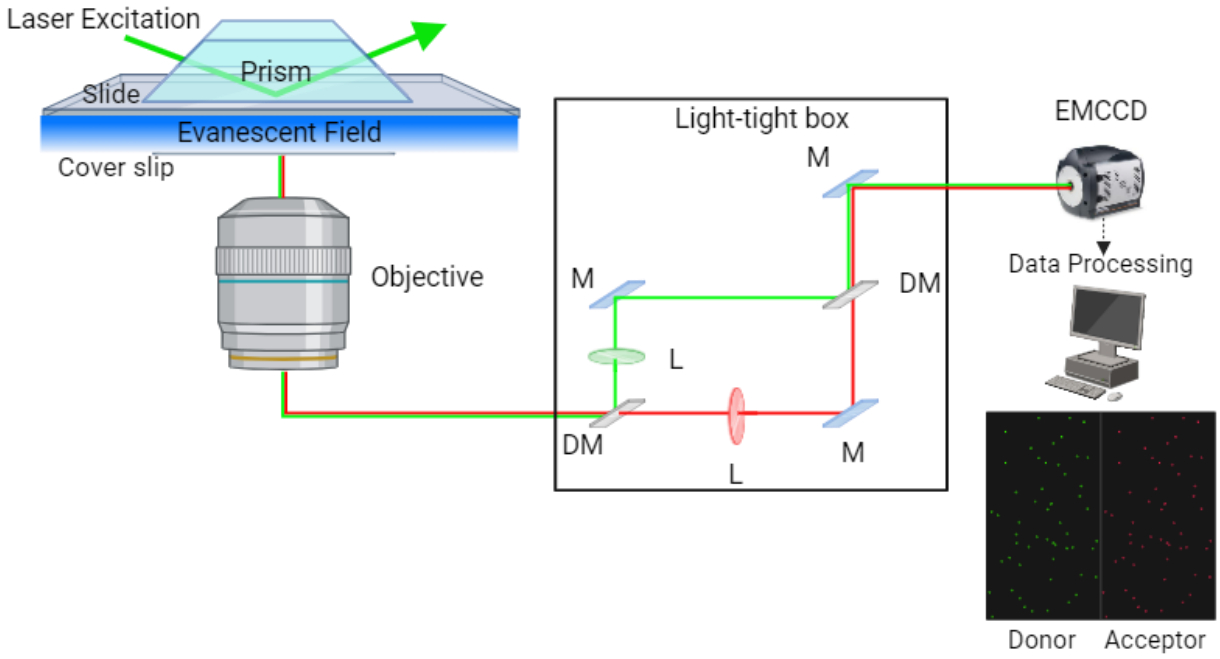

Figure 9. Schematic diagram of single-molecule total internal reflection fluorescence microscopy (SM-TIRF).

The laser excites the samples immobilized on the slide, creating an evanescent wave. Emission from the donor (green) and acceptor (red) passes into a light-tight box, where these two emissions are then captured side by side by an EMCCD camera. Inside the light-tight box, M represents a mirror, L represents a lens, and DM represents a dichroic mirror.

The restricted excitation range created by the evanescent wave makes TIRF microscopy a promising approach for single-molecular-level fluorescent observation. Besides, it effectively reduces fluorophore photobleaching in solution and prevents harmful light damage to the live cell sample [86, 87]. Traditionally, TIRF microscopy was used to study fluorescently labeled protein–protein, and protein–nucleic acid interactions [85, 88]. It allows direct visualization and quantification of kinetic rates at the single-molecule level.

In comparison to the bulk experiments, single molecule TIRF reveals individual stochasticity, variability, and heterogeneity, providing insights into details that cannot be detected by bulk experiments [85]. Besides, despite the need for high-quality and pure samples, the single molecule TIRF requires much lower concentrations (pM to nM), which enhance the efficiency with limited material [89]. Meanwhile, proteins with relatively dynamic structures, such as GPCRs, TIRF can be employed to uncover dynamic information by monitoring processes like fluorescent resonance energy transfer (FRET) and protein-induced fluorescent enhancement (PIFE) [87, 90]. As for the A_{2A}AR, like most other class A GPCRs, the transmembrane (TM) helixes VI and VII undergo significant conformational change during the activation [91]. Consequently, single-molecule TIRF has become our preferred method for tracking the dynamic information of A_{2A}AR in vitro.

CHAPTER II. SLOW CONFORMATIONAL DYNAMICS OF THE HUMAN A_{2A} ADENOSINE RECEPTOR ARE TEMPORALLY ORDERED

A version of this chapter was originally published by Shushu Wei, Naveen Thakur, Arka P Ray, Beining Jin, Samuel Obeng, Christopher R McCurdy, Lance R McMahon, Hugo Gutiérrez-de-Terán, Matthew T Eddy, Rajan Lamichhane on Structure in November 2021. (Website: https://www.cell.com/structure/fulltext/S0969-2126(21)004172?_returnURL=https%3A%2F%2Flinkinghub.elsevier.com%2Fretrieve%2Fpii%2FS0969212621004172%3Fshowall%3Dtrue)

For this study, Shushu Wei implemented and supervised the project, conducted single-molecule experiments, collected and analyzed data, and wrote and edited the manuscript. Naveen Thakur and Arka P Ray conducted A_{2A}AR expression, labeling, and purification. Samuel Obeng, Christopher R. McCurdy, and Lance R. McMahon conducted radioligand binding experiments. Hugo Gutiérrez-de-Terán performed simulations. Rajan Lamichhane and Matthew T. Eddy acquired funding, supervised experiments and data analysis, and contributed to writing the manuscript with input from all co-authors.

2.1 Abstract

A more complete depiction of protein energy landscapes includes the identification of different function-related conformational states and the determination of the pathways connecting them. We used attenuated total internal reflection fluorescence (TIRF) imaging to investigate the conformational dynamics of the human A_{2A} adenosine receptor (A_{2A}AR), a class A GPCR, at the single-molecule level. The slow, reversible conformational exchange was observed among three different fluorescence emission states populated for agonist-bound A_{2A}AR. Transitions among these states predominantly occurred in a specific order, and exchange between inactive and active-like conformations proceeded through an intermediate state. Models derived from molecular dynamics simulations with available A_{2A}AR structures rationalized the relative fluorescence emission intensities for the highest and lowest emission states but not the transition state. This suggests that the functionally critical intermediate state required to achieve activation is not currently visualized among available A_{2A}AR structures.

2.2 Introduction

Time-dependent fluctuations of the atomic coordinates of proteins, i.e. conformational dynamics, are inherently related to their biological functions, as demonstrated over 40 years ago by NMR spectroscopy [92, 93] and subsequent additional biophysical methods. An understanding of protein conformational dynamics is necessary to develop fundamental mechanistic insights into processes such as protein-substrate and protein-protein interactions in biological systems.

These same molecular recognition processes give rise to the physiological activities of G protein-coupled receptors (GPCRs), sensory proteins that bind an enormous range of endogenous and exogenous ligands, including many hormones, neurotransmitters, and clinical drugs [94]. Chemical information contained in bound ligands is relayed to the GPCR intracellular surface through conformational dynamics that enable receptors to recognize intracellular partner proteins and initiate signaling cascades. Information on function-related dynamics has predominantly been provided by spectroscopic methods, which complement GPCR structures from x-ray crystallography and cryogenic electron microscopy (cryo-EM) [95, 96]. Many spectroscopic methods, including NMR spectroscopy, typically observe average properties of proteins from a large ensemble of molecules. These spectroscopic methods can identify multiple, simultaneously-populated conformational states. However, when more than two states are observed, information on the pathways connecting different states and, most importantly, the order in which they are populated must come from single-molecule measurements [97-100].

We used single-molecule fluorescence to study the conformational dynamics of the human A_{2A} adenosine receptor (A_{2A}AR), a representative class A GPCR. A_{2A}AR has been the focus of a growing number of NMR spectroscopic studies [49, 52, 91, 101-105], which provide a rich set of literature data as a background for the further development of additional biophysical methods to study GPCRs. Thus, it seemed to be a logical next step to extend single-molecule fluorescence experiments developed to study the β_2-adrenergic receptor [106-108] to A_{2A}AR as a second member of class A GPCRs.

Using single-molecule total internal reflection fluorescence (TIRF) imaging, we observed relatively slower ($k_{ex} \leq 10\ s^{-1}$) exchange processes in $A_{2A}AR$ with a fluorophore covalently attached to helix 7 at the intracellular surface. Our data complement other $A_{2A}AR$ studies that investigated relatively faster time scales using single-molecule Förster resonance energy transfer (FRET), which measured ligand efficacy-dependent changes for sub-millisecond to ~3 millisecond molecular motions of $A_{2A}AR$ in detergent micelles [109] and in lipid nanodiscs [110]. In the present study, measurements of slower exchange processes provide a new window into $A_{2A}AR$ function-related conformational dynamics.

2.3 Result

2.3.1 $A_{2A}AR$ sample preparation and TIRF imaging experimental design

For single-molecule fluorescence imaging experiments, a variant of human $A_{2A}AR$ containing a single cysteine replacement at position 289 located at the intracellular surface of helix 7, $A_{2A}AR$[A289C], was expressed in *Pichia pastoris* using previously described protocols (see Star Methods) [49]. The location of the introduced cysteine was selected based on literature data from ^{19}F NMR studies of $A_{2A}AR$ [91], which demonstrated that NMR spectra of $A_{2A}AR$ labeled with ^{19}F-2,2,2-trifluoroethanethiol at the same position were sensitive to differences in the efficacies of bound ligands [91]. C289 was the only cysteine available for chemical conjugation. Purified $A_{2A}AR$[A289C] was reconstituted into lipid nanodiscs containing a 65:30:5 molar ratio mixture of POPC, POPS, and biotinylated POPE lipids, respectively, and labeled with the Cy3 fluorophore at position 289, yielding homogeneous sample preparations (**Figure S1**). $A_{2A}AR$[A289C]

labeled with Cy3 in lipid nanodiscs retained nearly native ligand binding affinities for antagonists and agonists, as measured by radioligand binding experiments on the same samples measured in single-molecule fluorescence experiments (**Figure S1**). In the following sections, Cy3-labeled A_{2A}AR[A289C] is referred to as A_{2A}AR-Cy3.

To investigate the conformational dynamics of A_{2A}AR at the single-molecule level, we immobilized nanodiscs containing A_{2A}AR-Cy3 on a microscope slide and monitored them under TIRF illumination following protocols established in single-molecule fluorescence experiments with the b_2-adrenergic receptor [106, 107]. The resolution of the camera used in TIRF imaging experiments enabled observations of changes in fluorescence emission on the time scale of $\geq$ 100 milliseconds, correlating to rates of exchange processes of $k_{ex} \leq 10\ s^{-1}$. Control experiments were performed to characterize the specific immobilization of biotin-labeled nanodiscs to a PEG-coated quartz slide surface using biotin-streptavidin interactions (**Figure S2**). Fluorescence time trajectories were measured for A_{2A}AR-Cy3 with no ligand added during the sample preparation, i.e., apo A_{2A}AR-Cy3 (**Figure 10A**), and for A_{2A}AR-Cy3 in complexes with the antagonist ZM241385 and agonists NECA (**Figure 10B**) and CGS21680. Following protocols validated in earlier TIRF studies with GPCRs [106, 107], subsequent analysis focused on data from dynamic molecules from folded and functional receptors. Approximately 40% to 50% of the trajectories showed dynamic behavior, comparable to earlier studies with b_2AR where approximately 60% of the molecules showed dynamic behavior [111, 112].

2.3.2 Two predominant fluorescence emission states are observed with apo and antagonist bound A_{2A}AR in lipid nanodiscs

The majority of apo A_{2A}AR-Cy3 trajectories showed dynamic behavior where the fluorescence intensity reversibly fluctuated primarily between two intensity states (**Figures 10A and S3**). We normalized the fluorescence intensities with the mean intensity of the lowest intensity states at each point and compiled traces of 239 individual molecules to generate a histogram (**Figure 10C**). The histogram shows two distinct peaks centered around two different intensity states with relative areas 62% and 38% that we assigned as State 1 and State 2, respectively (**Figure 10C**).

Similar to apo A_{2A}AR-Cy3, the majority of A_{2A}AR-Cy3 molecules in complex with the antagonist ZM241385 also showed dynamic behavior with fluorescence intensities that fluctuated between two intensity states (**Figure 10E**) with the same mean fluorescence emission intensities observed for apo A_{2A}AR-Cy3. The resulting histogram generated from single-molecule traces of 288 molecules of A_{2A}AR-Cy3 in complex with ZM241385 showed two distinct states centered around the same intensity values as apo A_{2A}AR-Cy3 with relative areas of 58% for State 1 and 32% for State 2, comparable to observations with apo A_{2A}AR-Cy3 (**Figure 10, C and E**). For both apo and antagonist-bound A_{2A}AR-Cy3, we also observed a relatively small population of transitions to an even higher third intensity state (**Figure 11, C and E**); however, the number of these transitions was not sufficient to populate this state on the histogram.

2.3.3 Three fluorescence emission states are observed with agonist-bound A_{2A}AR in lipid nanodiscs

Single-molecule fluorescence traces of A_{2A}AR-Cy3 in complexes with the agonists NECA and CGS21680 showed dynamic behavior for a majority of the observed molecules. In traces of agonist-bound A_{2A}AR-Cy3, three distinct emissions intensities were observed (**Figure 10B**). For the A_{2A}AR-Cy3 complex with NECA, traces from 229 molecules were compiled into a histogram (**Figure 10D**), which showed distinct changes compared with the histograms for apo and antagonist-bound A_{2A}AR-Cy3. Compared to apo and antagonist-bound A_{2A}AR-Cy3, the histogram for A_{2A}AR-Cy3 in complex with NECA showed a decrease in the population of State 1 (49%), an increase in the population of State 2 (39%) and the emergence of a third peak, which we defined as “State 3” (12%) (**Figure 10D**). Single-molecule experiments with A_{2A}AR-Cy3 in complex with a second agonist, CGS21680, showed similar behavior to the complex with NECA. A histogram compiled from traces of 315 molecules of A_{2A}AR-Cy3 in complex with CGS21680 showed three distinct states with relative areas of 46%, 39% and 15% calculated for States 1, 2 and 3, respectively (**Figure 10F**).

2.3.4 Structural models of A_{2A}AR-Cy3 provide a rational for two of the observed fluorescence intensities.

Because the Cy3 fluorescence emission intensity depends on the local environment of the fluorophore, changes in the fluorescence emission are strongly correlated with changes in protein structure and the environment of Cy3 [106, 107, 113, 114]. To investigate the structural basis for the observed different fluorescence intensities

Figure 10. Single-molecule fluorescence intensity trajectories and histograms compiled from a collection of individual A_{2A}AR molecules.

(A) An example of single-molecule fluorescence intensity trajectory from immobilized apo A_{2A}AR-Cy3 in lipid nanodiscs. Repeated intensity jumps are observed predominantly between two fluorescence intensity states at ~200 a.u. and ~400 a.u. before photobleaching. The trajectory shows raw intensities without normalization or fitting with a Hidden Markov model. Loss of intensity fluctuations after a single-step photobleaching transition (black arrow) indicates a single receptor molecule is observed.

(B) Single-molecule fluorescence intensity trajectory of A_{2A}AR in complex with the agonist NECA. Intensity jumps are observed among three intensity states at ~200 a.u., ~400 a.u. and ~600 a.u. Same presentation details as in (A). The selected trace shows the range of transitions between different events, including several transitions to State 3 before photobleaching.

(C) Histogram compiled from 239 receptor molecules of A_{2A}AR where no ligand was added to the sample (apo). The dashed black and blue lines represent fits to two gaussian populations centered around the normalized intensities of 1 and 2. Fluorescence intensities are normalized to the mean intensity of the low-intensity state. The composite fit representing the sum of the two gaussian fitted curves is shown as the solid black line.

Figure 10. Single-molecule fluorescence intensity trajectories and histograms compiled from a collection of individual A_{2A}AR molecules.

(D) Histogram compiled from 229 receptor molecules of A_{2A}AR in complex with the agonist NECA. The dotted black and blue lines represent fits to two gaussian populations centered around the normalized intensities of 1 and 2, and the red dotted curve represents a fit to a third gaussian population centered around the normalized intensity of 3. The composite fit representing the sum of the three gaussian fitted curves is shown as the solid black line.

(E) Histogram compiled from 287 receptor molecules of A_{2A}AR in complex with the antagonist ZM241385. Same presentation details as in (C).

(F) Histogram compiled from 315 receptor molecules of A_{2A}AR in complex with the agonist CGS21680. Same presentation details as in (D).

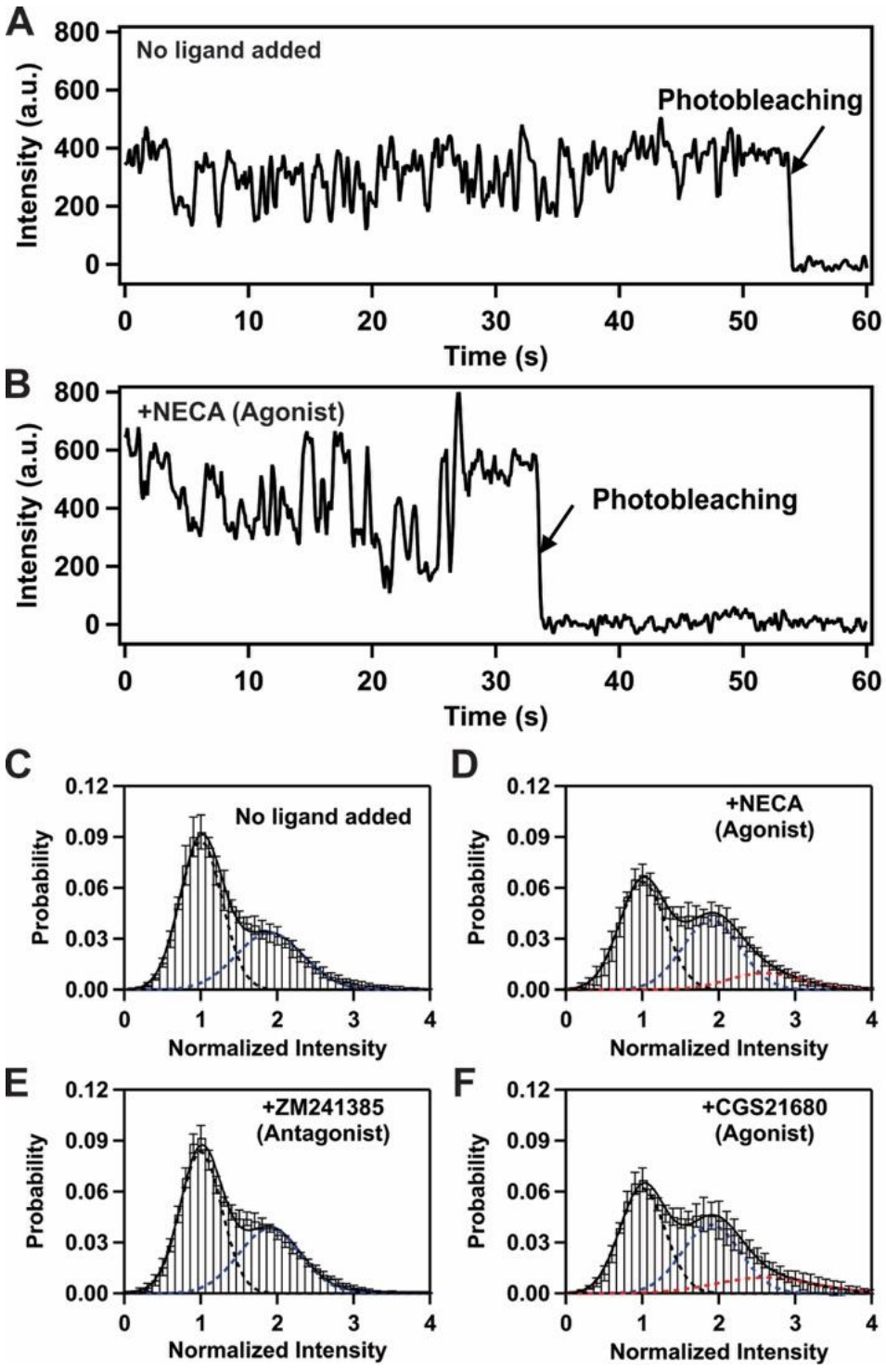

Figure 10. Single-molecule fluorescence intensity trajectories and histograms compiled from a collection of individual A_{2A}AR molecules.

of A_{2A}AR-Cy3 complexes, we generated three computational models of A_{2A}AR-Cy3 by covalently docking the fluorophore to representative crystal structures of human A_{2A}AR and followed this with extensive atomistic MD simulations (see STAR Methods). From these models, we investigated the range of possible orientations of Cy3 and the local environment around the dye, which can control the conformational degrees of freedom of the dye and influence fluorescence emission intensities.

Three structures were chosen as representatives for generating the initial models: A_{2A}AR in complex with the antagonist ZM241385 (PDB ID 4EIY) [115], A_{2A}AR in complex with the full agonist NECA (PDB ID 2YDV) [116] and a tertiary complex with NECA and an engineered G protein, "mini $G\alpha_S$" (PDB ID 5G53) [117]. For each case, the initial model was created by manually covalently docking Cy3 to the sidechain of $C289^{7.54}$ and the corresponding system subjected to triplicate MD simulations, accounting for a total sampling time of 1.5 μs for each conformation. Evaluation of the trajectories included a cluster analysis of the conformations visited by the Cy3 molecule (**Figure S4**) and a contact map to detect and visualize potential interactions of Cy3 with nearby aromatic residues.

In all simulations of antagonist-bound A_{2A}AR-Cy3, Cy3 is consistently oriented toward the intracellular interface between the membrane bilayer and surrounding aqueous solution (**Figure 10A**) and exhibited a relatively large degree of conformational freedom, as observed in the principal component analysis (PCA) and cluster analysis (**Figure S4**). A larger degree of conformational freedom of the dye results in lower fluorescence emission, and thus we assigned State "1" to the antagonist-bound

conformation. This assignment is also consistent with the larger observed population of State 1 in the histograms of apo and antagonist-bound A_{2A}AR-Cy3 (**Figure 10, E and G**).

In simulations of agonist-bound A_{2A}AR-Cy3, Cy3 is located in a very different environment than for apo and antagonist-bound A_{2A}AR-Cy3 and is observed to be surrounded by the intracellular ends of several transmembrane helices (TM) 2, 3, 6 and 7 and intracellular loops 1 and 2 (**Figure 11B**). In this environment, Cy3 shows a smaller degree of conformation freedom, which would result in higher fluorescence emission. We thus assigned State 3 to the agonist bound A_{2A}AR conformation based on the significantly increased transitions to State 3 for the agonist complexes. Comparing the conformation of the dye between agonist-bound and antagonist-bound A_{2A}AR-Cy3, one can observe a clear dependence of the dye orientation on the global conformation of the receptor. In particular, the orientation of $C289^{7.54}$, where the dye is covalently attached, strongly depends on the backbone configuration of helix 7, which changes between inactive and active conformations of A_{2A}AR [116-118]. Thus, changes in the observed intensity of Cy3 related to differences in the efficacies of bound ligands could be assigned to large conformational changes in the structure of A_{2A}AR-Cy3. As expected, no interconversion between structures was observed in our simulations, since the time scale of the atomistic MD simulations is orders of magnitude shorter than the time scales reported for the exchange between inactive and active conformational states [91, 119].

In MD simulations of A_{2A}AR-Cy3 in a tertiary complex with the agonist NECA and mini Ga_S, Cy3 shows a similar local environment as described for the A_{2A}AR-Cy3 complex with NECA (**Figure 11, B and C**). Based on this result, we expect that the fluorescence

Figure 11. Structural models and representative fluorescence intensity trajectories from individual Cy3-labeled A_{2A}AR single molecules in complex with different ligands and with no ligand added (apo).

(A) A structural model of A_{2A}AR in complex with the antagonist ZM241385 is shown in grey ribbon representation. ZM241385 is shown in cyan stick representation, and the Cy3 fluorophore covalently attached to position C289 is shown in red space-filling representation. Cy3 is positioned near the interface between the lipid bilayer and surrounding aqueous solution and is expected to exhibit a lower fluorescence emission due to a larger magnitude of conformational flexibility.

(B) A structural model of A_{2A}AR in complex with the agonist NECA is shown in grey ribbon representation. NECA is shown in cyan stick representation, and the Cy3 fluorophore covalently attached to position C289 is shown in green space-filling representation. Cy3 is located near the intracellular surface and surrounded by transmembrane helices (TM) 2, 3, 6 and 7, as well as ICL1 and ICL2, as annotated. In this position, the rate of isomerization of Cy3 fluorophore decreases, leading to an expected increase in fluorescence emission.

(C) A structural model of A_{2A}AR in a tertiary complex with the agonist NECA and GaS. A_{2A}AR is shown in grey ribbon representation, NECA is shown in cyan stick representation, and GaS is shown in blue ribbon representation.

(D) A dynamic trajectory of A_{2A}AR-Cy3 without ligand added (apo). The Cy3 intensity is normalized by the mean value of the lowest intensity state. The intensity trajectories (black) are fitted by a three-state Hidden Markov model (red). The trace shows a few transitions to state 3 that are very short in duration.

Figure 11. Structural models and representative fluorescence intensity trajectories from individual Cy3-labeled A_{2A}AR single molecules in complex with different ligands and with no ligand added (apo).

(E) A dynamic trajectory of the A_{2A}AR with agonist, NECA. The trace for A_{2A}AR in complex with an agonist shows more frequent transitions to a third, higher intensity state and also show that the molecule spends a longer time in the third state as compared to traces with no ligand and antagonist (ZM241385).

(F) A dynamic trajectory of A_{2A}AR in complex with the antagonist ZM241385. Similar to the apo trace, the signal only spends a short time in state 3.

(G) A dynamic trajectory of the A_{2A}AR with agonist CGS21680. Same presentation details as in (E).

(H) An expanded view of the trajectory from 38 to 48 seconds from the section in panel (E) indicated by orange vertical dashed lines. The expanded view shows clear transitions between states 1 to 2 and states 2 to 3 and also shows a rare direct transition from state 3 to state 1.

transitions between states 1 to 2 and states 2 to 3 are showsn.

(I) An expanded view of the trajectory from 10 to 20 seconds from the section in panel (F) marked by blue vertical dashed lines. Multiple sequential transitions between states 1 to 2 and states 2 to 3 are shown.

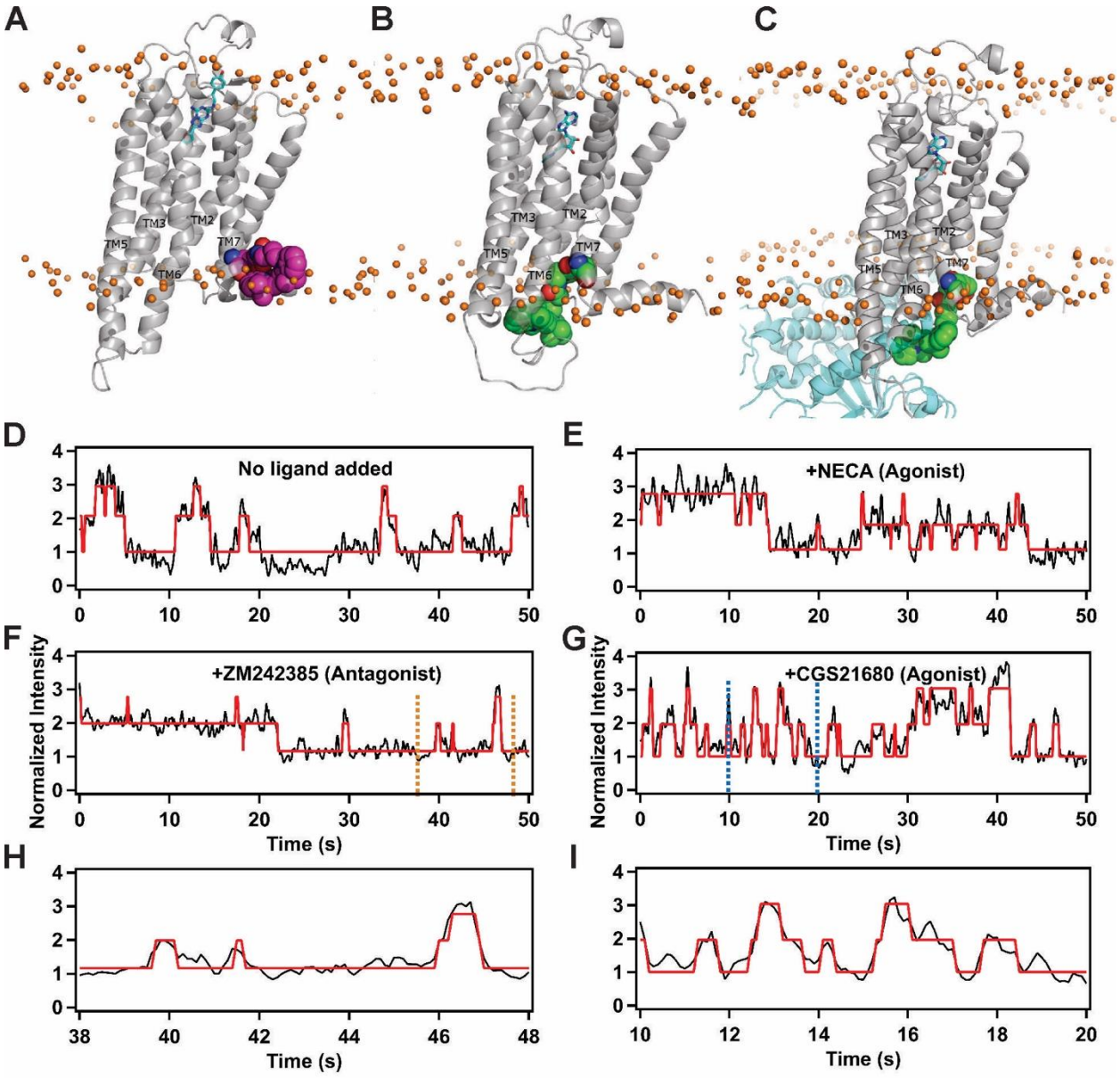

Figure 11. Structural models and representative fluorescence intensity trajectories from individual Cy3-labeled A_{2A}AR single molecules in complex with different ligands and with no ligand added (apo).

The emission intensity of Cy3 is similar between the agonist-bound conformation and the tertiary conformation. From the above analysis,it follows that the fluorescence emission state defined as State 2 is likely not represented among currently available structures of A_{2A}AR.

2.3.5 Transitions among fluorescence intensity states occur in a reversible and sequential order

Fluorescence intensities for normalized single-molecule time trajectories were fit using a three-state hidden Markov model [120]. The fitted lines are shown by the red lines in **Figure 10**. Results from fitting the trajectories were consistent with the intensity histograms of **Figure 9**. For apo A_{2A}AR-Cy3, the majority of molecules transitioned between two states, State 1 and State 2 (**Figure S3A**). A much smaller number of transitions to a higher intensity state, State 3 (**Figure 11C and Table S1)** were also observed but did not occur with sufficient frequency to populate the histogram (**Figure 10C**). The A_{2A}AR-Cy3 complex with the antagonist ZM241385 showed behavior similar to apo A_{2A}AR-Cy3, with the vast majority of transitions occurring between States 1 and 2 (**Figure 11E**). In contrast to these data, the A_{2A}AR-Cy3 complexes with agonists NECA and CGS21680 showed more frequent transitions between State 2 and State 3 (**Figure 11E and G**). For agonist-bound A_{2A}AR, transitions to State 3 remained in State 3 for a longer duration than for apo and antagonist-bound A_{2A}AR (**Figure 11E and G and Table S1**).

To further visualize the frequencies of transitions and the connectivity of the three intensity states, we generated two-dimensional Transition Density Plots (TDP) by using

transitions from the fitted traces (**Figure 12**). TDPs of apo A_{2A}AR-Cy3 clearly showed two densities populated around normalized intensities 1 and 2 (**Figure 12A**), signifying frequent and prominent reversible transitions between State 1 and State 2. Similar transitions were also observed between States 1 and 2 in the TDP for the A_{2A}AR-Cy3 complex with the antagonist ZM241385 (**Figure 12B**).

TDPs of A_{2A}AR-Cy3 complexes with the agonists NECA and CGS21680 were significantly different from apo and antagonist-bound A_{2A}AR-Cy3 (**Figure 12**). In the presence of agonists, we observed that the receptor more frequently transitioned to State 3 and also spent a longer time at State 3 before returning to State 2 (**Figure 12C** and **D**, and **Table S1**). TDPs for A_{2A}AR-Cy3 complexes with the agonists NECA and CGS21680 revealed a third region with clear density at the intersection of States 2 and 3. We further analyzed the hidden Markov fitted time trajectories to quantify the relative number of sequential transitions between State 1, State 2 and State 3. Fewer than 2 % of the total transitions were occurred directly between State 1 and State 3. These rare transitions were observed for both agonist-bound and antagonist-bound A_{2A}AR, however the addition of agonist did not increase the frequency of these rare transitions. This observation is reflected in the corresponding TDPs, which do not show measurable densities related to direct transitions between State 1 and State 3 (**Figures 12C and D**). Overall, these data indicate that for agonist-bound A_{2A}AR, transitions between State 1 and State 3 almost always proceed through, State 2, which may be a potential intermediate state required for receptor activation.

2.4 Discussion

We observed three distinct fluorescence emission states for agonist-bound A_{2A}AR-Cy3 (**Figures 10 and 11**). These distinct fluorescence emission states corresponding to different local environments of the Cy3 fluorophore bound to position 289 in helix 7 (**Figure 11, A-C**). The three states are also observed for the complex with the antagonist ZM241385 and the apo receptor (**Figure 11, C and D**), though the population of the highest emission state for apo and antagonist-bound A_{2A}AR was too low to visualize as a significant fraction of the total population in histograms (**Figure 10**). MD simulations of A_{2A}AR-Cy3 indicate that due to steric hindrances, the fluorophore cannot change local environments without larger structural rearrangements of the receptor (**Figure 11, A-C**). Thus, the different emission states likely correlate with backbone rearrangements of the A_{2A}AR transmembrane helices at the intracellular surface.

The observation of three distinct states is interesting when compared with earlier single-molecule fluorescence studies of the b2-adrenergic receptor, where two conformational states were observed in single-color TIRF experiments that used a similar experimental design as the present study [106, 107]. Two conformational states were also reported in single-molecule FRET experiments [108]. The different number of observed emission states between A_{2A}AR and b_2AR, suggest potential differences in mechanisms of activation and indicate that further investigations of many more different class A GPCRs are needed to develop a more general understanding of GPCR function-related conformational dynamics.

In the present study, the integration time of the camera used for data acquisition was 100 ms, so fluctuations in the fluorescence intensity must occur on time scales equal to or slower than 100 ms to be observed, corresponding to rates of exchange processes on the order of 10^{-1} s^{-1} or slower. These relatively slower processes are in line with rates of exchange between different conformational states measured in ^{19}F-NMR experiments of A_{2A}AR in detergent micelles containing DDM and CHS [91]. These slower rates and are also in line with rates of slow conformational exchange in b_2AR estimated by ^{19}F-NMR to be $k_{ex} \leq 10$ s^{-1} [119]. MD simulations in the present work could detect two different conformational states of A_{2A}AR-Cy3 but are not sufficiently long to detect these slow transitions between different conformational states observed in single-molecule fluorescence data.

The present work complements other recent single-molecule studies of A_{2A}AR that measured dynamic processes on relatively faster time scales. In a recent report of single-molecular FRET of A_{2A}AR in detergent micelles containing LMNG and CHS, ligand-depending shifts and broadening of smFRET distributions were interpreted to suggest exchange between inactive and active conformations of A_{2A}AR that occurred on a timescale of ~3 ms or $k_{ex} \geq$ ~30–40 s^{-1} [109]. In a separate study, Maslov et al. reported observations of exchange processes on a similar time scale of sub-millisecond to low millisecond fluctuations with A_{2A}AR in nanodiscs containing POPC and POPG lipids [110]. Both the Fernandes et al. and Maslov et al. studies utilized a diffusion-based experimental design in which the observation of FRET signals depends on the rate of diffusion of the receptors in aqueous solutions.

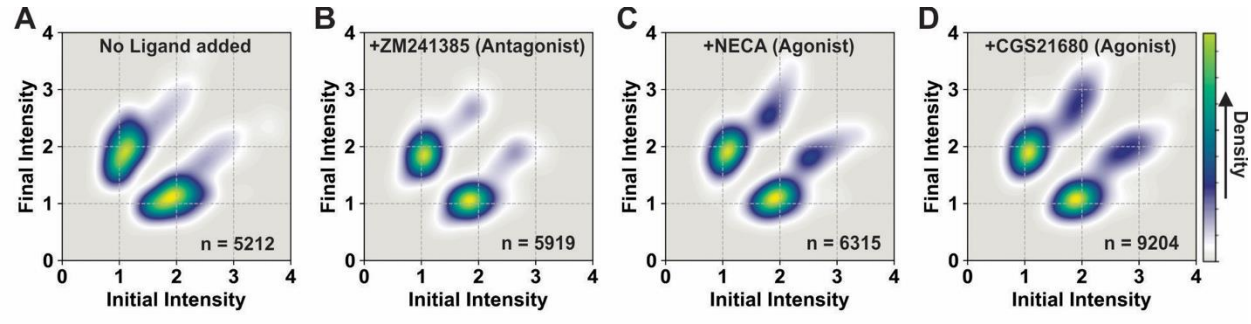

Figure 12. Transition density plots (TDPs) of A_{2A}AR complexes with different ligands and without ligand.

The TDPs are generated from the normalized initial and final intensities. In these plots, 'n' represents the number of transitions used to prepare the TDPs. The gradient color scheme is indicated in the rightmost bar, where the arrowhead points toward relatively higher density, which re

lates to the frequency of observed transitions.

(A and B) The TDPs of apo and antagonist-bound A_{2A}AR show that transition events predominantly occur between states 1 and 2.

(C and D) The TDPs of A_{2A}AR in complexes with the agonists NECA and CGS21680 show that transition events occur between states 1 and 2 and between states 2 and 3 with measurable frequencies. Only negligible densities are observed between states 1 and 3, indicating that very few transitions occur directly between those two states.

This design would not permit observations of exchange processes with rates that are reported here. With the TIRF experimental design, molecules are tethered to the microscope slide, which allows one to monitor dynamics on relatively longer time scales. The relatively faster dynamics reported by Fernandes and Maslov may have also occurred with A_{2A}AR samples in the present study but were not observed due to limitations of the time resolution of the camera.

One of the more surprising observations of this work is the reversible temporal ordering of the fluorescence emission states (**Figure 13**). This observation is reminiscent of single-molecule FRET data from a recent study of a class C GPCR dimer where receptor monomers were labeled with different fluorophores and FRET measurements were recorded between each monomer in a functional dimer [121]. In Liauw et al., FRET data were interpreted as evidence of "conformational checkpoints" that suggested an activation process involving step-wise interactions between monomers in the homodimer [121]. Here we observed a step-wise process involving conformational changes within a class A GPCR monomer. This observation creates a new framework for understanding GPCR activation processes and for resolving questions in future studies of how orthosteric ligands, allosteric modulators and mutations may potentially alter the order of these exchange processes.

2.5 Experimental model and subject details

2.5.1 Microbes

XL-10 *E. coli* cells were cultured in LB media, BL21(DE3) cells were cultured in TB media, and the BG12 strain of *P. pastoris* was cultured in BMGY and BMMY media. All cell lines

Figure 13. Schematic of the temporal ordering observed for transitions among A_{2A}AR conformational states.

For each receptor cartoon representation, the color of the rightmost intracellular helix corresponds to the color scheme used with the histograms shown in Figure 10 panels C-F.

(A) For apo A_{2A}AR and antagonist-bound A_{2A}AR, transitions are predominantly observed between states 1 and 2, indicated by the black arrows. Far fewer transitions are observed between states 2 and 3, indicated by the grey arrows.

(B) For agonist-bound A_{2A}AR, transitions are observed between states 1 and 2 and between states 2 and 3 (black arrows).

(C) Transitions directly between states 1 and 3 are only very rarely observed, as indicated by the red 'X'.

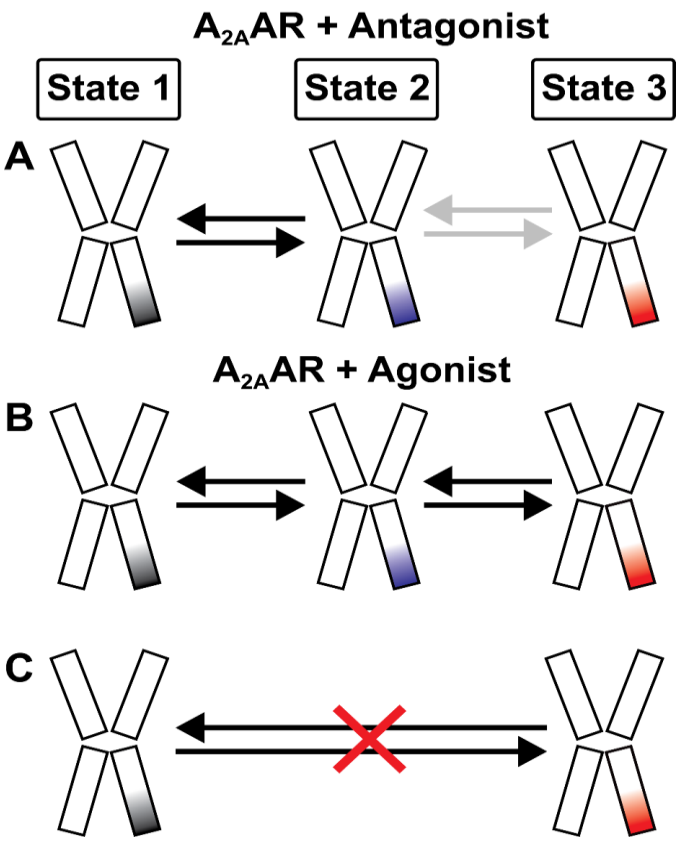

Figure 13. Schematic of the temporal ordering observed for transitions among A_{2A}AR conformational states.

used in this study were authenticated by the suppliers and were chosen to remain consistent with previous studies.

2.5.2 Mutagenesis

PCR-based site-directed mutagenesis (QuickChange II, Strategene, CA) was used to generate the A_{2A}AR A289C variant used for single-molecule fluorescence experiments. Primers used for this effort are provided in the Key Resources Table.

2.5.3 MSP1D1 expression and purification

MSP1D1 was expressed and purified similar to protocols described in previous studies [122, 123]. MSP1D1 encoded in the open reading frame of a pET28a vector (Invitrogen) was transformed into the BL21(DE3) E. coli strain. A single transformed colony was inoculated into 5 mL Luria–Bertani (LB) broth containing 50 mg/mL kanamycin and incubated overnight at 37 ºC with shaking. 1 L Terrific Broth (TB) media was inoculated with the overnight culture and allowed to reach an optical density of 0.6-0.8, and protein expression was induced with 1 mM isopropyl β-D-1-thiogalactopyranoside (IPTG) and allowed to proceed for 4 hours at 37 ºC. The cells were harvested by centrifugation at 4000 x g for 30 min, frozen in liquid nitrogen and stored at -80 °C for later use. The cell pellets were thawed and resuspended in lysis buffer (50 mM Tris-HCl, pH 8.0, 500 mM NaCl, 1% Triton X-100, and 1 mM EDTA) at 20 mL of buffer per gram of cell pellet and 100 µL of in-house prepared protease inhibitor solution was added. The resuspended cells were lysed with a single pass through a cell disruptor (Pressure Biosciences) operating at 20,000 psi. Insoluble material was separated by ultracentrifugation at 20,000 x g at 4 °C for 45 minutes, and the supernatant was applied

to a Ni-NTA column equilibrated with 50 mM Tris-HCl, pH 8.0, 500 mM NaCl, and 1% (w/v) Triton X-100. The column was washed with 5 CV of wash buffer 1 (50 mM Tris-HCl, pH 8.0, 500 mM NaCl, and 1% (w/v) Triton X-100), washed with 5 CV of buffer 2 (50 mM Tris-HCl, pH 8.0, 500 mM NaCl, and 50 mM cholate), washed with 5 CV of buffer 3 (50 mM Tris-HCl, pH 8.0, and 500 mM NaCl) and washed with 5 CV of buffer 4 (50 mM Tris-HCl, pH 8.0, 500 mM NaCl, and 20 mM imidazole). MSP1D1 was eluted with 5 CV of buffer containing 50 mM Tris-HCl, pH 8.0, 500 mM NaCl, and 500 mM imidazole. Fractions containing MSP1D1 were pooled and dialyzed against 50 mM Tris-HCl, pH 8.0, 20 mM NaCl, and 0.5 mM EDTA in dialysis tubing with a 10 kDa MWCO (Thermo-Fisher Scientific). MSP1D1 was then incubated with tobacco etch virus (TEV) protease at a 1:100 (TEV: MSP) molar ratio overnight at 4 °C. The protein solution was applied to a nickel column and the flow-through fraction containing purified MSP1D1 was collected. MSP1D1 was then transferred into a storage buffer containing 20 mM Tris, pH 7.5, 100 mM NaCl, and 0.5 mM EDTA by dialysis for 4 hours using dialysis tubing with a 10 kDa MWCO (Thermo-Fisher Scientific). MSP1D1 was concentrated to 1 mM, frozen in liquid nitrogen and stored at −80 °C for future use.

2.5.4 A_{2A}AR production

The gene encoding human A_{2A}AR(1-316) containing a point mutation to remove the only glycosylation site (N154Q), an N-terminal FLAG tag, and a 10 X C-terminal His tag was cloned into a pPIC9K vector (Invitrogen) at the BamHI and NotI restriction sites. Alanine 289 was replaced with cysteine via site-directed mutagenesis, and the resulting plasmid was introduced by electroporation into the BG12 strain of *Pichia pastoris*

(Biogrammatics). Transformed colonies were screened for optimal protein expression using a previously reported Western blot assay [49] that utilizes an anti-FLAG monoclonal conjugated antibody to identify high-expressing clones. Once identified, glycerol stocks were prepared from high-expressing clones and stored at -80 ºC. Small scale cultures containing 4 mL buffered minimal glycerol (BMGY) media in 15 mL culture tubes were inoculated from the glycerol stock and grown at 30 °C for 48 hours to reach an optical density of 9-10. These cultures were then used to inoculate 50 mL BMGY medium in a 250 mL baffled flask and incubated at 30 °C for approximately 60 hours to reach an optical density of 15-20. Subsequently, 2.8 L baffled flasks containing 500 mL BMGY media were inoculated with the 50 mL cultures and incubated at 30 °C for 48 hours to reach an optical density of 15-20. Cells were collected by centrifugation at 3000 x g for 15 minutes and resuspended in 500 mL of buffered minimal methanol (BMMY) medium without methanol and the temperature was lowered to 28 °C. These cultures were incubated for 6 hours to ensure a complete metabolic digest of glycerol before methanol was added to a final concentration of 0.5% w/v to induce protein expression. Two additional 0.5% w/v aliquots of methanol were added at 12-hour intervals after initial induction. Expression proceeded for a total of 36 hours and then cells were harvested by centrifugation at 3000 x g for 15 minutes. The isolated cell pellets were frozen in liquid nitrogen and stored at -80 °C for later purification.

2.5.5 A_{2A}AR purification

Cell pellets containing A_{2A}AR were resuspended in lysis buffer (50 mM sodium phosphate pH 7.0, 100 mM NaCl, 5% glycerol (w/v), and in-house prepared protease

inhibitor solution) and lysed by a single pass through a cell disruptor (Pressure Biosciences) operating at 40,000 psi. Membranes were isolated and collected by ultracentrifugation at 200,000 x g, frozen in liquid nitrogen and stored at -80 °C for future use. Isolated membrane pellets were resuspended in buffer (10 mM HEPES pH 7.0, 10 mM KCl, 20 mM $MgCl_2$, 1M NaCl) and treated with 1 mM theophylline and protease inhibitor solution for 1 hour. Subsequently, protein was extracted from the membrane in a buffer containing 0.5% (w/v) n-Dodecyl-β-D-Maltopyranoside (DDM), 0.05% cholesteryl hemisuccinate (CHS), 50 mM HEPES pH 7.0, and 500 mM NaCl for 6 hours at 4 °C. Then insolubilized material was separated by ultracentrifugation at 200,000 x g for 30 min, and the supernatant was collected and incubated overnight at 4 °C with Co^{2+}-charged affinity resin (Talon, Takara Bio USA) and 30 mM imidazole. The resin was then washed with 20 CV of wash buffer 1 (50 mM HEPES pH 7.0, 500 mM NaCl, 10 mM $MgCl_2$, 30 mM imidazole, 8 mM ATP, 0.05% DDM, and 0.005% CHS). Resin was collected and washed 2 more times with 20 CV of wash buffer 2 (25 mM HEPES pH 7.0, 250 mM NaCl, 5% glycerol, 30 mM imidazole, 0.05% DDM, 0.005% CHS, and ligand), and eluted with buffer 3 (50 mM HEPES pH 7.0, 250 mM NaCl, 5% glycerol, 300 mM imidazole, 0.05% DDM, 0.005% CHS, and ligand). After elution, the protein was exchanged into a final buffer (25 mM HEPES pH 7.0, 75 mM NaCl, 0.05% DDM, 0.005% CHS, and ligand), using a PD-10 desalting column (Cytiva). All buffers were prepared with a saturating concentration of the required ligand. Apo protein was purified without the addition of ligands to the sample preparation buffers.

2.5.6 Single-molecule fluorescence sample preparation

The assembly of nanodiscs followed protocols adapted from previous studies [122, 123] that were further optimized for experiments with A_{2A}AR. Purified A_{2A}AR was mixed with purified MSP1D1 and lipids solubilized in buffer (25 mM Tris pH 8.0, 150 mM NaCl, and 200 mM sodium cholate) in a molar ratio of 1:5:250 (A_{2A}AR: MSP1D1:lipids). Lipids were mixed in a molar ratio of 65:30:5 (POPC:POPS:biotin-POPE) prior to mixing with A_{2A}AR and MSP1D1. The mixture of A_{2A}AR, MSP1D1 and lipids was incubated for 4 hours at 4 °C. Subsequently, bio-beads (Bio-Rad Laboratories) were added to the mixture and incubated overnight at 4 °C. The bio-beads were then removed and the resulting mixture was incubated with Ni-NTA resin (GoldBio) for 24 hours at 4 °C. After overnight incubation, a 10 folds molar excess of the Cy3 maleimide fluorophore (GE Healthcare) was added to the mixture and incubated in the dark at 4 °C for 3 h. The resin was then washed with 2 CV of a wash buffer (50 mM HEPES, pH 7.0, 150 mM NaCl and 10 mM imidazole), and nanodiscs containing A_{2A}AR were eluted with buffer (50 mM HEPES, pH 7.0, 150 mM NaCl, 300 mM imidazole and ligand). After elution, any remaining excess fluorophore was removed by exchanging the sample into a final buffer (25 mM HEPES pH 7.0, 75 mM NaCl, and ligand) using a PD-10 desalting column (Cytiva). All buffers were prepared with a saturating concentration of ligand or without ligand added (apo).

2.5.7 Radioligand binding assays for A_{2A}AR in lipid nanodiscs

Radioligand binding assays were performed with the same samples of A_{2A}AR[A289C] used for single-molecule fluorescence experiments; i.e., in nanodiscs containing the same lipid composition and with the Cy3 fluorophore covalently attached

at position 289. For the displacement binding experiments, increasing concentrations of cold ligands were incubated with the radioligand [^{3}H]ZM241385 (American Radiolabeled Chemicals, St. Louis, MO) and with 0.125-0.25 µg of nanodiscs containing A_{2A}AR in buffer containing 25 mM HEPES pH 7.0 and 75 mM NaCl for 60 min at room temperature. Binding reactions were terminated by filtration using the Microbeta filtermat-96 cell harvester (PerkinElmer, Waltham, MA) and radioactivity was measured using a MicroBeta2 microplate counter (PerkinElmer, Waltham, MA). Specific binding at A_{2A}AR was determined as the difference in binding obtained in the absence and presence of 10 µM ZM241385.

2.5.8 Single-molecule fluorescence data acquisition

Single-molecule fluorescence data were recorded using a customized prism-based TIRF imaging system based on an inverted IX73 microscope (Olympus) and customized TIRF stage (TIRF Labs Inc., Cary, NC, U.S.A.) as described in earlier publications [124, 125]. Quartz microscope slides (G. Finkenbeiner, Waltham MA) and coverslips were cleaned and passivated with polyethylene glycol (m-PEG-SVA) and 3% biotin-PEG-SVA (Laysan Bio Inc, Arab, AL) as previously described [89]. A sample chamber was prepared using PEGylated slides and coverslips using double-sided tape and coated with 0.02 mg/ml streptavidin [124]. Nanodiscs containing A_{2A}AR and 5% biotin-PE in imaging buffer (20 mM HEPES pH 7.5, 75 mM NaCl, 2 mM Trolox and saturating concentration of ligand or no ligand added) were introduced into the sample chamber and incubated for 10 minutes. The sample chamber was rinsed with an imaging buffer to remove any nonspecific molecular species. The chamber was rinsed with

glucose oxidase and a catalase oxygen scavenging system in imaging buffer and excited using a green (532 nM) laser. The emission intensities from the Cy3 fluorophore were collected on an EMCCD camera (Andor Technology) with 100 ms integration time using a custom single-molecule data acquisition program [124]. Single-molecule time trajectories were extracted using scripts written in IDL software (Harris Geospatial Solutions, Inc). The package for data acquisition and extraction was downloaded from the laboratory of Dr. Taekjip Ha (http://ha.med.jhmi.edu/resources/).

2.5.9 Molecular dynamics simulations

Molecular dynamics (MD) simulations of A_{2A}AR with the Cy3 fluorophore conjugated to cysteine 289 were performed using three different initial configurations of the receptor structure. The initial configuration of antagonist-bound A_{2A}AR was modeled from the crystal structure of A_{2A}AR in complex with the antagonist ZM241385 and with a coordinated sodium ion in a putative allosteric site (PDB ID 4EIY) [115]. Agonist-bound A_{2A}AR was modeled from the crystal structure of A_{2A}AR in complex with NECA (PDB ID 2YDV) [116]. A tertiary complex of A_{2A}AR was modeled from the crystal structure of A_{2A}AR in a complex with NECA and an engineered G protein ("mini $G\alpha_s$"; PDB ID 5G53) [117]. The antagonist-bound A_{2A}AR structure was prepared for MD simulations following previously reported procedures [126] that removed the non-native BRIL fusion protein used to facilitate crystallization and replaced the native residues in the third intracellular loops that were removed to facilitate crystallization. For agonist-bound A_{2A}AR, the point mutations introduced to increase the melting temperature of the receptor for crystallization were reverted to their native amino acid types with Pymol [127]. Protons were added to

all structures, the protonation states of titratable residues, including histidine, were calculated and the hydrogen bonding network was optimized with the protein preparation wizard tool in Maestro [128]. For all three structures, the native Ala289$^{7.54}$ sidechain was replaced with cysteine, and the Cy3 fluorophore was modeled with manual covalent docking using a 3D-optimized conformation of the fluorophore built in Maestro and further optimized with the Macromodel tools within the Schrödinger suite [129].

Each receptor construct was inserted into a solvated membrane model and equilibrated following the PyMemDyn protocol [126, 130]. The starting structures are automatically embedded in a pre-equilibrated membrane consisting of POPC lipids, and the transmembrane bundle was aligned to its vertical axis, i.e., the bundle of helices was aligned parallel to the Z-axis. This hexagonal-prism shaped box is then soaked with bulk water and energy minimized with GROMACS 4.6 [131] using the OPLS-AA/M force field [132] for the receptor and ligands and with Berger parameters for the lipids [133] together with the use of the half-e double-pairlist method [134] and the SPC water model [135]. The same setup is used for a 2.5 ns MD equilibration under periodic boundary conditions (PBC), where initial restraints on receptor and ligand atoms are gradually released, followed by another 2.5 ns MD where only the distance restraints between interhelical contacts in class-A GPCRs were imposed, as previously described in detail [130]. OPLS compatible parameters for all organic molecules (ZM241385, NECA and Cy3 maleimide) were generated with the LigParGen server [136] and translated into GROMACS with ad hoc scripts. For the Cy3 maleimide covalently attached to Cys289$^{7.54}$ a pseudoresidue was manually created. Each system was then subject to three replica MD simulations in

GROMACS, each lasting for 0.5 ms. The isobaric NPT ensemble was used with a Nose-Hoover thermostat [137, 138] with a target temperature of 310 K. Electrostatic interactions beyond a cutoff of 12 Å were estimated with the particle mesh Ewald method, and a 2 fs time step was used combined with the LINCS algorithm [139]. All MD analyses were conducted with the mdtraj library [140]. Molecular superimpositions, trajectory visualizations, and molecular images were performed with PyMOL. Analysis of the trajectories was performed with the MDtraj package [140].

2.6 Quantification and statistical analysis

2.6.1 Single-molecule fluorescence data analysis

Single-molecule fluorescence time trajectories were assessed and analyzed using custom software written in Matlab. Individual trajectories were selected for further analysis from trajectories with single-step photobleaching that displayed reversible fluorescent intensity fluctuations at different intensity states before bleaching, which are described as dynamic traces. Individual dynamic traces were background corrected and normalized to the mean value of the lower-intensity state, which is defined as a value of "1". Each trace was truncated before photobleaching, and the traces were binned and compiled to generate intensity histograms.

Histograms were generated by compiling more than 100 normalized single-molecule traces from at least two independent experiments. Error bars on histograms are the standard error calculated from 5 individual movies used to generate the histograms. Similar approaches were also used to process error bars previously [121]. To fit and process histograms, we used Igor Pro software (version 8.04, Wavemetrics, Lake

Oswego, OR, USA). In detail, histograms for apo and antagonist-bound $A_{2A}AR$ fit two Gaussian distributions, and agonist-bound $A_{2A}AR$ three Gaussian distributions using Igor's Multipeak Fit 2 function as shown in equations 1 and 2, respectively.

$$y = y_0 + A_1 \exp\left\{-\left(\frac{x-b_1}{w_1}\right)^2\right\} + A_2 \exp\left\{-\left(\frac{x-b_2}{w_2}\right)^2\right\} \quad \text{.....1}$$

$$y = y_0 + A_1 \exp\left\{-\left(\frac{x-b_1}{w_1}\right)^2\right\} + A_2 \exp\left\{-\left(\frac{x-b_2}{w_2}\right)^2\right\} + A_3 \exp\left\{-\left(\frac{x-b_3}{w_3}\right)^2\right\} \quad \text{.....2}$$

In the equations above, y_0 is a baseline, A is the peak amplitude, b is the intensity peak center, and w is the peak width. The Find Peaks algorithm was used to locate the number of peaks and fit those peaks using the mean conformational states as peak centers calculated from the transition density plots. We used 1.0, 1.9, and 2.6 normalized intensity peak centers to fit peaks 1, 2, and 3, respectively. The third peak was not populated for Apo and ZM bound samples, so it only fitted with two distributions. After fitting, the area of individual peaks was calculated from the A and w values obtained from the fit. A Hidden Markov model was used to fit individual trajectories into different states with the HaMMy program [120]. Transition density plots were generated from the HaMMy fitted data that provided the transition events between different states. We used custom software written with Python to generate the transition density plots [141].

2.6.2 Quantification and analysis of ligand binding for $A_{2A}AR$ in lipid nanodiscs

IC_{50} values were determined using a nonlinear, least-squares regression analysis by Prism 8 (GraphPad Software). IC_{50} values obtained from the displacement curves were converted to K_i values using the Cheng-Prusoff equation [142]. Data are expressed

as the mean ± the standard error from three independent experiments performed in triplicate.

2.7 Acknowledgments

This work was supported by the National Institutes of Health, grant number R35GM142946 (R. L.) and the start-up funds from the College of Arts and Sciences, University of Tennessee, Knoxville (R. L.). This research was funded by the National Institutes of Health, grant numbers R35GM138291 (M.T.E, N.T., A.P.R and B.J.), DA048353 (L.R.M and C.R.M) and DA047855 (L.R.M and C.R.M), and a Ralphe E. Powe Junior Faculty Award from Oak Ridge Affiliated Universities (M.T.E). We thank Raymond Pauszek from The Scripps Research Institute for providing custom software to prepare the transition density plots.

CHAPTER III. SINGLE-MOLECULE VISUALIZATION OF HUMAN A_{2A} ADENOSINE RECEPTOR ACTIVATION BY A G PROTEIN AND CONSTITUTIVELY ACTIVATING MUTATIONS

A version of this chapter was originally published by Shushu Wei, Niloofar Gopal Pour, Sriram Tiruvadi-Krishnan, Arka Prabha Ray, Naveen Thakur, Matthew T. Eddy, Rajan Lamichhane on Communication Biology in November 2023. (Website: https://www.nature.com/articles/s42003-023-05603-6)

In this research, Shushu Wei implemented and supervised the project, conducted single-molecule experiments, collected, and analyzed data, and wrote and edited the manuscript. Niloofar Gopal Pour and Naveen Thakur conducted the expression, labeling, and purification of A_{2A}AR wild type and three different mutants. Besides, they also did the size exclusion chromatography and ligand binding assay. Sriram Tiruvadi-Krishnan modified customer written program and analyzed data, especially analyzed kinetic data. Rajan Lamichhane and Matthew T. Eddy supervised experiments and data analysis and contributed to writing the manuscript with input from all co-authors.

3.1 Abstract

Mutations that constitutively activate G protein-coupled receptors (GPCRs), known as CAMs, modify cell signaling and interfere with drugs, resulting in diseases with limited treatment options. We utilized total internal reflection fluorescence (TIRF) imaging at the single-molecule level to visualize the dynamic process of CAM-mediated activation of the human A_{2A} adenosine receptor (A_{2A}AR) in real time. We observed an active-state population for all CAMs without agonist stimulation. Importantly, activating mutations significantly increased the population of an intermediate state crucial for receptor activation, notably distinct from the addition of a partner G protein. Activation kinetics showed while CAMs increased the frequency of transitions to the intermediate state, mutations altering sodium sensitivity increased transitions away from it. These findings indicate changes in GPCR function caused by mutations may be predicted based on whether they favor or disfavor the formation of an intermediate state, providing a new framework for designing receptors with altered functions or therapies that target intermediate states.

3.2 Introduction

Inherited and acquired mutations in cell surface receptors often disrupt intracellular signaling, which underlies a wide range of diseases, including developmental growth diseases and cancers. With more than 800 members, human G protein-coupled receptors (GPCRs) are cell surface receptors that participate in numerous and diverse physiological processes and constitute the largest family of druggable proteins [94]. While GPCR signaling is typically activated by agonists, such as small molecules or

polypeptides, GPCRs also exhibit basal activity in the absence of external stimulation, the extent of which varies among receptors [143, 144]. Mutations can alter basal level signaling, with some mutations leading to reduction or loss of signaling, while other mutations, known as constitutively activating mutations (CAMs), increase receptor basal activity. CAMs can increase basal activity by increasing receptor cell surface expression or promoting receptor transport, or by altering the conformational equilibria between different receptor functional states [145-147]. The mechanisms by which CAMs alter the dynamic equilibrium of GPCR conformers are poorly understood. CAMs resulting in agonist-independent gain-of-function have been linked to various diseases, such as hyperthyroidism resulting from mutations in the thyrotropin receptor [148], dwarfism resulting from mutations in the parathyroid hormone receptor [149], and hypocalcemia resulting from mutations in the calcium-sensing receptor [145]. CAMs are also strongly associated with the onset and progression of numerous cancers, including mutations in the α_{1B}-adrenergic receptor that promote tumorigenicity [150] and mutations in the smoothened receptor that contribute to drug-resistant basal cell carcinoma [151]. Additionally, certain human viruses encode for constitutively active receptors, such as herpesvirus KSHV, which produces a constitutively active GPCR associated with Karposi's sarcoma [152], and the Epstein-Barr virus, which encodes constitutively active BILF1 [153]. While evidence from pharmacological studies across various receptor types highlights the role of constitutively activating mutations in abolishing a receptor's response to drug efficacy, the mechanisms responsible for this action are not entirely understood.

The structural basis for constitutive activity is so far limited to crystal structures of three distinct GPCRs: rhodopsin [154], the neurotensin receptor NTSR1 [155], and the A_{2A} adenosine receptor (A_{2A}AR) [156]. This is compared to the crystal and cryo-EM structure of more than 100 unique receptors and more than 600 structures of GPCRs with ligands or partner proteins in total. In this study, we apply single-molecule fluorescence (SMF) to provide additional insight into the structural basis of GPCR constitutive activity.

The human A_{2A}AR belongs to the class A, or rhodopsin-like GPCRs, and is a validated target for Parkinson's disease,[44, 157, 158] as well as a target for treating multiple cancers [159-161]. Understanding the mechanisms of A_{2A}AR signaling has been the focus of a growing number of spectroscopic approaches, especially nuclear magnetic resonance (NMR) spectroscopy [49, 52, 56, 101-105, 162-164]. Single-molecule fluorescence (SMF) provides unique and complementary information on the pathways connecting distinct conformational states and the order in which they are populated [121, 165]. Total internal reflection SMF, in particular, has enabled the observation of slow conformational changes of the human β_2-adrenergic receptor that correlated with global structural rearrangements and activation of the receptor [87, 108, 166]. Complementing the approach using TIRF, diffusion-based experimental designs have also observed A_{2A}AR dynamics on faster, sub-millisecond timescales [109, 167].

Using TIRF SMF, slow, reversible exchange among three fluorescence intensity states was observed for human A_{2A}AR bound to agonists within lipid nanodiscs [165]. This exchange revealed that the population of an active-like A_{2A}AR conformation proceeded through an intermediate state, with direct transitions between inactive and

active-like conformations being rare [165]. These findings established a conceptual framework for comprehending A_{2A}AR activation as a step-wise, reversible process. In this process, small molecule agonists enhanced the frequency of transitions from an inactive state to an intermediate state before ultimately reaching an active conformation. We leveraged this framework to investigate whether CAMs altered this step-wise process or circumvented it altogether. Additionally, we applied the same framework to distinguish the effects of CAMs from the influence of ternary complex formation with a G protein on the A_{2A}AR activation mechanism.

These observations were compared with single-molecule fluorescence measurements of an A_{2A}AR variant that uncouples ligand-binding activity from signaling. Notably, this variant exhibited significant differences in the rate constants between the inactive state and intermediate state compared to A_{2A}AR variants containing CAMs. Through quantitative analysis of state lifetimes and their exchange rates, we uncovered that both mutations and the addition of a G protein substantially impact the conformational equilibria between the inactive and intermediate states, while only marginally affecting the equilibria between the intermediate and active states. Our data yield valuable mechanistic insights into the sequence of events required for GPCR activation and offer potential insights into pharmacological intervention in CAM-associated diseases.

3.3 Results

3.3.1 Single-molecule fluorescence with constitutively active A_{2A}AR variants in lipid nanodiscs

For single-molecule fluorescence imaging experiments, we utilized a variant of A_{2A}AR that contained a single solvent-accessible cysteine replacement at position 289, located at the intracellular surface of Helix 7 (**Figure 14**) [168], which we refer to as A_{2A}AR in the following text. Previous single-molecule fluorescence [165] and NMR studies [56, 163] demonstrated that structural probes at this location are sensitive reporters to changes in the conformation of A_{2A}AR associated with different efficacies of bound ligands. To investigate the impact of activating mutations, we created two additional variants from the A_{2A}AR sequence, $I92^{3.40}N$ and $R291^{7.56}Q$ (superscripts denote the Ballesteros-Weinstein nomenclature for GPCR residue positions). The amino acid replacement $I92^{3.40}N$, located in transmembrane (TM) 3 near the conserved "toggle switch" tryptophan $W246^{6.48}$, was previously shown to increase A_{2A}AR basal activity [169]. The second amino acid replacement $R291^{7.56}Q$, located near the intracellular surface of Helix VII, was shown to increase basal activity by disrupting interactions with the adjacent Helix VI and associated lipid molecules [56]. These two variants were selected because they both resulted in increased basal activity, but the locations of the mutations were in very different regions of the receptor (**Figure 14**). To provide a point of comparison, we also studied an A_{2A}AR variant containing a single inactivating mutation, $D52^{2.50}N$, located in the TM region of Helix II. This variant has been documented to retain native-like ligand binding

affinities for both antagonists and agonists but demonstrates a nearly complete loss of G protein signaling activity [49, 170].

Purified A_{2A}AR and A_{2A}AR variants were reconstituted into lipid nanodiscs containing a 65:30:5 molar ratio mixture of 1-palmitoyl-2-oleoyl-glycero-3-phosphocholine (POPC), 1-palmitoyl-2-oleoyl-sn-glycero-3-phospho-L-serine (POPS), and biotinylated 1-palmitoyl-2-oleoyl-glycero-3-phosphoethanolamine (POPE) lipids, respectively, and shown to produce homogeneous samples (**Figure S5**). The variant A_{2A}AR[R291Q] had been previously shown to retain pharmacological activity highly similar to native A_{2A}AR in lipid nanodiscs [56]. Using competitive radioligand experiments, we verified the ligand binding activity of A_{2A}AR[I92N] and A_{2A}AR[D52N] in the nanodiscs with the same lipid composition as single-molecule fluorescence experiments and found both variants to retain native-like pharmacological activity (**Figure S6**). A_{2A}AR and A_{2A}AR variants were labeled with the Cy3 fluorophore at position 289, according to previously reported protocols [165, 171]. As the Cy3 fluorescence emission intensity depends on the local environment of the fluorophore, changes in the fluorescence emission intensity are strongly correlated with changes in protein structure and the environment around Cy3 [87, 113, 114], which we observed previously for A_{2A}AR labeled at position C289 [165]. Cy3-labeled A_{2A}AR variants were immobilized on a microscope slide and monitored under TIRF illumination, following established protocols [87, 165]. The resolution of the camera used in TIRF imaging experiments facilitated observations of changes in fluorescence emission occurring on the timescale of 100 milliseconds. This capability enabled us to capture processes that occurred on a timescale of 10 s^{-1} or slower, which correlated with

function-related conformational rearrangements of the receptor backbone [119, 165]. Control experiments were performed to characterize the specific immobilization of biotin-labeled nanodiscs to a PEG-coated quartz slide surface using biotin-streptavidin interactions [165].

3.3.2 Constitutively active A_{2A}AR variants exhibit transitions among three fluorescence intensity states

Fluorescence emissions were measured, and fluorescence time trajectories were generated for Cy3-labeled A_{2A}AR, A_{2A}AR[I92N], A_{2A}AR[R291Q], and A_{2A}AR[D52N] with no ligand added during the sample preparation, i.e., apo preparation, and for complexes with the antagonist ZM241385 and the agonist NECA, which were compared with single-molecule traces recorded with A_{2A}AR (**Figure S7 and Figure 15**). ZM241385 and NECA were chosen because they have been extensively utilized within the scientific literature for investigating A_{2A}AR in pharmacological and biophysical studies and because each shares its pharmacophores with the majority of other antagonists or full agonists, respectively [172].

Following protocols validated in earlier TIRF studies with GPCRs [87, 165], subsequent analysis focused on data from dynamic molecules from folded and functional receptors. Approximately 40%–50% of the trajectories exhibited dynamic behavior while the remaining 50 to 60% of the trajectories showed a static single-step bleaching behavior without any transitions, consistent with earlier SMF studies of A_{2A}AR [165] and β_2AR[87, 166].

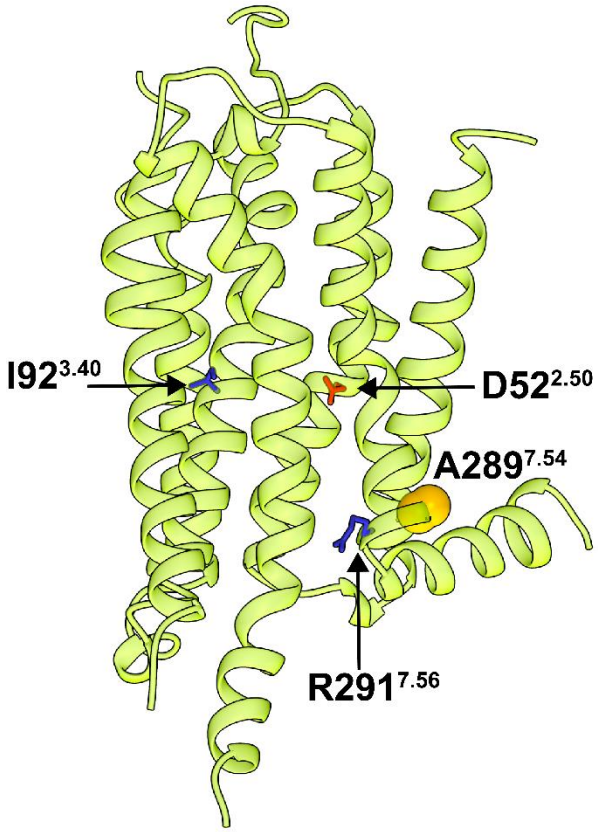

Figure 14. Locations of A289 and residues modified to study signaling mechanisms in a crystal structure of human A_{2A}AR.

Locations of A289 and residues modified to study signaling mechanisms in a crystal structure of human A_{2A}AR. A_{2A}AR in complex with the antagonist ZM241385 is shown in ribbon representation (PDB 3eml). The A289 in helix VII is shown in space-filling representation and residues D52, I92 and R291 are shown in stick representation are presented.

Previously, two distinct fluorescence emission intensities were observed for $A_{2A}AR$ without ligand added (apo) or in complex with the antagonist ZM241385.[165] For agonist complexes with $A_{2A}AR$, a third fluorescence intensity state was also observed, which was assigned to an active or active-like conformation [165]. In contrast to the observations with $A_{2A}AR$, for both variants $A_{2A}AR$[I92N] and $A_{2A}AR$[R291Q], we observed three distinct fluorescence emission intensities not only for agonist-bound preparations but also for complexes with the antagonist ZM241385 and in absence of any ligand added (**Figure S7**). For $A_{2A}AR$[D52N], we also observed three fluorescence emission intensities for the apo sample and for complexes with the antagonist ZM241385 and agonist NECA (**Figure S7**).

3.3.3 Constitutively activating mutations increase the population of an intermediate state required for $A_{2A}AR$ activation

Single-molecule fluorescence traces of $A_{2A}AR$, $A_{2A}AR$[D52N], $A_{2A}AR$[I92N], and $A_{2A}AR$[R291Q] were compiled into histograms to facilitate comparison of the relative populations of the observed fluorescence states (**Figure 15, Table S5**). In the absence of any ligand added (apo), $A_{2A}AR$ exhibited two distinct fluorescence emission states centered around two peaks, with relative areas of 63% and 37% for states 1 and 2, respectively. Similarly, for the complex with the antagonist ZM241385, two peaks with relative areas of 63% and 37% for states 1 and 2, respectively, were observed (**Figure 15a and Table S4**). For agonist-bound $A_{2A}AR$, distinct emission states were observed centered around three peaks, with relative areas of 49%, 37%, and 14% for states 1, 2, and 3, respectively (**Figure 15a and Table S4**), consistent with previous findings.[165]

Compared with $A_{2A}AR$, the variant $A_{2A}AR$[D52N] exhibited three fluorescence emission intensities not only for the agonist-bound receptor but also for the apo receptor and the complex with the antagonist ZM241385 (**Figure 15B and Table S4**). Compared to $A_{2A}AR$, for all samples of $A_{2A}AR$[D52N], the peak corresponding to state 1 was increased and the peak corresponding to state 2 exhibited a diminished area (**Table S4**). Furthermore, the peak intensities observed for $A_{2A}AR$[D52N] were highly similar for complexes with antagonists and agonists, indicating that the mutation eliminated the sensitivity of the receptor to the efficacy of bound ligands (**Figure 15B and Table S4**).

Both variants $A_{2A}AR$[I92N] and $A_{2A}AR$[R291Q] exhibited three fluorescence emission intensities for the apo receptor and for complexes with the antagonist ZM241385 and agonist NECA (**Figure 15C, Figure 15D and Table S4**). Notably, for all $A_{2A}AR$ variants, including those containing CAMs, no new fluorescence emission states were observed compared with $A_{2A}AR$. Instead, compared to $A_{2A}AR$, for variants containing CAMs, we observed a decrease in the population of state 1, an increase in the population of state 2, and a significant increase in the population of state 3 for apo receptors and for complexes with the antagonist and with the agonist (**Table S4**). Additionally, for both $A_{2A}AR$[I92N] and $A_{2A}AR$[R291Q], we observed similar histograms for apo samples and for complexes with antagonists and agonists, indicating the efficacy of bound ligands did not impact on the relative areas of the three fluorescence emission states.

Figure 15. Single-molecule fluorescence histograms compiled from collections of individual molecules of A_{2A}AR, A_{2A}AR[D52N], A_{2A}AR[I92N] and A_{2A}AR[R291Q].

(A) Histograms compiled for A2AAR with no ligand added (apo), in complex with the antagonist ZM241385, and in complex with the agonist NECA. The dashed lines represent fits to Gaussian populations centered around the normalized intensities of 1 (black), 2 (blue), and 3 (red). The composite fit representing the sum of the Gaussian fitted curves is shown as a solid black line. Error bars represent the standard error calculated for each bar of the histogram.

(B-D) Histograms compiled for (B) A_{2A}AR[D52N], (C) A_{2A}AR[I92N] and (D) A_{2A}AR[R291Q]. Same presentation details as in (A).

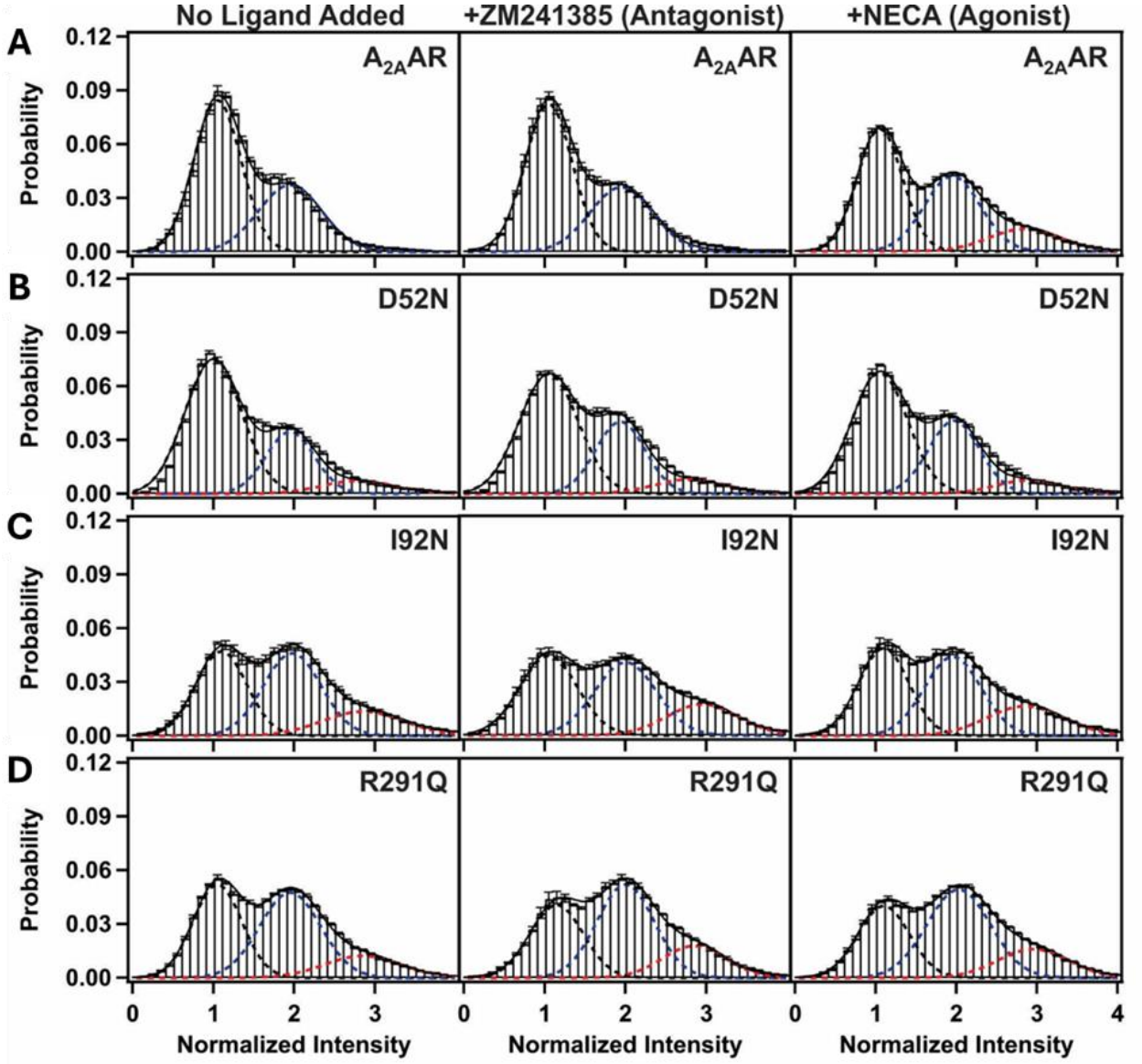

Figure 15. Single-molecule fluorescence histograms compiled from collections of individual molecules of A_{2A}AR, A_{2A}AR[D52N], A_{2A}AR[I92N] and A_{2A}AR[R291Q].

3.3.4 A_{2A}AR Variants Containing Constitutively Activating Mutations Exhibit Reversible Fluctuations Among Three Intensity States in Sequential Order

Fluorescence intensities for normalized single-molecule time trajectories were fit using a hidden Markov model (**Figure S7**) [120]. To visualize the transitions between states and the connections among the states, we generated two-dimensional transition density plots (TDPs) using transitions from the fitted traces for A_{2A}AR and all A_{2A}AR variants (**Figure 16**). For A_{2A}AR, the TDP for the complex with the agonist NECA was significantly different from the TDP of apo and antagonist-bound A_{2A}AR (**Figure 16A**), consistent with earlier results [165]. Specifically, agonist-bound A_{2A}AR exhibited more frequent transitions to state 3 and spent a longer time in state 3 before transitioning to state 2. Importantly, transitions between states 1 and 3 were infrequent, consisting of fewer than 1% of the total transitions, and thus were not visible in the TDP (**Figure 16A and Table S6**). Comparatively, for A_{2A}AR[D52N], all TDPs for the apo receptor and complexes with the antagonist ZM241385 and agonist NECA appeared highly similar, with only subtle differences observed for the complex with the agonist NECA (**Figure 15A**). Transitions between states 1 and 3 were again very rare, consisting of fewer than 2% of the total transitions, analogous to A_{2A}AR (**Table S6**).

TDPs for the CAM-containing variants A_{2A}AR[I92N] and A_{2A}AR[R291Q] appeared similar to each other and also resembled the TDP for agonist-bound A_{2A}AR (**Figure 16C and Figure 16D**). Interestingly, unlike A_{2A}AR, the TDPs for all samples of A_{2A}AR[I92N] and A_{2A}AR[R291Q] showed only minor differences, indicating that the activity level of the receptors was not responsive to the efficacy of bound ligands.

Figure 16. TDPs of $A_{2A}AR$, $A_{2A}AR[D52N]$, $A_{2A}AR[I92N]$, and $A_{2A}AR[R291Q]$ with different ligands or without ligand.

TDPs were generated from the normalized initial and final intensities.

(A) The TDPs of $A_{2A}AR$ without ligand added (apo), in complex with the antagonist ZM241385 and in complex with the agonist NECA. The X and Y axes of TDP plots represent the normalized initial and final intensities of transition events. The gradient color scheme is indicated in the rightmost bars, where the arrowhead points toward a relatively higher density, which relates to the frequency of observed transitions. "n" refers to the number of analyzed transitions. (B-D) TDPs for (B) $A_{2A}AR[D52N]$, (C) $A_{2A}AR[I92N]$, and (D) $A_{2A}AR[R291Q]$. Same presentation details as in (A).

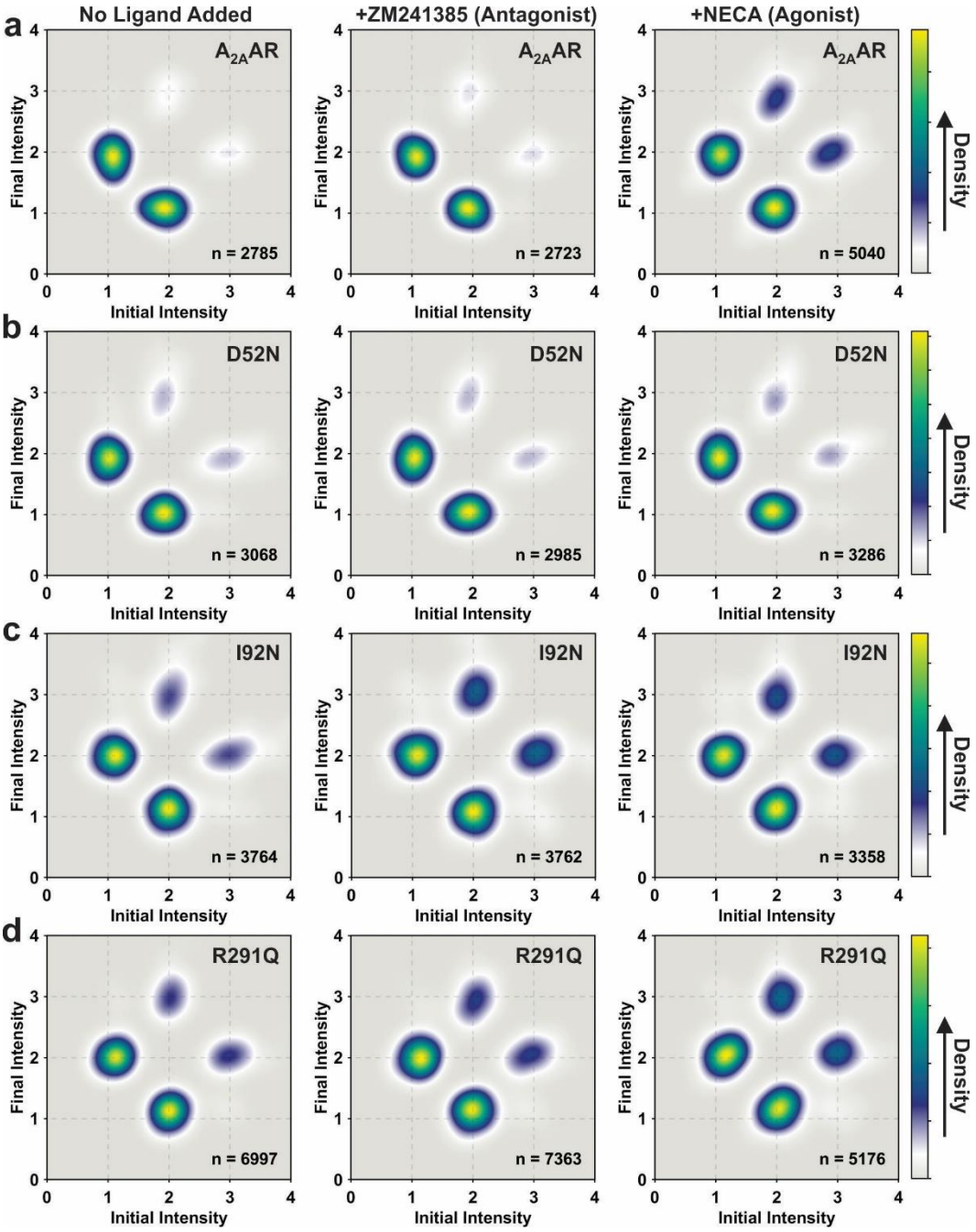

Figure 16. TDPs of $A_{2A}AR$, $A_{2A}AR$[D52N], $A_{2A}AR$[I92N], and $A_{2A}AR$[R291Q] with different ligands or without ligand.

Notably, transitions between states 1 and 3 were found to be more frequent than for $A_{2A}AR$ but still relatively rare, consisting of fewer than 3% of the total transitions (**Table S6**). These results indicate that constitutively activating mutations increase the basal level of receptor signaling by increasing the frequency of transitions to state 2, the conformational intermediate, rather than bypassing transitions to state 2 by increasing the frequency of transitions between states 1 and 3. Therefore, a conceptual framework that describes reversible sequential transitions developed to explain ligand efficacy also appears consistent with the impact of constitutively activating mutations on function-related dynamics.

3.3.5 The influence of ternary complex formation with an engineered G protein on the fluctuations of $A_{2A}AR$ and $A_{2A}AR$ variants

We next applied single-molecule fluorescence to investigate how ternary complex formation with a G protein influenced the conformational exchange of $A_{2A}AR$ and the studied $A_{2A}AR$ variants. Ternary complexes were formed by incubating the receptor in lipid nanodiscs with "mini-G_S", an engineered G protein designed to mimic the binding of full-length $G\alpha_S$ to the receptor [117]. After incubating the proteins together, the resulting complex was then added to the quartz slides for TIRF imaging experiments (**Figure 17**). See the Methods section for further details.

The addition of mini-G_S to $A_{2A}AR$ showed a marked and measurable impact on the relative areas for all fluorescence emission intensities (**Figure 18A**). Notably, for all samples of $A_{2A}AR$, addition of mini-G_S increased the area of state 3: for apo and antagonist-bound $A_{2A}AR$, from <1% in the absence of mini-G_S to 8% in the presence of

mini-G_S, and for agonist-bound $A_{2A}AR$, from 14% in the absence of mini-G_S to 21% in the presence of mini-G_S (**Figure 18A and Table S4**). For all samples of $A_{2A}AR$, in the presence of mini-G_S, we also observed a decrease in the area of state 1 and at most, a marginal impact on the area of state 2 (**Table S4**). Notably, the response of the addition of mini-G_S to $A_{2A}AR$ was distinct from the measured impact of introducing constitutively activating mutations, where we observed an increase in the area of state 2 (**Figure. 15**).

The response of $A_{2A}AR$ to the presence of mini-G_S contrasted with that of $A_{2A}AR$[D52N]. For $A_{2A}AR$[D52N], addition of mini-G_S had no measurable impact on the relative populations of the three observed states (**Figure 18B and Table S4**). This was expected because this variant has been noted to have very low G protein signaling levels even in the presence of a large concentration of a full agonist [170], likely due to the inability of this variant to form ternary complexes. The impact of this mutation on $A_{2A}AR$ has been well-documented [126, 173], and analogous mutations in the same positions of many other class A has also resulted in similar significant alterations to signaling [174]. The precise mechanism of the loss of signaling activity for $A_{2A}AR$[D52N] remains a subject of ongoing investigation, but earlier determination of the crystal structure of $A_{2A}AR$[D52N] in complex with a full agonist pointed to subtle changes in the backbone trajectory around the conserved NPXXY motif [170], and related NMR experiments noted that this mutation altered function-related conformational dynamics at the receptor intracellular surface [49].

For both $A_{2A}AR$[I92N] and $A_{2A}AR$[R291Q], addition of mini-G_S also appeared to have a smaller impact on the areas of the three observed fluorescence emission states (**Figure 18C, Figure 18D and Table S4**). For $A_{2A}AR$[I92N], a modest increase in the relative area

of state 2 and a concurrent decrease in the relative area of state 1 were observed in the presence of mini-G_S with no change in state 3 (Figure. 5c). For A_{2A}AR[R291Q], we also observed a decrease in the area of state 1 for apo and antagonist-bound A_{2A}AR[R291Q] and an increase in the area of state 2 for antagonist-bound and agonist-bound A_{2A}AR[R291Q] (**Figure 18D**). These data indicate that for the constitutively active A_{2A}AR variants, the addition of mini-G_S does not further drive the conformational equilibrium.

3.3.6 Reversible, sequential fluctuations among A_{2A}AR conformational states are maintained in the presence of G protein

We used the hidden Markov model to fit the normalized single-molecule time trajectories for A_{2A}AR samples observed in the presence of mini-G_S and generated the corresponding TDPs (**Figure 19**). For A_{2A}AR in the presence of mini-G_S, we observed an increased frequency of transitions between states 2 and 3 for both the apo receptor and antagonist-bound A_{2A}AR (**Figure. 19A**). Importantly, transitions between states 1 and 3 were again found to be rare and not populated in the TDP. This indicates that the vast majority of A_{2A}AR conformational fluctuations proceeded in a reversible, sequential manner even in the presence of a partner protein.

For A_{2A}AR[D52N], A_{2A}AR[I92N], and A_{2A}AR[R291Q], we observed at most only minor differences in the TDPs recorded for samples prepared in the absence and presence of mini-G_S (**Figure 19B, Figure 19C and Figure 19D**). As with A_{2A}AR, there was no measurable increase in the frequency of transitions between states 1 and 3 for all variants in the presence of mini-G_S, consistent with reversible sequential transitions between states.

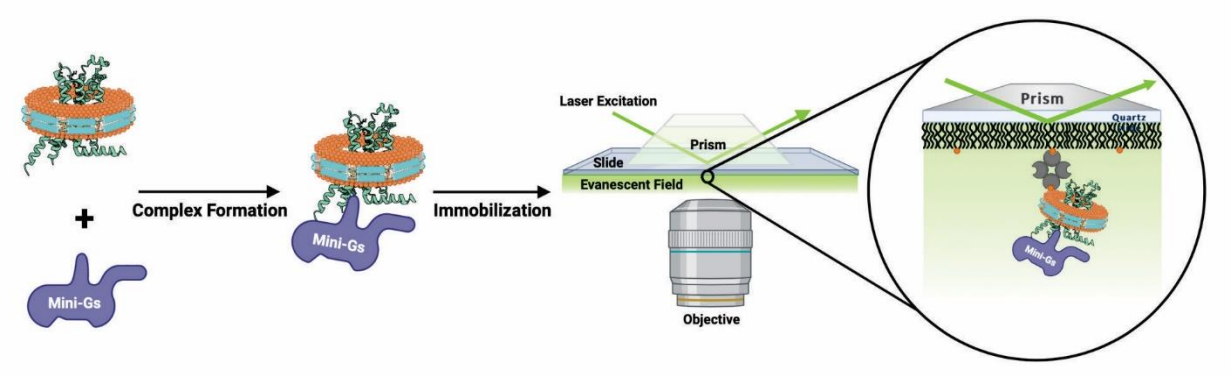

Figure 17. Schematic of SMF experiments with $A_{2A}AR$ in a ternary complex with an engineered G protein (mini-G_S).

The receptor in lipid nanodiscs was incubated with mini-G_S prior to applying the sample to a channel in a quartz slide for TIRF imaging experiments. This image was prepared with BioRender.

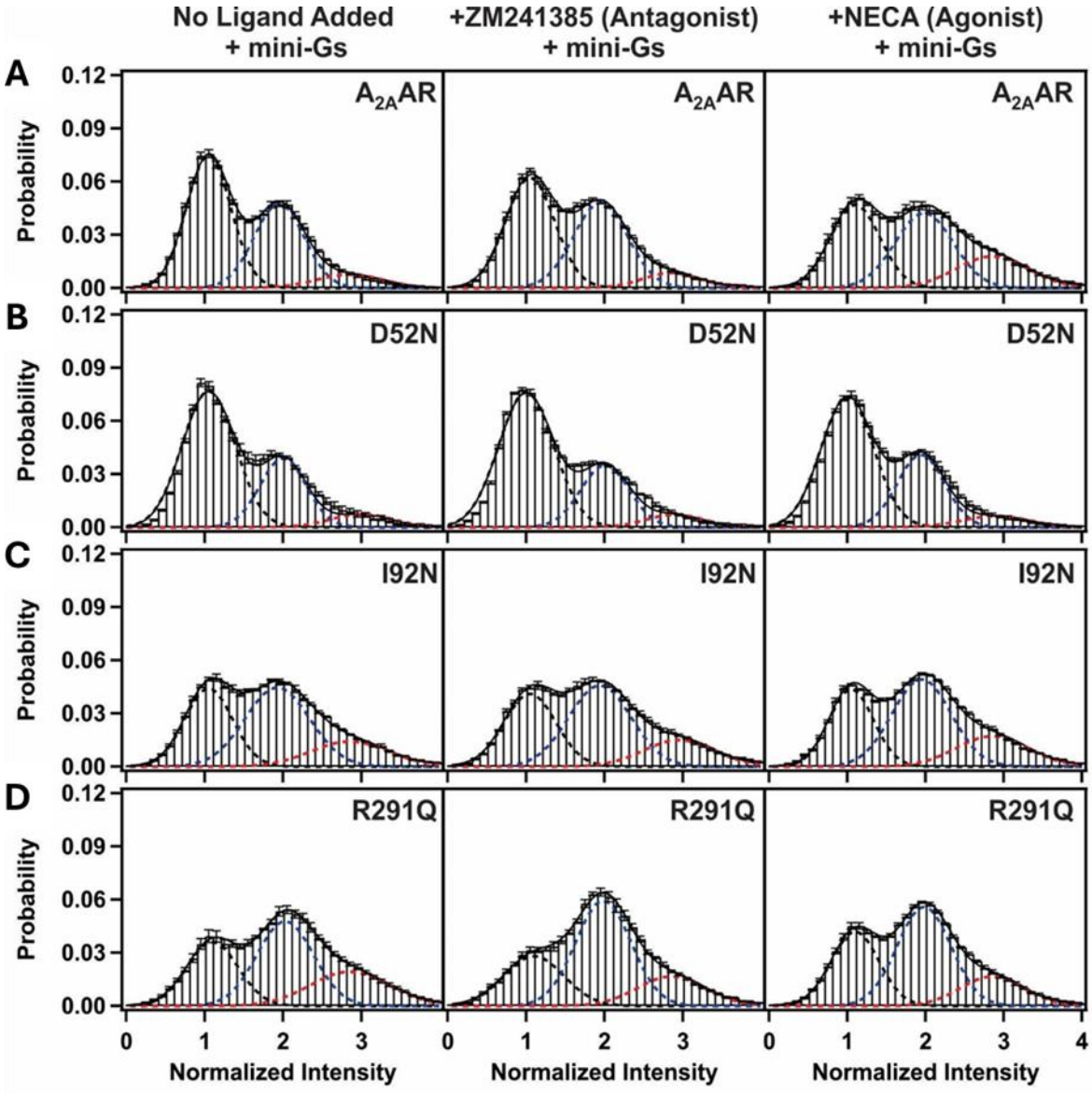

Figure 18. Single-molecule fluorescence histograms compiled from collections of individual molecules of $A_{2A}AR$, $A_{2A}AR[D52N]$, $A_{2A}AR[I92N]$ and $A_{2A}AR[R291Q]$ in the presence of Mini-G_S.

(A) Histograms compiled for $A_{2A}AR$ with no ligand added (apo), in complex with the antagonist ZM241385, and in complex with the agonist NECA in the presence of mini-GS. Same presentation details as in Fig. 2. (B-D) Histograms compiled for (B) $A_{2A}AR[D52N]$, (C) $A_{2A}AR[I92N]$ and (D) $A_{2A}AR[R291Q]$.

Figure 19. TDPs of $A_{2A}AR$, $A_{2A}AR[D52N]$, $A_{2A}AR[I92N]$, and $A_{2A}AR[R291Q]$ in the presence of mini-G_S.

TDPs were generated from the normalized initial and final intensities.

(A) The TDPs of $A_{2A}AR$ without ligand added (apo), in complex with the antagonist ZM241385 and in complex with the agonist NECA in the presence of mini-G_S. The X and Y axes of the TDP plots represent the normalized initial and final intensities of transition events. The gradient color scheme is indicated in the rightmost bars, where the arrowhead points toward a relatively higher density, which relates to the frequency of observed transitions. "n" refers to the number of analyzed transitions. (B-D) TDPs for (B) $A_{2A}AR[D52N]$, (C) $A_{2A}AR[I92N]$, and (D) $A_{2A}AR[R291Q]$ in the presence of mini-G_S. Same presentation details as in (A).

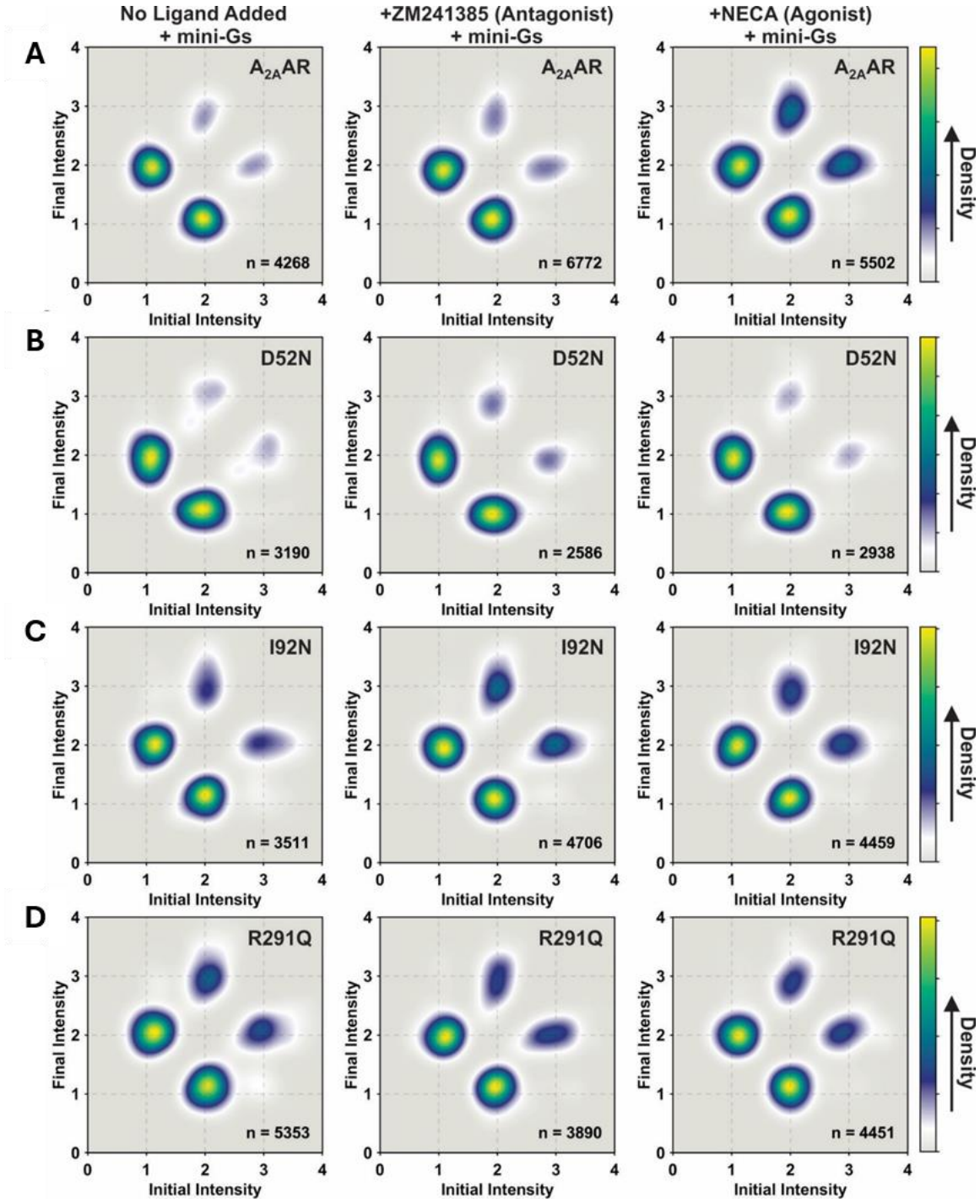

Figure 19. TDPs of $A_{2A}AR$, $A_{2A}AR$[D52N], $A_{2A}AR$[I92N], and $A_{2A}AR$[R291Q] in the presence of mini-G_S.

3.3.7 Constitutively activating mutations and the G protein shift the equilibrium towards the intermediate state

From statistical analysis of the dwell times of collections of receptors, we determined the average time spent or mean occupancy time in each state and the kinetics of transitioning among states 1, 2, and 3 for A_{2A}AR and all A_{2A}AR variants (**Figure S10 and Table S7**). For A_{2A}AR, the average time spent in state 1 was longer (~2.9 s) compared to the average time spent in states 2 or 3 for the apo receptor and for both antagonist-bound A_{2A}AR and agonist-bound A_{2A}AR (**Figure S10a and Table S7**). Similarly, the A_{2A}AR[D52N] variant also spent a longer time in state 1 (~2.9 s) (**Figure. S10A and Table S7**). Interestingly, for both the A_{2A}AR[I92N] and A_{2A}AR[R291Q] variants, we observed a shorter mean occupancy time (~1.5 s) compared with both A_{2A}AR and A_{2A}AR[D52N] (**Figure. S10A and Table S7**). While the addition of mini-G_S appeared to shorten the mean occupancy times for A_{2A}AR, especially for agonist-bound A_{2A}AR (~1.8 s), there was no impact of the addition of mini-G_S for A_{2A}AR[D52N], A_{2A}AR[I92N] or A_{2A}AR[R291Q] (**Figure 10B and Table S7**).

For nearly all samples of A_{2A}AR and A_{2A}AR variants, we observed that the dwell time histograms of state 1 and state 2 do not fit well with a mono-exponential function. Instead, a reduced chi-squared analysis showed that a bi-exponential function consisting of faster and slower transitions provided the best fit (**Table S9 to S16**). Three exceptions were observed where a mono-exponential function appeared to provide a better fit for transitions state 2 to state 1: A_{2A}AR in complex with the antagonist ZM241385, A_{2A}AR[I92N] in complex with the agonist NECA and A_{2A}AR[I92N] in complex with NECA

in the presence of mini-G_S (**Table S9 to S16**). Since both shorter and longer dwell times were observed within the same molecule, most likely this indicated that state 1 and state 2 each contain two kinetically distinct substates that share the same fluorescence intensity.

Given that the activation of $A_{2A}AR$ and its variants occurs sequentially through intermediate state 2, there was a compelling need to explore the impact of mutations and the presence of mini-G_S on the transitions between intermediate state 2 and state 1, as well as between state 2 and state 3. Because a bi-exponential function was used to fit most of the observed transitions between states 1 and 2, we first determined an average rate constant for transitions between state 1 and state 2, $k_{1\rightarrow2}$ and for the inverse transition from state 2 to state 1, $k_{2\rightarrow1}$ by weighting each rate with the observed number of transitions and determining the mean (see Methods section for further details). The values for $k_{1\rightarrow2}$ and for $k_{2\rightarrow1}$ were then used to calculate the equilibrium rate-constant ($k_{eq(1,2)}$), which we define as the ratio of $k_{1\rightarrow2}/k_{2\rightarrow1}$ (**Figure. 20a, Figure. 20, and Table S8**). In the absence of mini-G_S, the values of $k_{eq(1,2)}$ ranged from ~0.3 to ~3.2 across all $A_{2A}AR$ variants (**Figure. 20b**). For $A_{2A}AR$, the addition of the agonist NECA increased the value of $k_{eq(1,2)}$ from ~1.2 to ~2.4, consistent with the idea that agonists increase the frequency of transitions to the intermediate state. The mutation D52N showed a clear impact on the values of $k_{eq(1,2)}$, which are reduced to less than 1 for all $A_{2A}AR$[D52N] samples relative to $A_{2A}AR$, indicating this mutation decreases the frequency of transitions to state 2 from state 1 (**Figure. 20a**).

The addition of mini-G_S increased the values of $k_{eq(1,2)}$ for most samples of $A_{2A}AR$ and $A_{2A}AR$ variants. Specifically, the addition of mini-G_S increased $k_{eq(1,2)}$ for apo $A_{2A}AR$ from ~1.2 to ~2.0, and for agonist-bound $A_{2A}AR$ from ~2.4 to ~3.8. The broadly observed increase in $k_{eq(1,2)}$ is consistent with the idea that the addition of mini-G_S shifts the receptor conformational equilibrium away from an inactive conformation to more frequently populate the intermediate state. The clear exception to this observation is for $A_{2A}AR$[D52N], where no increase in $k_{eq(1,2)}$ was observed for apo $A_{2A}AR$[D52N] or in a complex with NECA (**Figure. 20B**). The reduction in the frequency of transitions to state 2 for $A_{2A}AR$[D52N] is consistent with the known low G protein signaling for this variant[170] and further confirms the importance of state 2 as critical to the function of active $A_{2A}AR$. Both $A_{2A}AR$[I92N] and $A_{2A}AR$[R291Q] showed an increase in $k_{eq(1,2)}$ for complexes with the agonist NECA relative to the apo protein or antagonist-bound receptor (**Figure. 20A**). $A_{2A}AR$[I92N] showed a modest increase in $k_{eq(1,2)}$ for the apo protein and agonist-bound receptor in the presence of mini-G_S (**Figure. 20B**) and the $k_{eq(1,2)}$ for $A_{2A}AR$[R291Q] did not show a significant change upon the addition of mini-G_S for the agonist complex but did show an increase for the complex with the antagonist ZM241385 (**Figure. 20B**).

Unlike the rate constants governing transitions between states 1 and 2, our reduced chi-squared analysis indicated that the rate constants for transitions between states 2 and 3 were better described by a mono-exponential fit rather than a bi-exponential fit (**Figure S10 and Table S9 to S16**). Thus, unlike states 1 and 2, no additional substates were observed for state 3. For nearly all samples, the rate constants from state 2 to state 3, $k_{2\rightarrow3}$were similar to the rate constants for the reverse process,

$k_{3\rightarrow2}$. Defining $k_{eq(2,3)}$ as the ratio of $k_{2\rightarrow3}/k_{3\rightarrow2}$, we found that the range of values of $k_{eq(2,3)}$ for samples prepared without mini-G_S spanned from ~0.5 to ~1.5, with most values near 1 and the lowest value of 0.5 for apo $A_{2A}AR$ (**Figure. 20C and Table S7**). The range of values of $k_{eq(2,3)}$ was significantly narrower than the range of values for $k_{eq(1,2)}$ for all receptors and for all sample preparations (**Figure. 20A, Figure. 20B, and Figure S10**). This indicates that the effect of mutations and of the addition of mini-G_S had a proportionally greater impact on the rate constants between states 1 and 2 compared with the rate constants between states 2 and 3.

3.4 Discussion

Analysis of single-molecule fluorescence emission traces of human $A_{2A}AR$ in lipid nanodiscs revealed the presence of three distinct states both in the absence and presence of mini-G_S, with no additional states observed upon the addition of mini-G_S (**Figure 15, Figure 18, Figure S7 and Figure S8**). We are confident in concluding that no additional states were observed, because in our analysis we observed unique states defined ~200 a.u. apart, well outside of the typical fluctuations observed that were not associated with different states, ± 30 to 40 a.u., which is consistence with previous results [165]. Notably, the frequency of transitions to state 3 exhibited a significant increase in the presence of mini-G_S. We also observed a significant increase in the relative area of emission state 3 for the $A_{2A}AR$ variants containing CAMs (**Figure 15 and Table S4**).

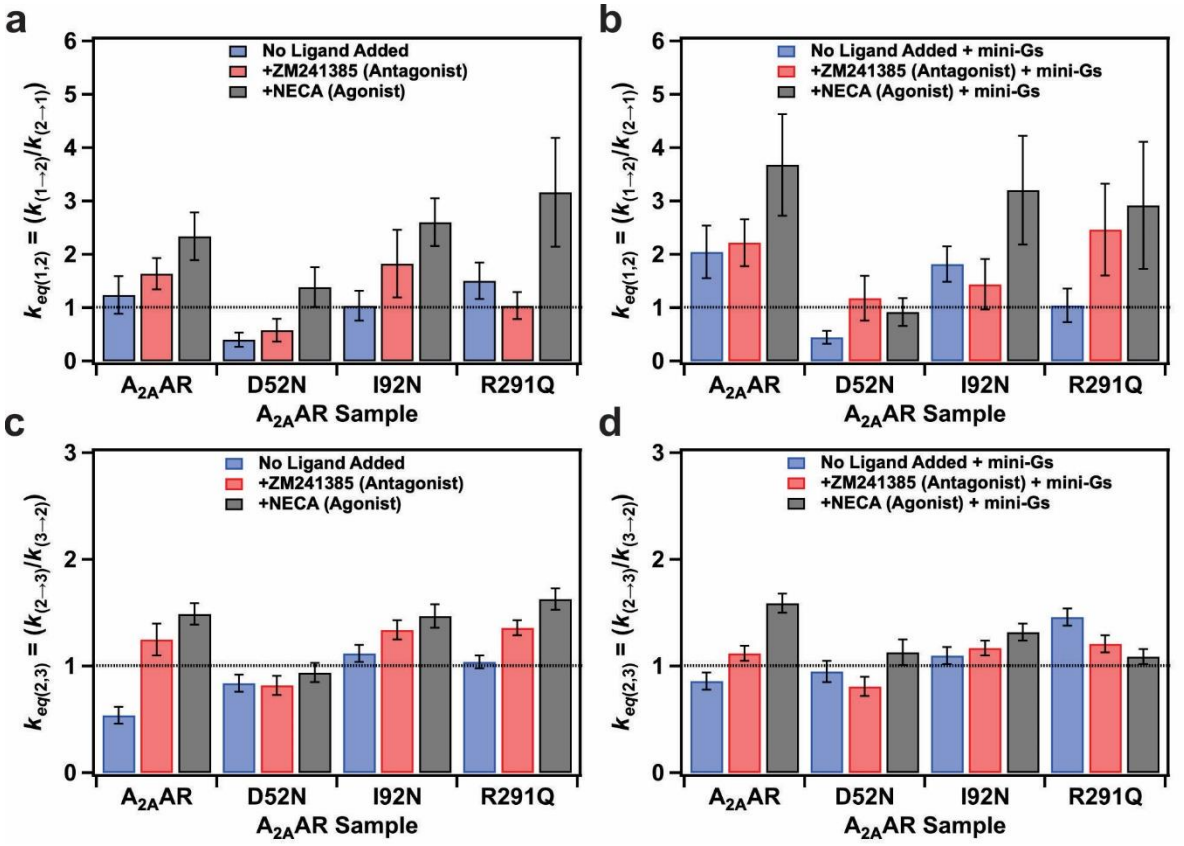

Figure 20. Ratios of equilibrium rate-constants between consecutive states.

(A and B) Ratio of transition rate constants between states 1 and 2 for samples (A) without mini-G_S and (B) with mini-G_S. (C and D) Ratio of transition rate constants between states 2 and 3 for samples (C) without mini-G_S and (d) with mini-G_S. The vertical scales in panels c and d were expanded for clarity. See Supplementary Fig. 7 for a plot of panels c and d on the same scale as panels (A) and (B). For all panels, error bars indicate the calculated standard deviation. The dotted horizontal lines indicate values of the rate-constants equal to 1.

These findings collectively indicate that the conformation of $A_{2A}AR$ in state 3 likely corresponds to the conformation of active $A_{2A}AR$ within the assembled ternary complex with mini-G_S. Interestingly, this observation aligns with a recent NMR study demonstrating that complex formation with an agonist alone is adequate to induce a global conformation of $A_{2A}AR$ that resembles the conformation observed in a ternary complex [164].

Concurrently, we observed identical relative areas of observed emission intensities of states 1 and 2 for both apo $A_{2A}AR$ and antagonist-bound $A_{2A}AR$ (**Figure 15 and Table S4**), indicating ZM241385 does not change the distribution of fluorescence emission states. This result appears in line with earlier ^{19}F-NMR studies of $A_{2A}AR$ labeled with TET at position C289 [56, 163] and also in line with single-molecule FRET observations measured on the sub-millisecond timescale [167]. In contrast, ^{19}F-NMR studies of $A_{2A}AR$ labeled at position V229C showed an inverse agonist effect of ZM241385, which was attributed to a higher basal activity reported for samples from that study [104]. Interpretation of the data in the current study are in line with relatively low basal activity reported for $A_{2A}AR$ [173].

In the context of the agonist bound $A_{2A}AR$ ternary complex, we have also noted the persistence of a finite occupancy for state 1. One possible implication of this observation is the potential for rapid dissociation and subsequent re-association of mini-G_S, accompanied by corresponding conformational changes in the receptor. However, based on our experience, such events have not been observed in either the analytical characterization of $A_{2A}AR$ ternary complexes or in earlier NMR studies. An alternative interpretation of this data suggests the presence of multiple conformations of $A_{2A}AR$ within

the assembled ternary complex, leading to varying fluorescence intensities. This interpretation aligns more closely with findings from studies of alternative GPCR conformations in ternary complexes, as observed in cryo-EM structures of a neurotensin receptor [175] and β_2AR [176]. The fluorescence probe employed in our study exhibits sensitivity to conformational changes pertinent to receptor function occurring at the intracellular surface. Analogous to spectroscopic methodologies like ^{19}F-NMR, which utilize probes targeted at specific sites, it remains a possibility that subtle structural variations could be present in other receptor regions, such as the transmembrane domain or extracellular surface. This also indicates that while the mean fluorescence intensity observed for state 2, referred as the intermediate state, remains consistent across all samples, subtle structural variations in the intermediate state conformation could exist for different variants or in the absence and presence of the mini-G_S protein. Previously, we had proposed a similar hypothesis to rationalize potential structural differences between the intermediate state of agonist-bound and antagonist-bound A_{2A}AR.[165]

The transition density plots shown in Figure. 16 provide clear evidence that CAMs do not increase the frequency of transitions between states 1 and 3. Instead, both the I92N and R291Q mutations increase the frequency of transitions to the intermediate state, state 2, as depicted in Figure. 21. It is notable that despite the I92N and R291Q mutations are located in distinct regions of the receptor, both mutations exert similar effects on the transition frequency to the intermediate state. These findings support the idea that both I92 and R291 are crucial elements within an allosteric pathway connecting the orthosteric drug binding site and intracellular surface. This interpretation aligns with previous NMR

investigations involving R291 and theoretical analysis involving I92 [169]. Earlier investigations utilizing single-molecule fluorescence indicated that the activation of $A_{2A}AR$ by agonists followed a sequential and reversible step-wise process [165]. Findings from our current study demonstrate align with this sequential activation model, reinforcing its consistency with visualizing the influence of CAMs and addition of the partner mini-G_S protein.

Measurement of the mean occupancy times of $A_{2A}AR$[I92N] and $A_{2A}AR$[R291Q] revealed significantly reduced lifetimes of state 1 for these two variants, including for the apo receptors and their complexes with the antagonist ZM241385 (**Figure S10**). Concurrently, examination of the dwell time data of the same variants indicated an increased number of transitions from state 1 to state 2 for both $A_{2A}AR$[I92N] and $A_{2A}AR$[R291Q] (**Figure 20 and Figure S10**). These findings align with the notion that constitutively activating mutations decrease the energy barrier between state 1 and state 2 by raising the relative energy of state 1, thereby destabilizing it. For $A_{2A}AR$, we observed a decreased mean occupancy time for state 1 for the agonist complex in the presence of mini-G_S, suggesting that addition of agonists and mini-G_S also increase the relative energy of state 1. Notably, the mean occupancy time of state 1 for $A_{2A}AR$[D52N] remained relatively higher even in the presence of both an agonist and mini-G_S (**Figure S10**). Our observation of the longer mean occupancy time for $A_{2A}AR$[D52N] appears consistent with the observation of attenuated conformational dynamics observed by NMR for the same variant [49].

Analysis of the dwell time data for $A_{2A}AR$ and all $A_{2A}AR$ variants for transitions between states 1 and 2 required bi-exponential fits, consisting of both a slow transition and a fast transition. This indicated the presence of two sub-populations for both states 1 and 2, which each exhibited similar fluorescence emission intensities (**Figure 20**). This observation resembles earlier single-molecule fluorescence studies of the β_2AR, where analogous slow and fast transitions were observed between two fluorescence emission states [87, 166]. It is intriguing to speculate whether similar observations will be reported for additional class A GPCRs in future studies.

Our findings underscore a significant advantage of single-molecule fluorescence in elucidating the mechanisms of GPCR signal transduction. Specifically, SMF allows one to determine the sequential order of molecular events involving multiple distinct protein conformations. Existing literature, particularly studies employing spectroscopic techniques such as NMR spectroscopy, has established a connection between the conformational equilibria of GPCRs and their signaling functions [95]. By confirming and complementing these observations, single-molecule fluorescence adds valuable information on the energy landscape of GPCR activation and signaling [109, 121, 167, 177]. In our study, the use of single-molecular fluorescence enabled us to identify a crucial intermediate state essential for $A_{2A}AR$ activation. Furthermore, it facilitated the assessment of how the introduction of a G protein or the presence of activating or inactivating mutations influenced the conformational equilibria, favoring or inhibiting the population of the intermediate state (**Figure 21**). Consequently, the functional impact of

mutations on A_{2A}AR can be directly linked to their effect on the frequency of transitions to the intermediate state.

Over 60 crystal and cryo-EM structures of human A_{2A}AR have been publicly released, including complexes with antagonists, agonists, and ternary complexes with agonists and G proteins. Further, multiple crystal structures are available of A_{2A}AR in complex with an agonist but not G protein, which have been proposed to be “active-like” or intermediate states [116, 118]. Despite this, our modeling of single-molecule fluorescence data showed that a structure of this crucial intermediate state remains unknown [165]. Furthermore, the relationship between the population of the intermediate state and the A_{2A}AR function suggests an innovative approach for testing or designing mutations with novel properties by measuring the impact of novel mutations on the intermediate state. Further structural elucidation of intermediate states may also present new opportunities for targeted drug discovery.

3.5 Methods

3.5.1 Molecular cloning

The gene for human A_{2A}AR (1-316) was cloned into a pPIC9K vector (Invitrogen) using the restriction sites BamHI and NotI. The receptor sequence included a single amino acid replacement to remove a putative glycosylation site (N154Q), an N-terminal FLAG tag, and a 10 X C-terminal HIS tag. This sequence was used as a template to generate the variants A_{2A}AR[A289C], A_{2A}AR[A289C, R291Q], A_{2A}AR[A289C,I92N] and A_{2A}AR[A289C,D52N] using site-directed mutagenesis with the Accuprime *Pfx* SuperMix (ThermoFisher Scientific) and primers listed in Table S3.

Figure 21. Schematic of the impact of agonists, mutations, and presence of mini-G_S on the conformational equilibria describing A_{2A}AR activation for (A) addition of agonists, (B) presence of activating mutations, (C) presence of inactivating mutations, and (D) addition of agonists and mini-G_S.

The relative sizes of the arrows indicate their preferred direction in the equilibrium. The dashed green box highlights the transitions between states 1 and 2, which showed the largest magnitude of differences among the observed samples.

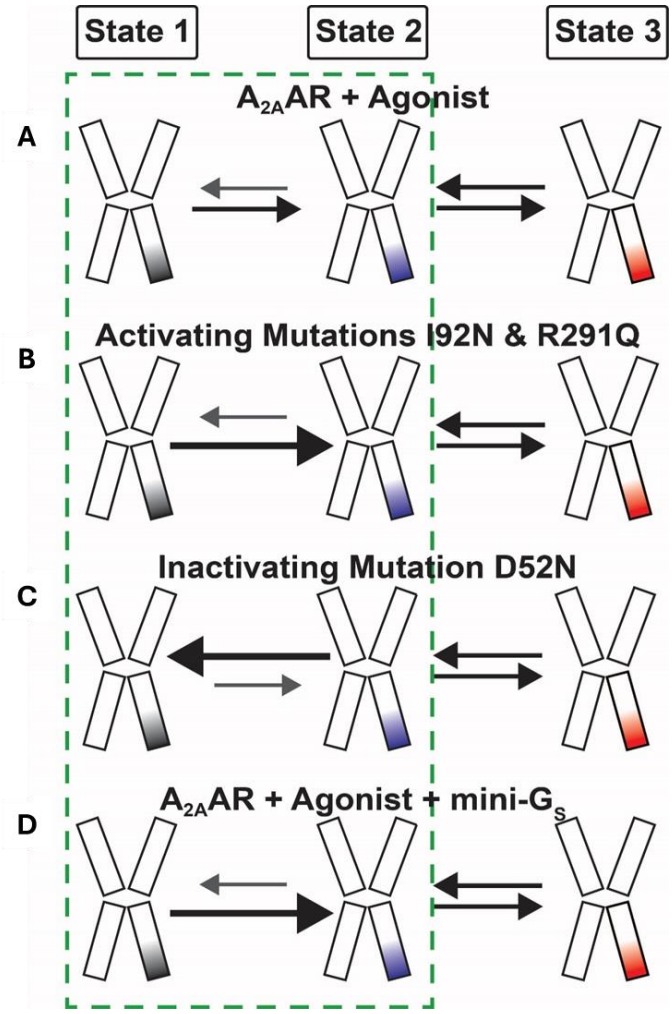

Figure 21. Schematic of the impact of agonists, mutations, and presence of mini-G_S on the conformational equilibria describing $A_{2A}AR$ activation for (A) addition of agonists, (B) presence of activating mutations, (C) presence of inactivating mutations, and (D) addition of agonists and mini-G_S.

3.5.2 Transformation to Pichia pastoris and colony selection

Recombinant pPIC9K plasmids containing A_{2A}AR variants were transformed into the *Pichia pastoris* strain BG12 (Biogrammatics) using electroporation. For each variant, 20-25 colonies were selected and plated individually to identify high-expressing clones using a Western blot assay [49, 102, 171]. Glycerol stocks of colonies expressing the highest levels of receptor were prepared and stored at -80 °C.

3.5.3 A_{2A}AR expression and purification

All A_{2A}AR variants were expressed using protocols reported in earlier studies [49, 171]. For each expressed A_{2A}AR variant, 400 µL of a glycerol stock was used to inoculate 4 mL of buffered minimal glycerol (BMGY) media. The cultures were incubated at 30 °C for 48 hours, shaking at 200 RPM. After 48 hours, the 4 mL cultures were used to inoculate 50 mL of BMGY media. These cultures were allowed to grow at 30 °C for 60 hours shaking at 200 RPM. The 50 mL cultures were used to inoculate 500 mL of BMGY media, and the 500 mL cultures were allowed to grow for 48 hours at 30 °C, shaking at 200 RPM. After 48 hours, the 500 mL cultures were centrifuged at 3000 x g for 15 minutes, the supernatant was discarded, and the pellets were resuspended in 500 mL fresh buffered minimal methanol (BMMY) media without methanol. To remove trace amounts of glycerol remaining in the cultures, the cells were allowed to grow for 6 hours at 28 °C and 200 RPM shaking. Subsequently, aliquots of 0.5% w/v methanol were added to induce protein expression three times at 12-hour intervals. 12 hours after the last induction, the cultures were centrifuged at 3000 x g for 15 minutes, and the cells were harvested, frozen, and stored at -80 ºC for future use.

Cell pellets were resuspended in buffer (50 mM sodium phosphate pH 7.0, 100 mM NaCl, 5% glycerol (w/v), and in-house prepared protease inhibitor cocktail solution) and lysed via two passes through a cell disrupter (Pressure Biosciences) operating at 40 PSI. Insoluble fractions from the lysed cells were centrifuged at 200,000 x g for 30 minutes, the solution was decanted, and the pellets were stored at -80 ºC.

To purify A_{2A}AR variants, membrane pellets were resuspended in buffer (10 mM HEPES pH 7.0, 10 mM KCl, 20 mM $MgCl_2$, 1 M NaCl) and centrifuged at 200,000 x g. Then the pellets were resuspended in the same buffer containing 1 mM theophylline and protease inhibitor and incubated for 30 minutes at 4 °C. Resuspended membranes were mixed in a ratio of 1:1 with solubilizing buffer (50 mM HEPES pH 7.0, 500 mM NaCl, 0.5% (w/v) n-Dodecyl-β-D-Maltopyranoside (DDM), and 0.05% cholesteryl hemisuccinate (CHS)) for 6 h at 4 °C. Insoluble material was removed by ultracentrifugation at 200,000 x g for 30 minutes. The resulting solution containing solubilized receptors was treated with Co^{2+}-charged affinity resin (Talon, Clontech) and 30 mM imidazole and incubated at 4 °C with gentle rotation. The resin was then washed with 25 column volumes of wash buffer 1 (50 mM HEPES pH 7.0, 500 mM NaCl, 10 mM $MgCl_2$, 30 mM imidazole, 8 mM ATP, 0.05% DDM, and 0.005% CHS) followed by 20 column volumes of wash buffer 2 (25 mM HEPES pH 7.0, 250 mM NaCl, 5% glycerol, 30 mM imidazole, 0.05% DDM, 0.005% CHS, and an excess of ligand). A_{2A}AR variants were eluted in a third buffer (50 mM HEPES pH 7.0, 250 mM NaCl, 5% glycerol, 300 mM imidazole, 0.05% DDM, 0.005% CHS, and ligand). Following this, samples were exchanged into buffer 4 (25 mM HEPES pH 7.0, 75 mM NaCl, 0.05% DDM, 0.005% CHS, and ligand) using a PD-10 desalting

column (Cytiva) equilibrated with buffer 4. Saturating concentrations of ligands were used for buffers containing ligands. For apo samples, no ligand was added to any of the buffers.

3.5.4 Nanodisc assembly

Nanodisc assembly was carried out according to protocols from earlier studies [73, 178]. For expression and purification of the scaffold protein MSP1D1, a single colony of *E. coli* BL21(DE3) containing MSP1D1 in pET28a vector was used to inoculate 10 mL LB medium with 50 µg/mL Kanamycin. After 12-14 h of incubation at 37°C with shaking at 200 RPM, this culture was used to inoculate 1 L Terrific Broth (TB) medium containing kanamycin in a baffled flask and was incubated at 37°C with shaking at 200 RPM until the optical density (OD) reached 0.6-0.8. MSP1D1 expression was induced by adding 1 mM final concentration of isopropyl β-D-1-thiogalactopyranoside (IPTG) to the cells, and incubation continued for 4 hours at 37°C. Cells were harvested by centrifuging at 4,000 × g for 30 min at 4°C. For lysis, cells were resuspended in MSP lysis buffer 1(50 mM Tris-HCl, pH 8.0, 500 mM NaCl, 1 mM EDTA, 1% triton X-100, and in-house protease inhibitor solution) and passed through a cell disrupter (Pressure Biosciences) operating at 20,000 PSI. Lysed cells were pelleted at 20,000 x g for 40 minutes. The supernatant was added to Ni-NTA resin pre-equilibrated with wash buffer 2 (50 mM Tris-HCl, pH 8.0, 500 mM NaCl, and 1% (w/v) Triton X-100), and the mixture was incubated at 4°C with rotation for 2 hours. The resin was washed with 5 CV wash buffer 2 followed by 5 CVs wash buffer 3 (50 mM Tris-HCl, pH 8.0, 500 mM NaCl, and 50 mM cholate), 5 CVs of wash buffer 4 (50 mM Tris-HCl, pH 8.0, and 500 mM NaCl) and finally 5 CVs of wash buffer 5 (50 mM Tris-HCl, pH 8.0, 500 mM NaCl, and 20 mM imidazole). MSP1D1 was

eluted in buffer (50 mM Tris-HCl, pH 8.0, 500 mM NaCl, and 500 mM imidazole) and then dialyzed in a 10 kDa MWCO dialysis tube using buffer 7 (50 mM Tris-HCl, pH 8.0, 20 mM NaCl, and 0.5 mM EDTA). TEV protease was then added to MSP1D1 in a 1:100 ratio (w/w), and the solution was incubated overnight at 4 ºC. The next morning, Ni-NTA was added to the solution and the mixture was run through a gravity column. MSP1D1 was collected as the flow-through. MSP1D1 was then dialyzed again in buffer 8 (20 mM Tris-HCl, pH 8.0, 100 mM NaCl, and 0.5 mM EDTA) for 4 hours at 4 ºC. MSP1D1 was concentrated to 1 mM and aliquoted stocks were stored at -80 ºC for future use.

To prepare the stock solutions of lipids, dried lipids were dissolved in cholate buffer (25 mM Tris-HCl, pH 8.0, 150 mM NaCl, and 200 mM sodium cholate) to a concentration of 100 mM. $A_{2A}AR$ (27 μM in DDM/CHS mixed micelles), lipids, and MSP1D1 were combined at a molar ratio of 1:5:250 and incubated for 1-2 hours at 4 °C with gentle rotation. After incubation, pre-washed bio-beads (Bio-Rad Laboratories) were added, and the mixture was incubated overnight at 4 °C. Following the overnight incubation, the bio-beads were removed from the solution and Ni-NTA resin (GoldBio) was added and incubated with the mixture for 24 hours at 4 °C. Following this, the resin was washed with 2 CVs of nanodisc wash buffer (50 mM HEPES, pH 7.0, 150 mM NaCl, and 10 mM imidazole), and nanodiscs containing $A_{2A}AR$ were eluted with nanodisc elution buffer (50 mM HEPES, pH 7.0, 150 mM NaCl, 300 mM imidazole and ligand). Samples were then exchanged into a final buffer containing 25 mM HEPES pH 7.0, 75 mM NaCl, and excess ligand.

3.5.5 Mini-G_S expression and purification

Human mini-G_S containing an N-terminal 6X His tag and TEV protease recognition sequence was expressed and purified according to protocols from previous publications [117, 179]. A single colony of the *E. coli* strain BL21(DE3) RIL containing mini-G_S in a pET28a vector was inoculated in 4 mL LB media supplemented with 0.2% glucose, 34 µg/mL chloramphenicol and 100 µg/mL carbenicillin and incubated at 37 ºC for 8 hours. This culture was used to inoculate 75 mL of the same media. The cells were allowed to grow at 30 ºC overnight shaking at 200 RPM. The next morning, the cells were harvested and resuspended in 1 L M9 minimal media and allowed to grow at 30 ºC, with 200 RPM shaking for 5-6 hours until the OD reached ~0.8. To induce the protein expression, 50 µM IPTG was added to the culture and the cells were incubated at 25 ºC for 16 hours with 200 RPM shaking. Cells were then harvested and stored at -80 ºC for future use.

Cells were lysed in buffer (25 mM Tris-HCl, pH 8.0, 150 mM NaCl, 1 mM $MgCl_2$, 5 µM GDP, protease inhibitor) with a cell disruptor (Pressure Biosciences) operating at 22 kPSI. The lysate was pelleted at 35,000 x g for 30 minutes. The supernatant was collected and incubated with Ni-NTA resin overnight at 4 °C. The next morning, the resin was washed with 20 CVs of wash buffer (25 mM Tris-HCl pH 8.0, 500 mM NaCl, 1 mM $MgCl_2$, 5 mM imidazole, 5 µM GDP, and 2 mg/mL iodoacetamide). The protein was then eluted with buffer (25 mM Tris-HCl pH 8.0, 250 mM NaCl, 1 mM $MgCl_2$, 250 mM imidazole, 10% (v/v) glycerol, and 5 µM GDP) and exchanged into a different buffer (25 mM Tris-HCl pH 8.0, 100 mM NaCl, 1 mM $MgCl_2$, 10% (v/v) glycerol, 5 µM GDP). The tobacco etch virus (TEV) protease was added to the solution at a 1:50 ratio (TEV: Mini-G_S) and

incubated for approximately 16 hours at 4 ºC. Following this, Ni-NTA resin was added and incubated with the protein. The resin was washed with additional buffer and cleaved mini-G_S was collected as the flow through. Mini-G_S was further purified using gel-filtration with buffer (20 mM HEPES pH 8.0, 150 mM NaCl, 5 mM $MgCl_2$, 1 mM EDTA, 10% (v/v) glycerol, and 5 µM GDP). Purified fractions containing the protein were concentrated to 50 µM, frozen, and stored at -80 ºC for future use.

3.5.6 A_{2A}AR-mini-G_S complex formation

Formation of the A_{2A}AR-mini-G_S ternary complex was carried out by adapting protocols described in earlier publications [117, 179]. Nanodiscs containing A_{2A}AR variants were combined with a 1.3-fold molar excess of mini-G_S, 1 mM $MgCl_2$, and apyrase (0.2 U) and incubated 4 to 6 hours at 4 ºC.

3.5.7 A_{2A}AR single molecular TIRF experiment

The A_{2A}AR-nanodisc complexes containing 5% biotin-PE were immobilized on polyethylene glycol (m-PEG-SVA and 3% biotin-PEG-SVA) passivated quartz slides using biotin-streptavidin interactions. Detailed steps describing the cleaning and PEG passivation of the slides were described in our previous studies.[165, 171] First, the surface of slides and coverslips was activated by 1M potassium hydroxide solution, silanized by incubating them in a 3% aminopropyltriethoxysilane (APTES) solution. The silanized surfaces were passivated with mPEG-SVA and Biotin-PEG-SVA solution prepared in 100 mM sodium bicarbonate buffer in the dark overnight. Finally, slides and coverslips were rinsed with deionized water, dried with nitrogen, and stored at -20 ºC.

Fluorescence time traces were recorded for Cy3-labeled A_{2A}AR, A_{2A}AR[D52N], A_{2A}AR[I92N], and A_{2A}AR[R2891Q] samples with no ligand added (apo) and for complexes with the antagonist ZM241385 and the agonist NECA. We used a customized prism-based TIRF imaging system based on an inverted IX73 microscope (Olympus) and customized TIRF stage (TIRF Labs Inc., Cary, NC, U.S.A.) for data acquisition.[165, 171] Double-sided tape was used to prepare the flow chamber on the PEGylated quartz surface, then Cy3-labeled A_{2A}AR-nanodisc complexes were applied and tethered to the surface by biotin and streptavidin interactions. After sample immobilization, the sample chamber was washed with imaging buffer (25 mM HEPES pH 7.5, 75 mM NaCl, 2 mM Trolox, and saturating concentration of ligand or no ligand added) and flushed with glucose oxidase and a catalase oxygen scavenging system (OSS) to increase the photostability of the dye. For TIRF experiments with mini-G_S, the preformed ternary complex was diluted in imaging buffer containing 1 mM $MgCl_2$, apyrase (0.2 U), and mini-G_S, washed and flushed with 50 μM ligand and additional 12.5 nM mini-Gs in OSS-containing imaging buffer with 1 mM $MgCl_2$ and apyrase (0.2 U) to guarantee the stability of the complex. The immobilized Cy3-labeled samples were excited by a green laser (532 nm), and the emission signals were collected on an EMCCD camera (Andor Technology) in real-time [165, 171].

Custom-built data acquisition and visualization programs written in IDL software (Harris Geospatial Solutions, Inc.) were used to record single-molecule videos and process single-molecule time trajectories (http://ha.med.jhmi.edu/resources/). We selected the dynamic single-molecule traces with single-step photobleaching and

normalized with the lowest intensity state for further analysis. We then use the 'maximum-likelihood Hidden Markov model (HMM)' fitting to distinguish the states as described previously [120, 165].

3.5.8 Histogram analysis

For the histogram analysis in each condition, the normalized population intensities in the histograms were fit to Gaussian distributions using the Multipeak Fit 2 function in the Igor Pro software (version 8.04, Wavemetrics, Lake Oswego, OR, USA) as described previously [165, 171]. In more detail, we used the "Find Peaks" algorithm in Igor Pro to locate the number of peaks and fit those peaks using the mean conformational states as peak centers as determined from analysis of the transition density plots (TDP). The TDPs were generated by a custom-written script in MATLAB (**Figure 16 and Figure 18**). The peak position centers are better defined by the TDP analysis because they are better resolved in these 2-dimensional correlations. We then revisited the histogram analysis by using the peak center values determined from the TDP as input and allowing all other parameters to vary. We then used Igor's "Multipeak Fit 2" function, $y(x) = y_0 + \sum_{i=2}^{3} A_i \cdot e^{-\left(\frac{x-\mu_i}{\sigma_i}\right)^2}$, to fit the Gaussian distributions. In this equation, y_0 is the baseline, i is the number of the Gaussian peaks ($i = 2$ or 3), A_i is the peak height or amplitude, μ_i is the peak center and, σ_i is the peak width. The goodness of the fit was evaluated by a Chi-Squared analysis. The area of individual peaks was calculated from the A_i and σ_i values obtained from the fit.

3.5.9 Dwell time analysis

The TDP shown in Figures 16 and 18 are used to define the cut-off values. These values were then used to separate the dwell time data generated by the HaMMy code into the corresponding state transitions (e.g., state 1 to 2, state 1 to 3, etc.). The dwell times for each state transition were then plotted as histograms whose bin widths were calculated by the Freedman-Diaconis rule, bin width $= 2 \cdot IQR(x)/\sqrt[3]{n}$, where $IQR(x)$ is the interquartile range of the sample data x and n is the number of observations in the data [180]. Then, the histograms were fitted by both the mono-exponential and bi-exponential decay fits whose equations were given by, $A \cdot e^{-k \cdot x}$ and $A_1 \cdot e^{-k_1 \cdot x} + A_2 \cdot e^{-k_2 \cdot x}$ respectively where A, A_1 & A_2 are the amplitudes of the fit, and k, k_1 & k_2 are the rate constants calculated from the fit. The amplitude values in the dwell-time analysis correspond to the number of transitions between each state (for example, A_1 is the number of transitions with the rate constant k_1). To analyze the bi-exponential fit, we normalized the two amplitude values and converted them to percentages, such that $A_1 + A_2 = 100\%$ (**Table S9 to S16**). The goodness of fits was evaluated by reduced chi-square analysis. The histograms, corresponding fits, and chi-square test results were performed using Igor Pro software (version 8.04, Wavemetrics, Lake Oswego, OR, USA). In the case of bi-exponential fits, the two fit constants, k_1, and k_2 are averaged by the corresponding amplitudes A_1 and A_2, and is given by, ${}^{1}/_{k} = {}^{A_1}/_{k_1} + {}^{A_2}/_{k_2}$ [181]. Based on the chi-squared test results for different conditions, we selected either mono-exponential or bi-exponential fits and used them for the final calculation of equilibrium rate-constant ratio $k_{eq(i,j)}$ (ratio of the rate constant from state i to state j to the rate

constant from state j to state i) for each state transition. The equilibrium rate-constant ratio for each condition and each state-transitions are shown in **Figure 21**, Supplementary **Figure 9 to Figure 11**, and are tabulated in **Table S9 to S16**.

3.5.10 Radioligand binding experiments

Radioligand binding assays were performed with the same samples of $A_{2A}AR$ and $A_{2A}AR$ variants used for single-molecule fluorescence experiments. For all competition binding experiments, increasing concentrations of cold ligands (NECA or ZM241385) were incubated with 0.5 nM of radioligand ([^{3}H]ZM241385 (American Radiolabeled Chemicals, St. Louis, MO) or [^{3}H] CGS21680 (Perkin Elmer, Waltham, MA)) and with 0.125-0.25 µg of nanodiscs containing $A_{2A}AR$ in buffer (25 mM HEPES pH 7.0 and 75 mM NaCl) for 60 min at room temperature. Binding reactions were terminated by filtration using the Microbeta filtermat-96 cell harvester (PerkinElmer, Waltham, MA), and radioactivity was measured using a MicroBeta2 microplate counter (PerkinElmer, Waltham, MA). Specific binding at $A_{2A}AR$ was determined as the difference in binding obtained in the absence and presence of 10 µM ZM241385. IC_{50} values were determined using a nonlinear, least-square regression analysis in Prism 8 (GraphPad Software, Inc.). The K_D or K_I values were calculated from the IC_{50} using the Cheng−Prusoff equation [142]. Error bars were calculated as the standard error of the mean (s.e.m) n $\geq$ 3 independent trials.

3.6 Acknowledgements

This work was funded by NIH grants R35GM138291 (M.T.E., N.G.P., A.R.) and R35GM142946 (R.L., S.W.)

CHAPTER VI. MOLECULAR DYNAMICS OF HUMAN A_{2A} ADENOSINE RECEPTOR IN NATIVE MAMMALIAN MEMBRANE ENVIRONMENT

4.1 Abstract

The lipid environment surrounding membrane proteins offers lateral pressure and close interactions, which are crucial for maintaining their functions. Current dynamic studies of GPCRs primarily focus on micelle and MSP-based nanodisc complexes. In this study, we utilized co-polymer lipids particles to maintain the native membrane environment surrounding the A_{2A}AR. We successfully purified both A_{2A}AR-DIBMALP (DIBAM lipid particle) and A_{2A}AR-SMALP (SMA lipid particle) complexes. Our findings suggest that SMALP exhibits higher solubilization of membrane proteins, while DIBMALP results in larger-sized complexes, providing a larger lipid environment for A_{2A}AR. Using single-molecule fluorescence resonance energy transfer (smFRET), we observed the influence of agonists and G protein on the dynamic interactions between A_{2A}AR transmembrane helices IV and VI in the native membrane environment. Preliminary data indicate a shift towards low FRET states when A_{2A}AR interacts with agonists and mini-G_S, both in SMALP and DIBMALP environments.

4.2 Introduction

Membrane scaffold protein (MSP) nanodiscs are a widely used technique in the structural and functional analysis of various membrane proteins, including G protein-coupled receptors (GPCRs). These MSP1D1-based nanodiscs provide a native-like phospholipid environment that mimics the hydrophobic conditions and lateral pressure found in natural membranes [171, 182]. However, the process of detergent solubilization poses significant challenges. During this procedure, membrane proteins may undergo

unfolding, aggregation, or loss of activity, as well as imbalance the membrane lateral pressure [64, 74, 82].

The functionality of GPCRs is closely related to specific lipid-protein interactions, such as the GPCRs' interactions with PIP_2 and cholesterol [58]. Unfortunately, these interactions are not preserved during the detergent mediated MSP1D1 nanodisc membrane stabilization process. Consequently, the detergent-free methods for purifying and stabilizing membrane proteins within their native membrane environment have been highlighted in recent years, especially in the study of GPCR functionality and structural dynamics. Compared to mammalian cell membrane components, MSP1D1 nanodiscs that we used in previous experiments lack cholesterol which plays a crucial role in interactions with certain cholesterol-binding domains in GPCRs [183]. Molecular dynamics (MD) simulations and crystallographic analyses of GPCRs have highlighted the presence of multiple cholesterol-binding motifs [70, 184, 185]. Additionally, the addition of cholesterol content has been shown to have significant functional consequences in GPCR signaling pathways [65, 67]. Specifically, membrane cholesterol depletion leads to a reduction in downstream signaling activities of the A_{2A}AR [69, 184]. All this evidence emphasizes the necessity of maintaining a native membrane environment in GPCR studies.

As a novel and efficient approach to solubilizing and purifying membrane proteins, detergent-free polymers such as polystyrene-co-maleic acid (SMA) and diisobutylene-maleic acid (DIBMA) can spontaneously insert into the lipid bilayer and extract membrane proteins along with their surrounding lipid environment, forming into nanodiscs (**Figure**

13) [82, 186-188]. The principle of this process is the amphiphilic nature of these co-polymers, which allows them to interact simultaneously with the hydrophobic lipid bilayers and water molecules. Consequently, this interaction leads to the formation of disc-shaped lipid particles (LPs). These polymer solubilization methods not only maintain the original structure, oligomerization, and function of membrane proteins but also preserve the protein-membrane interactions to the greatest possible [187, 189].

The SMALP approach offers advantages and simplifies the purification process for membrane proteins compared to traditional detergent-based methods. The GPCR-SMALP complex has already been utilized to study stability, functionality, kinetics, and structural dynamics within their native membrane environment. However, some potential limitations of SMA have also been noted in GPCR studies [82, 186, 190]. The primary drawback of SMA is its susceptibility to divalent cations, especially Mg^{2+} and Ca^{2+}, which can lead to conformational changes and precipitation of the SMA [77]. This principle of SMA to divalent cations causes a significant challenge in GPCR studies, especially in interactions with G proteins, as their binding with GPCRs relies on Mg^{2+} [80, 189]. Besides, during the activation of GPCR, the transmembrane helixes undergo significant structural rearrangement, resulting in a considerable volume change within the membrane, especially in the inner leaflet. However, the size limitations of SMALPs could restrict lipid freedom around GPCRs [80, 191]. Additionally, the hydrophobic styrene insertion may displace lipid molecules and slow down the conformational change process [186]. Considering these factors, we hypothesized that DIBMALP would provide a more reliable system for solubilizing and stabilizing the A_{2A}AR. Compared to SMA, DIBMA also exhibits

reduced sensitivity to divalent cations and provides milder fragmentation of the lipid bilayer, forming into discs with larger lipid surfaces, typically with a diameter around 10 to 50 nm [188, 192]. These features could provide less restriction during GPCR conformational change. Furthermore, DIBMALP can also capture the GPCRs with their ligand and G protein-bound form [77, 192].

To further understand the conformational dynamics of $A_{2A}AR$ on the intracellular side, our focus is on examining the conformational changes between two helices, TM IV and TM VI. Using a single molecule Fluorescence resonance energy transfer (smFRET) technique, we aimed to investigate the structural dynamics among different conformational states of APO, agonist-bound, and antagonist-bound $A_{2A}AR$, both with and without mini-G_S interaction.

4.3 Result

4.3.1 Expression of $A_{2A}AR$ from mammalian cells

To monitor the dynamics of intracellular helices of the $A_{2A}ARs$ in their native membrane environment, we designed the full-length $A_{2A}AR$ (1-412) with mutations introducing two maleimide dye labeling sites: one at the intracellular tip of TM IV (T119C) and the intracellular tip of TM VI (L225C). This design considers the activation process of Class A GPCRs, where the intracellular TM VI and TM VII undergo significant conformational changes, with TM VI notably moving away from the bundle (**Figure 22**) [193]. Additionally, the CWxp motif in TM VI and the NPxxY motif in TM VII contribute to G protein binding specificity [194]. Therefore, our focus is on the conformational dynamic pattern of TM VI, while the static helix, TM IV, serves as a reference substance helix. The

dynamic interplay between TM IV and TM VI can be elucidated through single-molecule Förster resonance energy transfer (smFRET) techniques (**Figure 22**). Although the wild-type A_{2A}AR contains a total of 15 inherent cysteines, eight of them are located within the transmembrane region [195, 196]. Meanwhile, six cysteines reside in the extracellular loops, forming three pairs of stable disulfide bonds, which avoid non-specific labeling with maleimide dyes [196]. The C394 located on the C-terminal has been identified as a crucial factor in the dimerization process of A_{2A}AR [197]. To avoid dimerization and non-specific labeling on C394, we introduced the Alanine mutation to C394. For protein purification and immobilization, our A_{2A}AR is expressed with a Flag tag on the N-terminal end and a 10X His tag on the C-terminal end (**Figure S12**). We cloned this A_{2A}AR sequence to the pcDNA3.1 vector (**Figure S12**) and successfully expressed this full-length mutant A_{2A}AR variant in the human embryonic kidney 293 (HEK293) cell lines (**Figure 23, Figure 24**).

4.3.2 Formation, labeling, and purification of co-polymer A_{2A}AR lipid complexes

After the A_{2A}AR was expressed in the cell line, we utilized 1.5% polymers (DIBMA or SMA) to solubilize the membrane proteins, followed by Ni-NTA nickel affinity chromatography purification of A_{2A}AR polymer LPs. The anti-His and anti-Flag tag western blot results confirmed the purification of the full-length A_{2A}AR captured by polymers, with a predominating monomeric form. As for the labeling, the eluted samples were incubated at 4 °C with maleimide fluorescent dyes, with Alexa-555 as the donor and Alexa-647 as the acceptor for 3 hours. Subsequently, the free dyes and imidazole in elution were removed from the sample by dialysis. Eventually, we obtained labeled A_{2A}AR polymer LPs. The molecular weights of purified A_{2A}AR-DIBMALPs and A_{2A}AR-SMALPs

samples were determined by the Mass Photometry (MP) analysis (**Figure 25**). The presence of single-peak populations in the MP data indicates that the majority of A_{2A}ARs solubilized by polymers are monomers. The average molecular weight of the purified A_{2A}AR-DIBMALPs was measured to be approximately 130 kilodaltons (kDa), while A_{2A}AR-SMALPs exhibited a smaller average molecular weight, around 99 kDa. Additionally, the MP histogram of A_{2A}AR-SMALPs showed a small shoulder on the peak, which indicates a more homogeneous size distribution of the A_{2A}AR in SMALP (**Figure 25**). On the other hand, we used Transmission Electron Microscopy (TEM) to visualize the formation structures and sizes of purified A_{2A}AR-SMALP and A_{2A}AR-DIBMALP complexes (**Figure 26**). Image J analysis revealed the size distribution of polymer LPs. The A_{2A}AR-SMALP exhibited a uniform size of around 23 nm. In addition, the A_{2A}AR-DIBMALP complex displayed a bigger average size of around 31 nm, except for some giant, irregularly shaped aggregates. These sizes align with the typical range observed for DIBMALP and SMA-purified membrane proteins [182, 198]. Altogether, these results indicate successful solubilization of the A_{2A}ARs by SMA and DIBMA in their native membrane environment, resulting in relatively uniform particle sizes. Moreover, the size of the A_{2A}AR-SMALP complex is notably smaller than that of the A2AAR-DIBMALP, indicating the limitations related to the size of SMALP on the conformational changes of the A_{2A}AR.

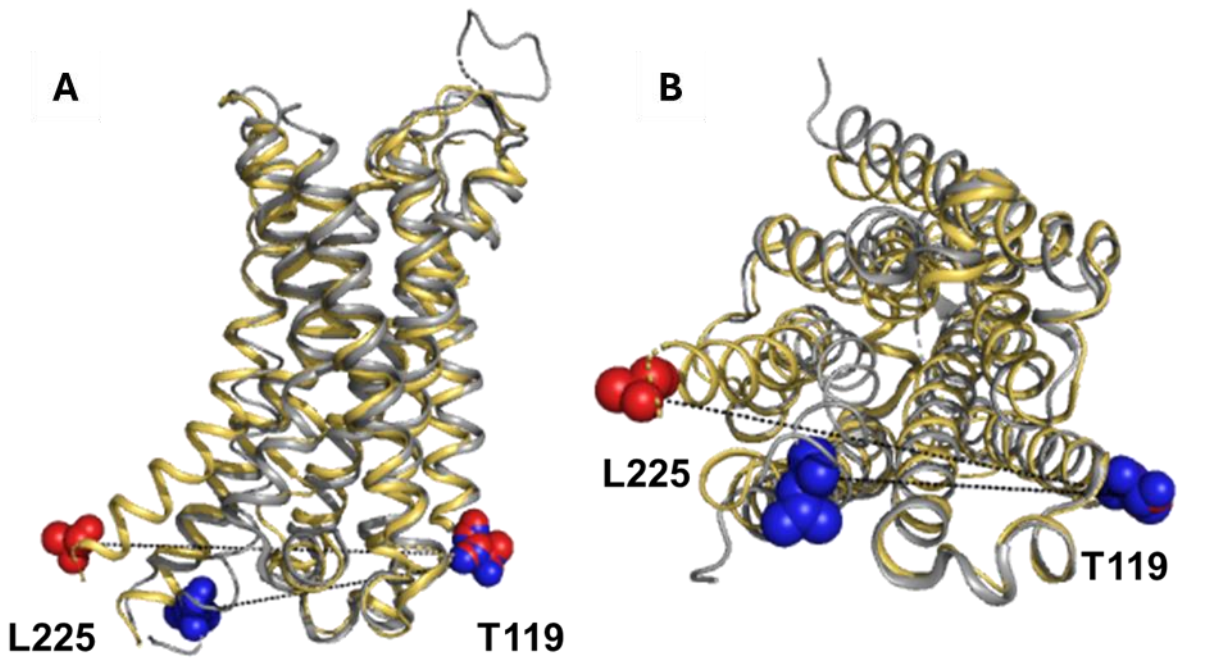

PDB ID	T119 (TM IV) – L225 (TM VI)
3eml (A_{2A}AR – ZM)	29.1 Å
6gdg (A_{2A}AR – NECA – Gs)	41.2 Å

Figure 22. A_{2A}AR conformational change between intracellular TM IV to TM VI.

(A) The front views show the overlay of A_{2A}AR in its fully active state (yellow with red T119 and L225, PDB 6gdg) and inactive state (gray with blue T119 and L225, PDB 3eml). (B) The bottom views of A_{2A}AR crystal structures. During A_{2A}AR activation, intracellular TM VII exhibits the most significant conformational changes, moving away from the bundle, while TM IV remains static. The distance between TM IV and TM VI increases from 29.1 Å to 41.2 Å.

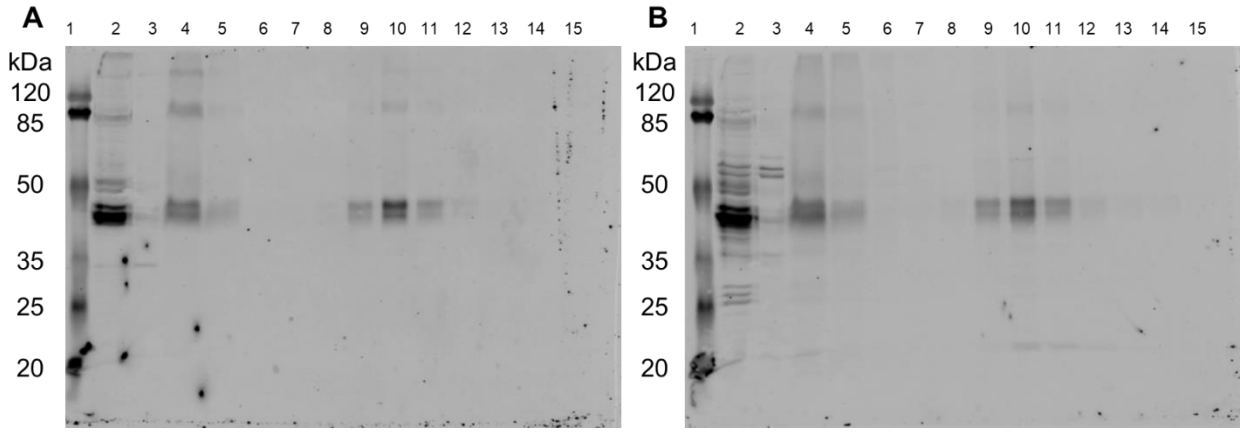

Figure 23. Western blot characterization of A_{2A}AR expression and A_{2A}AR-DIBMALPs purification.

The (A) anti-Flag tag and (B) anti-His tag western blot results reveal the majority of purified A_{2A}AR-DIBMALP forms as monomers, approximately 47 kDa in size.

Lane 1: Pre-stained protein molecular weight marker. Lane 2: Cell lysate of A_{2A}AR-expressing HEK293T cells. Lane 3: Supernatant of cell lysate. Lane 4: Membrane proteins solubilized by DIBMA. Lane 5: Flow-through after Ni-NTA incubation. Lanes 6-8: Washing buffer with 20 mM, 40 mM, 60 mM imidazole, respectively. Lanes 9-15: Elution 1 to elution 7 of affinity purification.

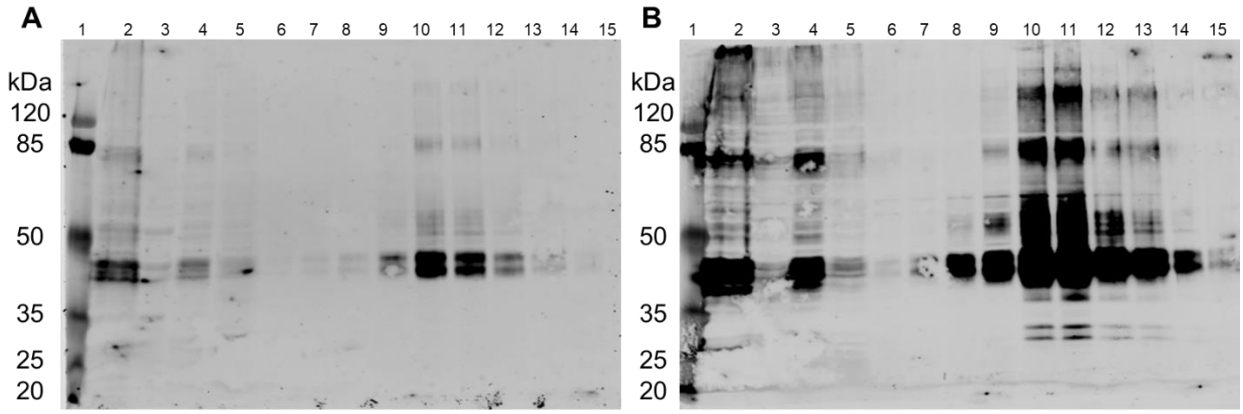

Figure 24. Western blot characterization of A_{2A}AR expression and A_{2A}AR-SMALPs purification.

The (A) anti-Flag tag and (B) anti-His tag western blot results reveal the expression of A_{2A}AR from HEK293T cell and the A_{2A}AR-SMALPs after the His tag affinity binding purification. The specificity of the anti-His tag antibody is lower compared to the anti-Flag tag antibody. Based on the western blot with the primary antibody of the anti-Flag tag, the majority of purified A_{2A}AR-SMALPs appear as monomers.

Lane 1: Pre-stained protein molecular weight marker. Lane 2: Cell lysate of A_{2A}AR-expressing HEK293T cells. Lane 3: Supernatant of cell lysate. Lane 4: Membrane proteins solubilized by DIBMA. Lane 5: Flow-through after Ni-NTA incubation. Lanes 6-8: Washing buffer with 20 mM, 40 mM, 60 mM imidazole, respectively. Lanes 9-15: Elution 1 to elution 7 of affinity purification.

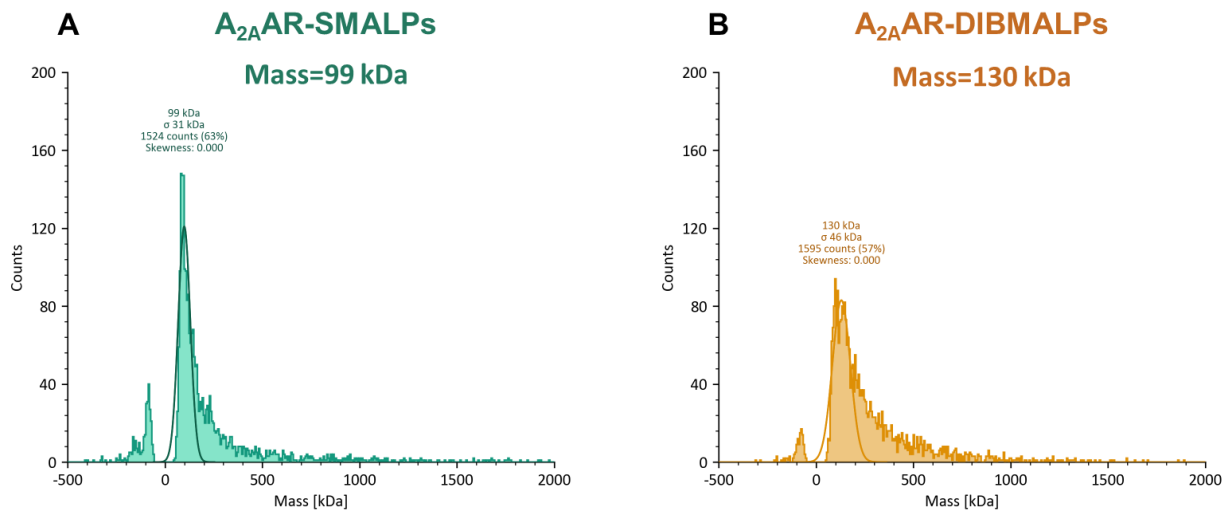

Figure 25. Mass photometry (MP) reveals the molecular weight of A_{2A}AR in polymer LPs.

Mass photometry measures the molecular weight of (A) A_{2A}AR-SMALPs and (B) A_{2A}AR-DIBMALPs. Both mass histograms display a predominant single population. Based on the fitting, the molecular weight of A_{2A}AR-SMALPs is approximately 99 kDa, and A_{2A}AR-DIBMALPs has an average molecular weight around 130 kDa.

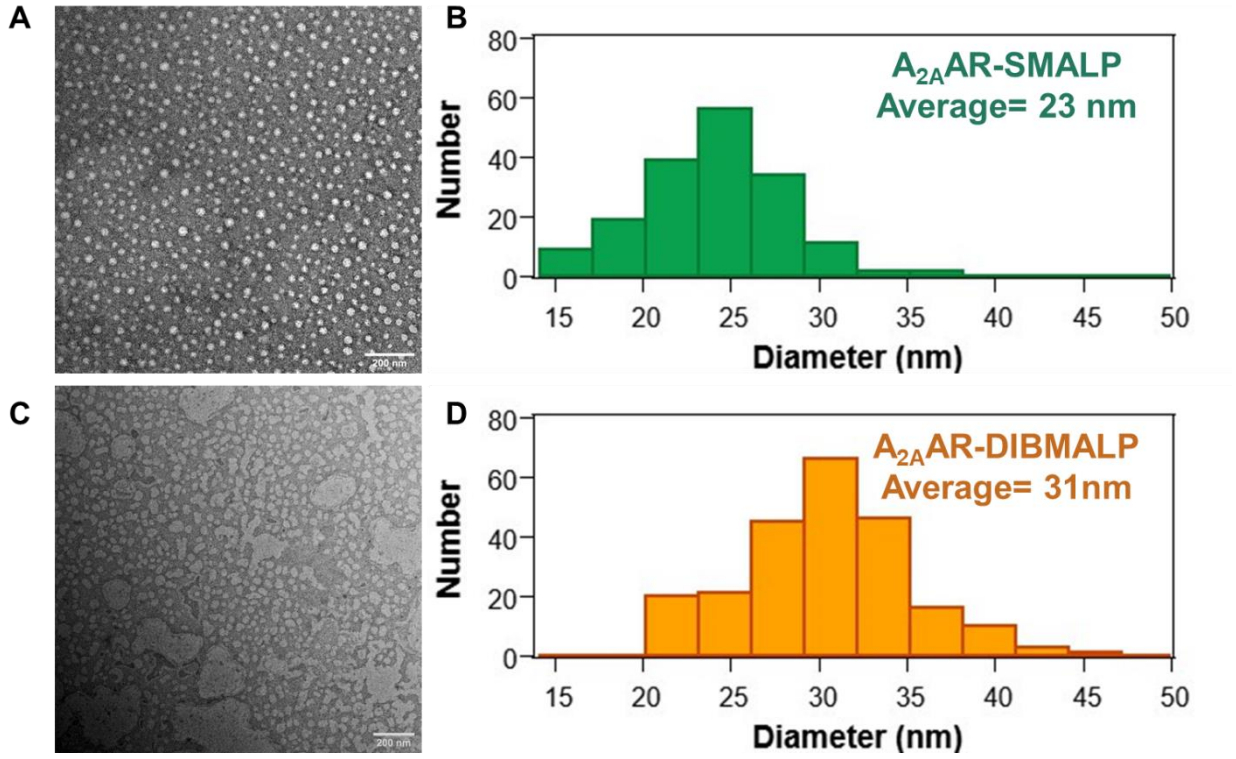

Figure 26. Transmission electron microscopy (TEM) reveals the disc size of A_{2A}AR polymer LPs.

(A) TEM image of uranyl acetate-stained A_{2A}AR-SMALPs. (B) Diameter distribution of A_{2A}AR-SMALPs, with an average diameter of around 23 nm. (C) TEM image of uranyl acetate-stained A_{2A}AR-DIBMALPs. (D) Diameter distribution of all regularly shaped A_{2A}AR-DIBMALPs, showing an average diameter of around 31 nm.

4.3.3 A_{2A}AR conformational dynamic in native membrane environment uncovered by smFRET

After purifying and labeling the A_{2A}AR within the polymer LPs, we applied the smFRET to monitor and analyze the conformational dynamics of A_{2A}ARs in their native membrane environment, primarily by employing DIBMA. The slide cleaning and PEGylation of the quartz slide followed our previous study [166, 199]. After that, the labeled A_{2A}AR-DIBMALP samples were immobilized on a quartz slide through streptavidin-biotin interactions, followed by biotinylated anti-Flag antibodies binding to the Flag tags on the N-terminal of A_{2A}AR in DIBMALPs (**Figure 27**). Although based on TEM results, most of the purified A_{2A}AR in polymer LPs are monomers, we still observed aggregates during single-molecule recording, which could be triggered by the properties of polymers, as reported in existing research [187, 198]. Moreover, in both the A_{2A}AR-SMALP and A_{2A}AR-DIBMALP samples, this aggregation was further exacerbated by incubation with the antagonist ZM or mini-G_S, especially in DIBMALP. This might be related to the stability of DIBMA in environmental conditions [77]. For molecule selection, we choose single molecule time traces displaying single step bleaching for both donor and acceptor signals, along with an anti-correlation in intensity between them. Our selection included both static and dynamic molecules. (**Figure S16**). The FRET efficiency (E) was calculated by equation $E = I_A/(I_D+I_A)$, where I_A represents the acceptor intensity, and I_D represents the donor intensity.

The hidden Markov model fitting was used on the selected dynamic FRET time traces to reveal the intensity of states and transition information between different

conformational states. However, as the data is still in its preliminary stage, determining the number of TM IV-TM VI conformational states during A_{2A}AR activation in DIBMALPs remains unclear. Although the state information needs to be explored further in the next step, the overall FRET population shifted to a lower efficiency state when binding with the agonist NECA. The addition of mini-G_S protein further reduced the FRET efficiency population to a lower efficiency state (Figure 28). This observation is consistent with the crystal structure in which the TM VI of A_{2A}AR moves outward during the activation process, increasing the distance between TM VI and TM IV [200]. At the same time, we also applied smFRET experiments to track the structural dynamics of A_{2A}AR in SMALP complexes. Although the FRET populations of A_{2A}AR molecules show a similar shift direction towards lower FRET efficiency when interacting with agonists and mini-G_S proteins, this shift is less significant compared to the DIBMALP samples (**Figure 28**). Besides, we observed a higher proportion of static A_{2A}AR molecules within the SMALP compared to those within the DIBMALP. These preliminary results suggest that SMALPs may limit the conformational flexibility of A_{2A}AR. Accordingly, we compiled transition events of A_{2A}AR-DIBMALP by using transition density plots. Although the preliminary results are unclear in revealing the exact number of conformational states, it is obvious that the interaction of the A_{2A}AR-DIBMALP with the agonist NECA and mini-G_S induces more transition events of low FRET, indicating an increasing percentage of transitions towards the active conformations.

4.4 Discussion

The innovation of this study breaks through the limitation of studying the molecular dynamics of A_{2A}AR in their native membrane environment, which maintains most of the lipid-protein interactions. Compared to our previous use of single environment sensitive Cy3 dyes to reveal dynamic information on TM VII, this study expands the understanding of conformational change between two different intracellular helixes.

The first and challenging step was to obtain high-quality, labeled A_{2A}AR within polymer LPs, which can be observed on a single molecular level. To reduce the aggregation and polymer precipitation during the purification and labeling processes, we avoided divalent cations or A_{2A}AR ligands until the single molecule TIRF imaging. The addition of 1% glycerol to all buffers helped decrease the aggregation level of both A_{2A}AR-SMALPs and A_{2A}AR-DIBMALPs to some extent. However, the TEM and TIRF imaging still exhibits some aggregates, particularly in DIBMALP (**Figures 25B, 26C**). Furthermore, the aggregates dramatically increased within a week after the freshly prepared sample.

Considering the negative charges carried by the maleic acid carboxylate groups in both SMA200 and DIBMA, which we utilized in our research, and considering the C-terminal of the A_{2A}AR protein that was involved in phosphorylation and was positively charged [201, 202], we presumed that these factors may intensify the aggregation of the particles. We attempted to reduce the aggregation level of DIBMLPs by using a C-terminal truncation mutant of A_{2A}AR (1-316). Based on the results of TEM and TIRF imaging, there was a slight reduction in the presence of giant aggregates under the APO condition in the

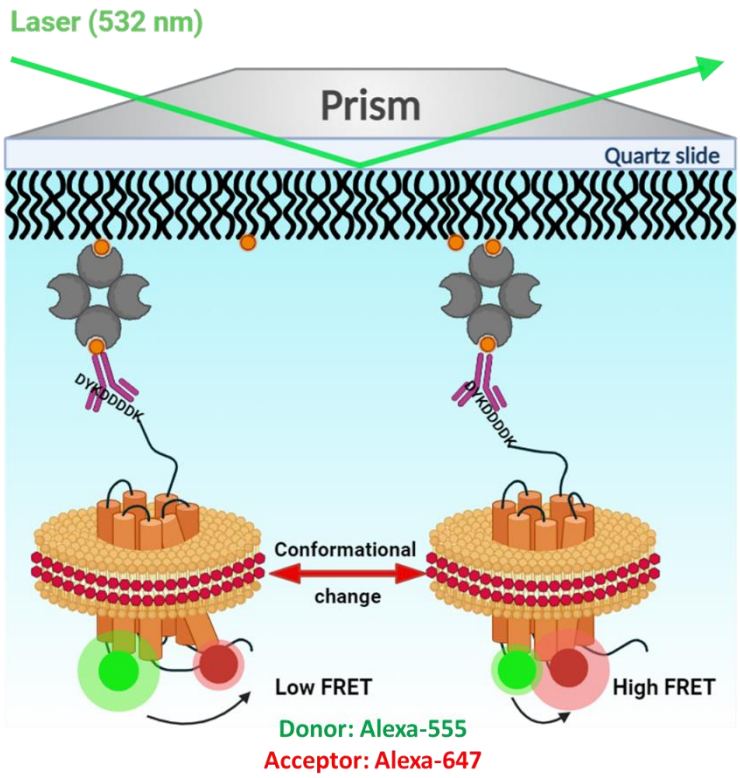

Figure 27. Schematic of using fluorescence resonance energy transfer to study the conformational dynamics of A_{2A}AR in the native membrane environment.

The schematic depicts Alexa-555 (green) and Alexa-647 (red) labeled A_{2A}AR (orange) within a polymer lipid particle (lipids shown in orange and polymer in red), immobilized onto a quartz slide by biotin (orange circles), streptavidin (gray semi-circles), and biotin-anti Flag antibody (orange circles with purple antibody). The Flag-tag is expressed on the N-terminal of A_{2A}AR immobilized on the slide. A 532 nm green laser is used to excite the donor fluorophore, Aleca-555 by creating an evanescent wave from the total internal reflection of the laser beam. The conformational change is monitored by the change in FRET efficiency.

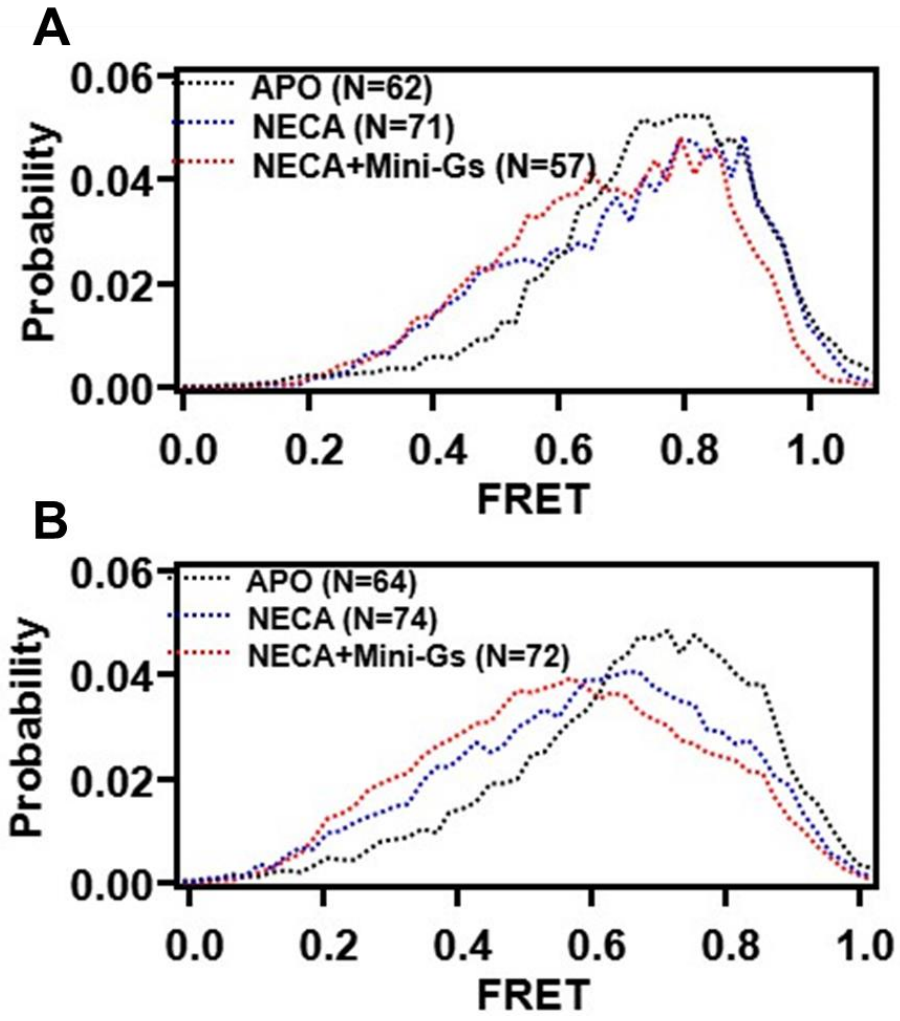

Figure 27. Histograms compiled from single molecule traces of A_{2A}AR in polymer LPs.

The FRET efficiency distribution of (A) A_{2A}AR-SMALPs and (B) A_{2A}AR-DIBMALPs reveals a population shift towards the low FRET population when A_{2A}AR interacts with the agonist NECA (blue dot), compared to the no ligand added APO conditions (black dot). The addition of mini-G_S (red dot) results in a further shift of the FRET population towards the lower FRET efficiency states.

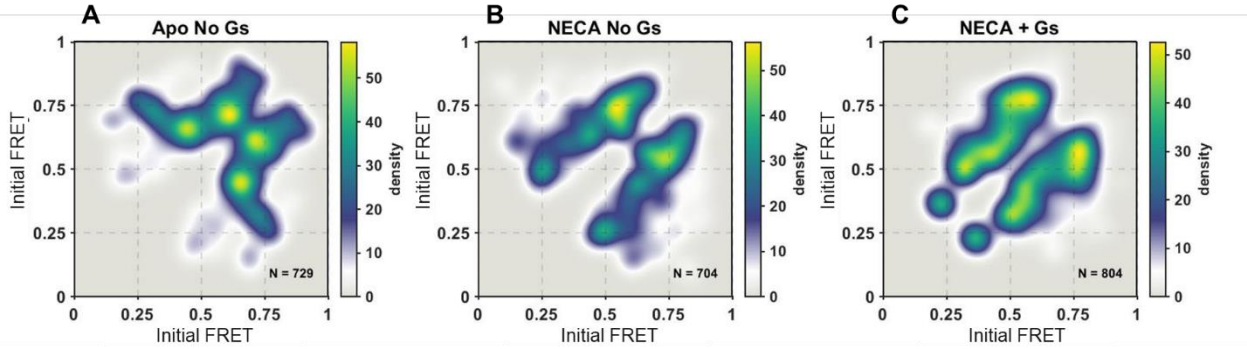

Figure 28. Transition density plots (TDPs) of A_{2A}AR-DIBMALPs.

TDPs exhibit the transition populations between different states of A_{2A}AR-DIBMALPs complexes under different conditions, including (A) without any binding partner, (B) with agonist NECA, and (C) with both agonist and mini-G_S.

C-terminal truncation version of A_{2A}AR-DIBMALPs (**Figure 26C and Figure S18A**). However, the aggregation induced by ZM still exists (**Figure S14**). On the other hand, aggregates were still clearly observed when mini-G_S protein was added to the environment (**Figure S14**). This phenomenon may be induced by the magnesium present in the mini-Gs incubation buffer, which is essential during the G protein activation [203]. In recent years, there has been a growing trend for membrane proteins purification by using various polymers [80, 192, 198]. Different types of DIBMAs with distinct properties have been gradually developed to meet evolving needs. Therefore, it is necessary to test multiple types of DIBMA, such as Glyco-DIBMA, which exhibits better solubility and higher tolerance of divalent cations [204], and Sulfo-DIBMA, capable of forming electroneutral nanodiscs [205]. We studied the single molecular dynamics of A_{2A}AR-SMALPs and A_{2A}AR-DIBMALPs under antagonist ZM, agonist NECA, and without ligand. Similar to the single-color experiment conducted previously in Chapter 3, we also introduced mini-G_S to the environment to investigate the impact of G protein interaction on the conformational dynamics of A_{2A}ARs in their native membrane environment.

The single-molecule FRET imaging of two dyes labeled A_{2A}AR-SMALPs and DIBMLPs, monitored using TIRF microscopy, confirmed the efficacy of conducting single-molecule level dynamic studies of A_{2A}ARs within their native membrane environment through polymer LPs stabilization. However, due to the requirement for high-quality labeled samples for single molecule experiments, the formation of aggregates influences the background signal and reduces the recording quality, particularly in conditions involving ZM and the addition of mini-G_S. The reason for the aggregation induced by the

antagonist ZM in A_{2A}AR-DIBMALPs remains unclear. In addition, we plan to investigate some other A_{2A}AR antagonists, such as caffeine and theophylline, to determine if they can maintain A_{2A}AR-DIBMALPs in a single molecule formation.

Due to the aggregation observed in the presence of ZM, only APO, NECA, and NECA with mini-G_S addition data were analyzed. The results from population distribution histograms suggest that the addition of the agonist and mini-G_S induced a shift in the conformation of TM VI towards lower FRET populations, indicating active-like states. Furthermore, we noted a reduced flexibility of A_{2A}AR TM VI in SMALPs compared to that in DIBMALPs, which suggests the advantage of studying the dynamic information of GPCR in larger discs, DIBMALPs. As for the dynamic analysis of FRET traces, we applied the same program we in our previous study, HaMMy [199]. However, despite the results of population distribution (**Figure 28**) and TDPs (**Figure 29**), the number of TM IV-TM VI conformational states during A_{2A}AR activation in DIBMALPs remained unclear. In the future, we will try another available software called vbFRET that uses variational Bayesian inference to learn hidden Markov models from individual, single-molecule FRET traces. This program can automatically fit the traces into the best number of states [206].

Besides advancing our molecular-level dynamic study of A_{2A}AR, we also need to verify the functionality of the A_{2A}AR mutants we designed for the dye labeling. We will assess the production level of cyclic guanosine monophosphate (cAMP), a secondary messenger involved in G protein activation, and compare it between the wild type and our A_{2A}AR mutants [207, 208]. Furthermore, we need to ensure that the A_{2A}AR stabilized in polymer LPs still maintains their functionality in ligand binding and G protein binding.

Therefore, ligand and mini-GS protein binding assays must be conducted as part of the further steps. Finally, we intend to repeat the smFRET experiment under all conditions of A_{2A}AR in DIBMALP and get detailed information on the A_{2A}AR TM VI dynamics.

4.5 Methods

4.5.1 Plasmid construction

The full-length A_{2A}AR [T119C L225C C394A] (**Figure S12**) and C-terminal truncation (1-316) A_{2A}AR [T119C L225C] plasmids used in this study were linked with N-terminal Flag tag followed with a three residues spacer (GSS) and C-terminal 10X His tag. The encoded genes were inserted into the high copy number pcDNA3.1(+) vector from HindIII and NotI restriction enzyme sites. The plasmids were prepared by a commercial vendor, in this case, GenScript (https://www.genscript.com). The plasmids were amplified by maxiprep, and their concentrations were measured by UV-Vis. Following plasmid amplification, polymerase chain reaction (PCR) amplification and sequencing were performed using three 5' primers to check the sequences (**Table S17**).

4.5.2 A_{2A}AR expression from HEK293T cell

We utilized the human embryonic kidney 293T cell line (HEK293T, ATCC) to express our designed A_{2A}ARs [209, 210]. The HEK293T cells were cultured in DMEM medium supplemented with 10% fetal bovine serum (FBS) and 1X antibiotic-antimycotic solution (Anti-Anti, 100 units/mL of penicillin, 100 µg/mL of streptomycin, Gibco). Before the DNA transfection, the cell line underwent at least six sub-culturing cycles, resulting in

six 100 mm cell culture dishes with 80% confluence in each dish. The cell line was grown in the incubator with humidification and 5% CO_2 at 37 °C.

After the cell was grown to six dishes, we prepared for the DNA transfection. First, we mixed the plasmid containing the designed A_{2A}AR insertion with polyethylenimine (PEI) as the transfection reagent, along with Opti-MEM medium. Our preliminary experiments revealed that the optimal transfection ratio between plasmid and PEI was 1:3. For each dish, 8μg of plasmid was sufficient for the protein expression, considering the high copy number of this plasmid. The transfection mix was incubated at room temperature in the dark for 30 minutes and then gently distributed equally into the six dishes. Subsequently, incubate the HEK293T cells in DMEM supplemented with 1X Anti-Anti and 5% FBS for 48 hours after the transfection to allow for A_{2A}AR expression.

4.5.3 HEK293T cell lysis and A_{2A}AR polymer LPs formation

After the protein expression, we removed the medium and washed cells with phosphate buffered saline (PBS) to clean the residual medium. Cells were detached and collected with a cell scraper from the culture dish. After collecting cells, they were centrifuged at 300 g for 10 minutes to remove the washing PBS. The cell pellet was then resuspended in 3mL lysis buffer consisting of 200 mM sodium chloride (NaCl), 25 mM N-2-hydroxyethylpiperazine-N'-2-ethanesulfonic acid (HEPES), 1% glycerol, and protease inhibitor at a pH of 7.5. As for the cell lysis, we used a 20-gauge needle connected to a 5 mL syringe to lyse the cells. Gently pass the cell up and down through the needle with the syringe, repeating 60 times. This process helps to break the cells and lyse the membrane into small pieces, facilitating the release of cell contents. Subsequently,

released DNAs that increased the viscosity of the lysate suspension were degraded by ultrasonication for 2 minutes at a power level of 1 on ice.

Before solubilizing the membrane proteins with polymer, we increased the efficiency by removing the nuclei through centrifugation at 500 x g for 5 minutes and discarding the pellet. The lysed membrane fractions were then centrifuged at 100,000 x g for an hour. The collected membrane pellets were mixed with DIBMALP/SMALP buffer containing 200 mM NaCl, 25 mM HEPES, and 1% glycerol, along with either 1.5% DIBMA or SMA polymers. The mixture was then incubated overnight at 4 °C with rotation to facilitate polymer solubilization of membrane proteins. Finally, the insolubilized components were spun down by ultracentrifugation at 100,000 x g for an hour, resulting in the capture of membrane proteins by polymer LPs, which were contained in the supernatant buffer.

4.5.4 Purification and labeling of A_{2A}AR polymer LPs

To purify our A_{2A}AR, which contained a C-terminal 10X His tag and was captured in polymer LPs, we applied Ni-NTA affinity chromatography. A 500 mL Ni-NTA resin was pre-equilibrated three times with DIBMALP/SMALP buffer, each time for 10-20 minutes, and then incubated with the solution containing polymer-solubilized membrane proteins for more than 4 hours at 4 °C with rotation. We load the mixture in the column. The washing buffer (150 mM NaCl, 25 mM HEPES, 1% glycerol), and washing buffer with gradually increased imidazole (20 mM, 40 mM, 60 mM) were used to remove most of the unbound and nonspecifically bound proteins. In the end, the elution buffer containing washing buffer and 200 mM imidazole was utilized to elute the A_{2A}AR sample from the

resin. We performed sample elution by applying 200 µL of elution buffer seven times to ensure all the A_{2A}AR samples were collected.

After purifying the A_{2A}AR polymer LPs, Western blots were used to reveal the elution that contained the A_{2A}AR samples. These elution samples were combined, and the A_{2A}AR polymer LPs were subsequently incubated with Alexa-555 and Alexa-647 in a ratio of 1:5:10 for 3 hours at 4 °C in the dark. After labeling, the free dyes and imidazole were removed by dialysis. A 4L of freshly prepared dialysis buffer, consisting of 75 mM NaCl, 25 mM HEPES, 1% glycerol, pH 7.5, was prepared and cooled down to 4°C. The 7000kDa dialysis kit was dipped in the dialysis buffer for 10 minutes before sample injection. Initially, the dialysis buffer was changed twice, each time with 1 L, and incubated at 4 °C for 2 hours. For the last step, 2 L of dialysis buffer was incubated overnight at 4 °C with stirring.

4.5.5 A_{2A}AR single molecular FRET experiment

After the overnight dialysis, we collected the samples and calculated their concentration and labeling ratio using a Nanodrop spectrophotometer. It's important to note that these concentration measurements are rough estimations due to the low concentration of our samples and the absorbance of SMALP in the UV spectrum (around 200 nm to 270 nm), which overlaps with the protein absorbance at 280 nm [211]. We diluted the sample to 1 nM and incubated it with saturated ligand for more than an hour. The A_{2A}AR-mini-GS formation followed the method in Chapter III, 3.5.6. All the buffers and oxygen scavenging systems in single-molecule experiment also follow Chapter III, the only difference for the buffers for A_{2A}AR in polymer LPs is the addition of 1% glycerol.

The slide cleaning and passivation followed our previous method described in 3.5.7. The immobilization of A_{2A}AR-DIBMALPs and A_{2A}AR-SMALPs slightly differed from the process we applied to MSP1D1 nanodiscs. After immobilizing streptavidin on the PEGylated quartz surface, a solution of 500 ng/mL biotinylated anti-Flag tag antibody was incubated in the sample chamber for 10 minutes. Following this, unbound antibodies were washed away with an imaging buffer, and our A_{2A}AR polymer LPs were applied into the chamber and incubated for 30 minutes Once sample immobilization was complete, the sample chamber was washed again with imaging buffer and then flushed with a glucose oxidase and catalase oxygen scavenging system. The imaging was performed using the TIRF microscopy system, following the detailed steps described in section 3.5.7.

4.5.6 Data analysis

We recorded signals from both donor and acceptor channels, Custom-built data acquisition and visualization programs written in IDL software (Harris Geospatial Solutions, Inc.) [165, 171]. During data analysis, single molecular trajectories exhibiting both donor and acceptor signals with anti-correlation intensities were selected, including static and dynamic FRET traces. Each trajectory showed only a single step bleaching event on both the donor and acceptor signal. The static and dynamic FRET traces were compiled to generate the histograms exhibiting the overall population shift.

Furthermore, due to the more dynamic signals and the more significant conformational population shifts in A_{2A}AR-DIBMAS when interacting with agonist and mini-GS, we selected all dynamic traces (**Figure S16, bottom**) and employed maximum-likelihood Hidden Markov model fitting to distinguish states exhibited in each trajectory

[120]. After identifying all conformational states in dynamic traces, transition density plots (TDPs), which reveal the transition frequency between different conformational states, were generated using a custom-written code in MATLAB, as explained in the previous section 3.5.8. TDPs are crucial for accurately revealing the number, FRET efficiency, sequence, and reversibility of conformational states of A_{2A}AR in their native membrane environment, further contributing to dwell time analysis. However, to obtain TDPs with clearer populations, more dynamic FRET data are required. This will be our focus in the next step in this project.

CHAPTER V. CONCLUSIONS

5.1 Conclusion

In Chapter II, our investigation reviewed the conformational dynamics of the intracellular TM VII of the A_{2A}AR when it interacts with different ligands [165]. We employed TIRF (Total Internal Reflection Fluorescence) based single molecule microscopy for this investigation. As a membrane protein, we stabilized A_{2A}AR in a native-like lipid environment by MSP1D1 nanodisc to ensure its stability. By monitoring the signal from the environment-sensitive Cy3 probe labeled on the intracellular TV VII, we were able to determine two distinct conformational intensity states in the absence of any ligand and the presence of antagonist ZM. These states were distinguished by their normalized intensities, with intensity around 1 representing the inactive state and intensity around 2 representing the intermediate state. Upon the addition of the agonist NECA, a third population around normalized intensity 3 was populated. This newly observed state was assigned as an active conformational state of the A_{2A}AR activation. From the TDP results, we revealed the transitions between these three distinct states were both reversible and sequential. This finding suggested that direct transitions between the inactive and active states were highly unlikely. Instead, the transition pathway appeared to involve sequential transitions through the intermediate state 2. In this study, data acquisition with the EMCCD camera was conducted with an integration time of 100 milliseconds (ms). Consequently, signal fluctuations could only be resolved on time scales equal to or slower than 100 milliseconds, which we considered as slow dynamics. As for the structural representations of the three distinguishable conformational states, MD simulations identified two distinct conformational states of A_{2A}AR-Cy3. However, these simulations

failed to capture the intermediate state observed in the single-molecule experiments, designated as conformational state 2. This discrepancy arises from the fact that the intermediate state of A_{2A}AR has not been revealed by crystallography, primarily due to the instability and transience of this conformational state.

Although we elucidated the conformational dynamic pattern when A_{2A}AR interacts with different ligands, further questions have emerged about sequential transitions and the origination of three states. In Chapter III, we investigated how the interaction with G-proteins and CAMs influenced the dynamic patterns of A_{2A}AR. To maintain the stability of the G protein, we utilized an engineered G_{α} subunit, mini-G_S, to mimic the full-length G protein [212]. Furthermore, we also introduced specific constitutively active or inactive mutations to understand their impact on the structural dynamics of A_{2A}AR TM VII. The results based on our single molecule TIRF experiment highlighted that for WT A_{2A}AR, the interaction of the mini-G_S in the presence of an agonist decreases the population of inactive states. Meanwhile, from the dwell time analysis, mini-GS binding to the A_{2A}AR shifted the equilibrium towards the intermediate state. On the other hand, our observations revealed that for the CAMs, an active-state population was consistently present even in the absence of agonist stimulation. This indicates that the CAMs tend to take the active conformation on TM VII, and they appear to be insensitive to various ligands or interactions with mini-G_S. Kinetically, CAMs were found to increase the frequency of transitions from the inactive to the intermediate state, whereas the D52N mutation exhibited an opposing dynamic pattern. Furthermore, neither these constitutive

mutations nor the addition of mini-G_S altered the reversible and sequential dynamic pattern on TM VII.

In Chapters II and III, our focus was on the conformational dynamics of A_{2A}AR TM VII by stabilized receptors in MSP1D1 nanodisc with a native-like lipid environment. In Chapter IV, our objective was to unveil the structural dynamics of A_{2A}AR between the TM IV and TM VI within the native membrane environment by utilizing single-molecule FRET. We successfully captured the A_{2A}ARs in their natural membrane environment using polymer LPs, SMALP, and DIBMALP. The characterization of purified A_{2A}ARs in polymer LPs by MP and TEM revealed that the SMALPs formed a uniform size of approximately 23 nm, and the DIBMALPs were around 31 nm, with some uneven aggregations. These avoidants clearly showed that although the A_{2A}AR-SMALPs have a better homogenized disc formation than the A_{2A}AR-DIBAMLPs, the latter has a bigger size that could advance the conformational studies between TM IV and TM VI. Sequentially, the preliminary data from single-molecule FRET analysis of A_{2A}AR-SMALPs showed a narrow range of FRET efficiency population shifts towards lower efficiency states when interacting with agonists and mini-G_S as compared to A_{2A}AR-DIBMALPs. This evidence confirms that DIBMALPs could serve as a better system for investigating the dynamic information of GPCRs within their native membrane environment, including the A_{2A}AR. Furthermore, the dynamic trajectories fitted and compiled in TDP suggest that transitions between different states are reversible. Moreover, more transition events were observed in various lower FRET states, which we considered active-like states.

In conclusion, this study explored the conformational dynamics of A_{2A}AR TM VII in interaction with various ligands and the mini-GS protein on the molecular level. We also revealed the impact of constitutively activating and inactivating mutations on the structural dynamic patterns and the kinetic transitions between different conformational states. Currently, we are moving on to the conformational dynamic study of A_{2A}ARs in their native membrane environment. We found that DIBMALP would be a more suitable way to study the structural dynamic information of A_{2A}AR. However, the aggregation issue needs to be resolved by testing different polymers. The preliminary single-molecule FRET data revealed that binding agonist, NECA, and mini-G_S increase the transition events between more active-like states.

5.2 Future direction

Our next steps involve a comprehensive examination of different types of polymers, especially Glyco-DIBMA and Sulfo-DIBMA, to figure out the best polymer LPs that could reduce the aggregation level during single-molecule experiments [204, 213]. Accordingly, we will replicate the smFRET experiments under different conditions, including APO, antagonist-bound, and agonist-bound states of the A_{2A}AR, with and without adding mini-Gs protein. This will allow us to precisely assess the influence of these ligands and the mini-Gs protein on A_{2A}AR dynamics. Subsequently, we will utilize the vbFRET program to analyze the FRET trajectories that will provide comprehensive insights into the dynamics of A_{2A}AR transmembrane helix VI (TM VI) [206]. In addition to advancing our molecular-level dynamic study of A_{2A}AR, we need to confirm the functionality of the A_{2A}AR mutants designed for dye labeling. Accordingly, we will conduct the cAMP assay to compare levels

of cAMP production between the wild type and our A_{2A}AR mutants [207]. Moreover, it is necessary to ensure that the A_{2A}AR stabilized in polymer LPs retain their functionality for the ligand binding and G protein interaction. Thus, ligand and mini-GS protein binding assays are necessary for the subsequent steps.

After we understand the dynamic behavior of A_{2A}AR in the native membrane environment, our investigation will extend to understanding the impact of cholesterol on A_{2A}AR conformational changes during activation within its native membrane environment. To achieve this, we will manipulate the cholesterol concentration in HEK293 cells using Methyl-β-cyclodextrin (MβCD) to deplete cholesterol. The cholesterol levels will be quantified using the Cholesterol Quantitation Kit (MAK043). We will employ single-molecule FRET to monitor the dynamics between TM IV and TM VI.

REFERENCES

1. Foord, S.M., et al., *International Union of Pharmacology. XLVI. G protein-coupled receptor list.* Pharmacol Rev, 2005. **57**(2): p. 279-88.
2. Davies, M.N., et al., *Proteomic applications of automated GPCR classification.* Proteomics, 2007. **7**(16): p. 2800-14.
3. Wong, T.S., et al., *G protein-coupled receptors in neurodegenerative diseases and psychiatric disorders.* Signal Transduct Target Ther, 2023. **8**(1): p. 177.
4. Dunham, J.H. and R.A. Hall, *Enhancement of the surface expression of G protein-coupled receptors.* Trends Biotechnol, 2009. **27**(9): p. 541-5.
5. Hanlon, C.D. and D.J. Andrew, *Outside-in signaling--a brief review of GPCR signaling with a focus on the Drosophila GPCR family.* J Cell Sci, 2015. **128**(19): p. 3533-42.
6. Congreve, M. and F. Marshall, *The impact of GPCR structures on pharmacology and structure-based drug design.* Br J Pharmacol, 2010. **159**(5): p. 986-96.
7. Basith, S., et al., *Exploring G Protein-Coupled Receptors (GPCRs) Ligand Space via Cheminformatics Approaches: Impact on Rational Drug Design.* Front Pharmacol, 2018. **9**: p. 128.
8. Birdsall, N.J., *Class A GPCR heterodimers: evidence from binding studies.* Trends Pharmacol Sci, 2010. **31**(11): p. 499-508.
9. Congreve, M., et al., *Impact of GPCR Structures on Drug Discovery.* Cell, 2020. **181**(1): p. 81-91.
10. Hollenstein, K., et al., *Insights into the structure of class B GPCRs.* Trends Pharmacol Sci, 2014. **35**(1): p. 12-22.

11. de Graaf, C., et al., *Extending the Structural View of Class B GPCRs.* Trends Biochem Sci, 2017. **42**(12): p. 946-960.

12. Parthier, C., et al., *Passing the baton in class B GPCRs: peptide hormone activation via helix induction?* Trends Biochem Sci, 2009. **34**(6): p. 303-10.

13. Wu, H., et al., *Structure of a class C GPCR metabotropic glutamate receptor 1 bound to an allosteric modulator.* Science, 2014. **344**(6179): p. 58-64.

14. Chun, L., W.H. Zhang, and J.F. Liu, *Structure and ligand recognition of class C GPCRs.* Acta Pharmacol Sin, 2012. **33**(3): p. 312-23.

15. Papasergi-Scott, M.M., et al., *Structures of metabotropic GABA(B) receptor.* Nature, 2020. **584**(7820): p. 310-314.

16. Turku, A., et al., *Residue 6.43 defines receptor function in class F GPCRs.* Nat Commun, 2021. **12**(1): p. 3919.

17. Bhat, R.A., et al., *Structure-function analysis of secreted frizzled-related protein-1 for its Wnt antagonist function.* J Cell Biochem, 2007. **102**(6): p. 1519-28.

18. Kozielewicz, P., A. Turku, and G. Schulte, *Molecular Pharmacology of Class F Receptor Activation.* Mol Pharmacol, 2020. **97**(2): p. 62-71.

19. Schulte, G. and P. Kozielewicz, *Structural insight into Class F receptors - What have we learnt regarding agonist-induced activation?* Basic Clin Pharmacol Toxicol, 2020. **126 Suppl 6**: p. 17-24.

20. Velazhahan, V., et al., *Structure of the class D GPCR Ste2 dimer coupled to two G proteins.* Nature, 2021. **589**(7840): p. 148-153.

21. Velazhahan, V., et al., *Activation mechanism of the class D fungal GPCR dimer Ste2.* Nature, 2022. **603**(7902): p. 743-748.

22. Greenhalgh, J.C., et al., *Proposed model of the Dictyostelium cAMP receptors bound to cAMP.* J Mol Graph Model, 2020. **100**: p. 107662.

23. Insel, P.A., et al., *G Protein-Coupled Receptor (GPCR) Expression in Native Cells: "Novel" endoGPCRs as Physiologic Regulators and Therapeutic Targets.* Mol Pharmacol, 2015. **88**(1): p. 181-7.

24. Vassilatis, D.K., et al., *The G protein-coupled receptor repertoires of human and mouse.* Proc Natl Acad Sci U S A, 2003. **100**(8): p. 4903-8.

25. Wingler, L.M. and R.J. Lefkowitz, *Conformational Basis of G Protein-Coupled Receptor Signaling Versatility.* Trends Cell Biol, 2020. **30**(9): p. 736-747.

26. Yang, D., et al., *G protein-coupled receptors: structure- and function-based drug discovery.* Signal Transduct Target Ther, 2021. **6**(1): p. 7.

27. Bunemann, M. and M.M. Hosey, *G-protein coupled receptor kinases as modulators of G-protein signalling.* J Physiol, 1999. **517 (Pt 1)**(Pt 1): p. 5-23.

28. Cheng, L., et al., *Structure, function and drug discovery of GPCR signaling.* Mol Biomed, 2023. **4**(1): p. 46.

29. Huang, Y., N. Todd, and A. Thathiah, *The role of GPCRs in neurodegenerative diseases: avenues for therapeutic intervention.* Curr Opin Pharmacol, 2017. **32**: p. 96-110.

30. Azam, S., et al., *G-Protein-Coupled Receptors in CNS: A Potential Therapeutic Target for Intervention in Neurodegenerative Disorders and Associated Cognitive Deficits.* Cells, 2020. **9**(2).

31. Tautermann, C.S., D. Seeliger, and J.M. Kriegl, *What can we learn from molecular dynamics simulations for GPCR drug design?* Comput Struct Biotechnol J, 2015. **13**: p. 111-21.

32. Casado, V. and V. Casado-Anguera, *What are the current trends in G protein-coupled receptor targeted drug discovery?* Expert Opin Drug Discov, 2023. **18**(8): p. 815-820.

33. Jobe, A. and R. Vijayan, *Orphan G protein-coupled receptors: the ongoing search for a home.* Front Pharmacol, 2024. **15**: p. 1349097.

34. Hasko, G., L. Antonioli, and B.N. Cronstein, *Adenosine metabolism, immunity and joint health.* Biochem Pharmacol, 2018. **151**: p. 307-313.

35. Carpenter, B. and G. Lebon, *Human Adenosine A(2A) Receptor: Molecular Mechanism of Ligand Binding and Activation.* Front Pharmacol, 2017. **8**: p. 898.

36. Sheth, S., et al., *Adenosine receptors: expression, function and regulation.* Int J Mol Sci, 2014. **15**(2): p. 2024-52.

37. Paoletta, S., et al., *Receptor-driven identification of novel human A(3) adenosine receptor antagonists as potential therapeutic agents.* Methods Enzymol, 2010. **485**: p. 225-44.

38. Green, A., *Adenosine receptor down-regulation and insulin resistance following prolonged incubation of adipocytes with an A1 adenosine receptor agonist.* J Biol Chem, 1987. **262**(32): p. 15702-7.

39. DeOliveira, C.C., et al., *Role of A(1) and A(2A) adenosine receptor agonists in adipose tissue inflammation induced by obesity in mice.* Eur J Pharmacol, 2017. **799**: p. 154-159.

40. Grillo, S.L., et al., *Adenosine receptor expression in the adult zebrafish retina.* Purinergic Signal, 2019. **15**(3): p. 327-342.

41. Stockwell, J., E. Jakova, and F.S. Cayabyab, *Adenosine A1 and A2A Receptors in the Brain: Current Research and Their Role in Neurodegeneration.* Molecules, 2017. **22**(4).

42. Al-Attraqchi, O.H.A., et al., *Adenosine A2A Receptor as a Potential Drug Target - Current Status and Future Perspectives.* Curr Pharm Des, 2019. **25**(25): p. 2716-2740.

43. de Lera Ruiz, M., Y.H. Lim, and J. Zheng, *Adenosine A2A receptor as a drug discovery target.* J Med Chem, 2014. **57**(9): p. 3623-50.

44. Chen, J.-F. and R.A. Cunha, *The belated US FDA approval of the adenosine A2A receptor antagonist istradefylline for treatment of Parkinson's disease.* Purinergic Signalling, 2020. **16**(2): p. 167-174.

45. Cummins, L. and M.E. Cates, *Istradefylline: A novel agent in the treatment of "off" episodes associated with levodopa/carbidopa use in Parkinson disease.* Ment Health Clin, 2022. **12**(1): p. 32-36.

46. Isaacson, S.H., S. Bette, and R. Pahwa, *Istradefylline for OFF Episodes in Parkinson's Disease: A US Perspective of Common Clinical Scenarios.* Degener Neurol Neuromuscul Dis, 2022. **12**: p. 97-109.

47. Latorraca, N.R., A.J. Venkatakrishnan, and R.O. Dror, *GPCR Dynamics: Structures in Motion.* Chem Rev, 2017. **117**(1): p. 139-155.

48. Jaakola, V.P., et al., *The 2.6 angstrom crystal structure of a human A2A adenosine receptor bound to an antagonist.* Science, 2008. **322**(5905): p. 1211-7.

49. Eddy, M.T., et al., *Allosteric Coupling of Drug Binding and Intracellular Signaling in the A2A Adenosine Receptor.* Cell, 2017: p. 1-26.

50. Jespers, W., et al., *Deciphering conformational selectivity in the A2A adenosine G protein-coupled receptor by free energy simulations.* PLoS Comput Biol, 2021. **17**(11): p. e1009152.

51. Susac, L., et al., *A(2A) adenosine receptor functional states characterized by (19)F-NMR.* Proc Natl Acad Sci U S A, 2018. **115**(50): p. 12733-12738.

52. Huang, S.K., et al., *Delineating the conformational landscape of the adenosine A2A receptor during G protein coupling.* Cell, 2021. **184**(7): p. 1884-1894.e14.

53. Do, H.N., et al., *Unique features of different classes of G-protein-coupled receptors revealed from sequence coevolutionary and structural analysis.* Proteins, 2022. **90**(2): p. 601-614.

54. Weis, W.I. and B.K. Kobilka, *The Molecular Basis of G Protein-Coupled Receptor Activation.* Annu Rev Biochem, 2018. **87**: p. 897-919.

55. Korkutata, M., L. Agrawal, and M. Lazarus, *Allosteric Modulation of Adenosine A(2A) Receptors as a New Therapeutic Avenue.* Int J Mol Sci, 2022. **23**(4).

56. Thakur, N., et al., *Anionic phospholipids control mechanisms of GPCR-G protein recognition.* Nature Communications, 2023. **14**(1): p. 794.

57. Cui, M., et al., *Crystal structure of a constitutive active mutant of adenosine A(2A) receptor.* IUCrJ, 2022. **9**(Pt 3): p. 333-341.

58. Song, W., et al., *State-dependent Lipid Interactions with the A2a Receptor Revealed by MD Simulations Using In Vivo-Mimetic Membranes.* Structure, 2019. **27**(2): p. 392-403 e3.

59. White, K.L., et al., *Structural Connection between Activation Microswitch and Allosteric Sodium Site in GPCR Signaling.* Structure, 2018. **26**(2): p. 259-269 e5.

60. Yoshida, K., et al., *Phospholipid Membrane Fluidity Alters Ligand Binding Activity of a G Protein-Coupled Receptor by Shifting the Conformational Equilibrium.* Biochemistry, 2019. **58**(6): p. 504-508.

61. Wootten, D., et al., *Mechanisms of signalling and biased agonism in G protein-coupled receptors.* Nat Rev Mol Cell Biol, 2018. **19**(10): p. 638-653.

62. Di Paolo, G. and T.W. Kim, *Linking lipids to Alzheimer's disease: cholesterol and beyond.* Nat Rev Neurosci, 2011. **12**(5): p. 284-96.

63. Fabiani, C. and S.S. Antollini, *Alzheimer's Disease as a Membrane Disorder: Spatial Cross-Talk Among Beta-Amyloid Peptides, Nicotinic Acetylcholine Receptors and Lipid Rafts.* Front Cell Neurosci, 2019. **13**: p. 309.

64. Schonenbach, N.S., et al., *Adenosine A2a receptors form distinct oligomers in protein detergent complexes.* FEBS Lett, 2016. **590**(18): p. 3295-306.

65. Rouviere, E., et al., *Identification of Two New Cholesterol Interaction Sites on the A(2A) Adenosine Receptor.* Biophys J, 2017. **113**(11): p. 2415-2424.

66. Bianchetti, G., et al., *Investigation of the Membrane Fluidity Regulation of Fatty Acid Intracellular Distribution by Fluorescence Lifetime Imaging of Novel Polarity Sensitive Fluorescent Derivatives.* Int J Mol Sci, 2021. **22**(6).

67. Yang, L. and E. Lyman, *Local Enrichment of Unsaturated Chains around the A(2A) Adenosine Receptor.* Biochemistry, 2019. **58**(39): p. 4096-4105.

68. Ray, A.P., et al., *Dual mechanisms of cholesterol-GPCR interactions that depend on membrane phospholipid composition.* Structure, 2023. **31**(7): p. 836-847 e6.

69. McGraw, C., et al., *Membrane cholesterol depletion reduces downstream signaling activity of the adenosine A(2A) receptor.* Biochim Biophys Acta Biomembr, 2019. **1861**(4): p. 760-767.

70. Jakubik, J. and E.E. El-Fakahany, *Allosteric Modulation of GPCRs of Class A by Cholesterol.* Int J Mol Sci, 2021. **22**(4).

71. Pantelopulos, G.A., C.B. Abraham, and J.E. Straub, *Cholesterol and Lipid Rafts in the Biogenesis of Amyloid-beta Protein and Alzheimer's Disease.* Annu Rev Biophys, 2024.

72. Feringa, F.M. and R. van der Kant, *Cholesterol and Alzheimer's Disease; From Risk Genes to Pathological Effects.* Front Aging Neurosci, 2021. **13**: p. 690372.

73. Denisov, I.G., et al., *Directed Self-Assembly of Monodisperse Phospholipid Bilayer Nanodiscs with Controlled Size.* Journal of the American Chemical Society, 2004. **126**(11): p. 3477-3487.

74. Naranjo, A.N., et al., *Impact of purification conditions and history on A2A adenosine receptor activity: The role of CHAPS and lipids.* Protein Expr Purif, 2016. **124**: p. 62-7.

75. Jones, A.J.Y., et al., *Structure and Dynamics of GPCRs in Lipid Membranes: Physical Principles and Experimental Approaches.* Molecules, 2020. **25**(20).

76. Hothersall, J.D., et al., *Releasing the technical 'shackles' on GPCR drug discovery: opportunities enabled by detergent-free polymer lipid particle (PoLiPa) purification.* Drug Discov Today, 2020.

77. Gulamhussein, A.A., et al., *A comparison of SMA (styrene maleic acid) and DIBMA (di-isobutylene maleic acid) for membrane protein purification.* Biochim Biophys Acta Biomembr, 2020. **1862**(7): p. 183281.

78. Simon, K.S., N.L. Pollock, and S.C. Lee, *Membrane protein nanoparticles: the shape of things to come.* Biochem Soc Trans, 2018. **46**(6): p. 1495-1504.

79. Wheatley, M., et al., *GPCR-styrene maleic acid lipid particles (GPCR-SMALPs): their nature and potential.* Biochem Soc Trans, 2016. **44**(2): p. 619-23.

80. Routledge, S.J., et al., *Ligand-induced conformational changes in a SMALP-encapsulated GPCR.* Biochim Biophys Acta Biomembr, 2020. **1862**(6): p. 183235.

81. Morrison, K.A., et al., *Membrane protein extraction and purification using styrene-maleic acid (SMA) copolymer: effect of variations in polymer structure.* Biochem J, 2016. **473**(23): p. 4349-4360.

82. Pollock, N.L., et al., *Structure and function of membrane proteins encapsulated in a polymer-bound lipid bilayer.* Biochim Biophys Acta Biomembr, 2018. **1860**(4): p. 809-817.

83. Hilger, D., M. Masureel, and B.K. Kobilka, *Structure and dynamics of GPCR signaling complexes.* Nat Struct Mol Biol, 2018. **25**(1): p. 4-12.

84. Jespers, W., et al., *X-Ray Crystallography and Free Energy Calculations Reveal the Binding Mechanism of A(2A) Adenosine Receptor Antagonists.* Angew Chem Int Ed Engl, 2020. **59**(38): p. 16536-16543.

85. Kudalkar, E.M., T.N. Davis, and C.L. Asbury, *Single-Molecule Total Internal Reflection Fluorescence Microscopy.* Cold Spring Harb Protoc, 2016. **2016**(5): p. pdb top077800.

86. Fish, K.N., *Total internal reflection fluorescence (TIRF) microscopy.* Curr Protoc Cytom, 2009. **Chapter 12**: p. Unit12 18.

87. Lamichhane, R., et al., *Single-molecule view of basal activity and activation mechanisms of the G protein-coupled receptor β2AR.* Proc Natl Acad Sci U S A, 2015. **112**(46): p. 14254-9.

88. Sohn, H.W., et al., *A method for analyzing protein-protein interactions in the plasma membrane of live B cells by fluorescence resonance energy transfer imaging as acquired by total internal reflection fluorescence microscopy.* Methods Mol Biol, 2010. **591**: p. 159-83.

89. Lamichhane, R., et al., *Single-molecule FRET of protein-nucleic acid and protein-protein complexes: surface passivation and immobilization.* Methods, 2010. **52**(2): p. 192-200.

90. Liu, T., et al., *Single-molecule analysis reveals that a glucagon-bound extracellular domain of the glucagon receptor is dynamic.* J Biol Chem, 2023. **299**(9): p. 105160.

91. Sušac, L., et al., *A2A adenosine receptor functional states characterized by 19F-NMR.* Proceedings of the National Academy of Sciences of the United States of America, 2018. **115**(50): p. 12733-12738.

92. Wagner, G., A. DeMarco, and K. Wüthrich, *Dynamics of the aromatic amino acid residues in the globular conformation of the basic pancreatic trypsin inhibitor (BPTI).* Biophysics of structure and mechanism, 1976. **2**(2): p. 139-158.

93. Wüthrich, K. and G. Wagner, *NMR investigations of the dynamics of the aromatic amino acid residues in the basic pancreatic trypsin inhibitor.* FEBS letters, 1975. **50**(2): p. 265-268.

94. Hauser, A.S., et al., *Trends in GPCR drug discovery: new agents, targets and indications.* Nature Reviews Drug Discovery, 2017. **16**(12): p. 829-842.

95. Shimada, I., et al., *GPCR drug discovery: integrating solution NMR data with crystal and cryo-EM structures.* Nat Rev Drug Discov, 2019. **18**(1): p. 59-82.

96. Bostock, M.J., A.S. Solt, and D. Nietlispach, *The role of NMR spectroscopy in mapping the conformational landscape of GPCRs.* Current opinion in structural biology, 2019. **57**: p. 145-156.

97. Chung, H.S., et al., *Single-molecule fluorescence experiments determine protein folding transition path times.* Science, 2012. **335**(6071): p. 981-984.

98. Schuler, B., E.A. Lipman, and W.A. Eaton, *Probing the free-energy surface for protein folding with single-molecule fluorescence spectroscopy.* Nature, 2002. **419**(6908): p. 743-747.

99. Kim, J.-Y. and H.S. Chung, *Disordered proteins follow diverse transition paths as they fold and bind to a partner.* Science, 2020. **368**(6496): p. 1253-1257.

100. Aviram, H.Y., et al., *Two states or not two states: Single-molecule folding studies of protein L.* J Chem Phys, 2018. **148**(12): p. 123303.

101. Eddy, M.T., B.T. Martin, and K. Wüthrich, *A2A Adenosine Receptor Partial Agonism Related to Structural Rearrangements in an Activation Microswitch.* Structure, 2021. **29**(2): p. 170-176.e3.

102. Eddy, M.T., et al., *Extrinsic Tryptophans as NMR Probes of Allosteric Coupling in Membrane Proteins: Application to the A2A Adenosine Receptor.* Journal of the American Chemical Society, 2018. **140**(26): p. 8228-8235.

103. Ye, L., et al., *Mechanistic insights into allosteric regulation of the A2A adenosine G protein-coupled receptor by physiological cations.* Nature Communications, 2018. **9**(1): p. 1372.

104. Ye, L., et al., *Activation of the A2A adenosine G-protein-coupled receptor by conformational selection.* Nature, 2016. **533**(7602): p. 265-8.

105. Clark, L.D., et al., *Ligand modulation of sidechain dynamics in a wild-type human GPCR.* Elife, 2017. **6**.

106. Lamichhane, R., et al., *Biased Signaling of the G-Protein-Coupled Receptor beta2AR Is Governed by Conformational Exchange Kinetics.* Structure, 2020. **28**(3): p. 371-377 e3.

107. Lamichhane, R., et al., *Single-molecule view of basal activity and activation mechanisms of the G protein-coupled receptor beta2AR.* Proc Natl Acad Sci U S A, 2015. **112**(46): p. 14254-9.

108. Gregorio, G.G., et al., *Single-molecule analysis of ligand efficacy in β2AR–G-protein activation.* Nature, 2017. **547**(7661): p. 68-73.

109. Fernandes, D.D., et al., *Ligand modulation of the conformational dynamics of the A2A adenosine receptor revealed by single-molecule fluorescence.* Scientific Reports, 2021. **11**(1): p. 5910-16.

110. Maslov, I., et al., *Sub-millisecond conformational dynamics of the A2A adenosine receptor revealed by single-molecule FRET.* bioRxiv, 2020: p. 2020.11.26.400184.

111. Leitz, A.J., et al., *Functional reconstitution of Beta2-adrenergic receptors utilizing self-assembling Nanodisc technology.* Biotechniques, 2006. **40**(5): p. 601-2, 604, 606, passim.

112. Rouck, J.E., et al., *Recent advances in nanodisc technology for membrane protein studies (2012-2017).* FEBS Lett, 2017. **591**(14): p. 2057-2088.

113. Hwang, H., H. Kim, and S. Myong, *Protein induced fluorescence enhancement as a single molecule assay with short distance sensitivity.* Proc Natl Acad Sci U S A, 2011. **108**(18): p. 7414-8.

114. Stennett, E.M., et al., *Demystifying PIFE: The Photophysics Behind the Protein-Induced Fluorescence Enhancement Phenomenon in Cy3.* J Phys Chem Lett, 2015. **6**(10): p. 1819-23.

115. Liu, W., et al., *Structural basis for allosteric regulation of GPCRs by sodium ions.* Science, 2012. **337**(6091): p. 232-236.

116. Lebon, G., et al., *Agonist-bound adenosine A2A receptor structures reveal common features of GPCR activation.* Nature, 2011. **474**(7352): p. 521-525.

117. Carpenter, B., et al., *Structure of the adenosine A2A receptor bound to an engineered G protein.* Nature, 2016. **536**(7614): p. 104-107.

118. Xu, F., et al., *Structure of an agonist-bound human A2A adenosine receptor.* Science, 2011. **332**(6027): p. 322-327.

119. Horst, R., et al., *β_2-adrenergic receptor activation by agonists studied with ^{19}F NMR spectroscopy.* Angewandte Chemie, 2013. **52**(41): p. 10762-10765.

120. McKinney, S.A., C. Joo, and T. Ha, *Analysis of single-molecule FRET trajectories using hidden Markov modeling.* Biophys J, 2006. **91**(5): p. 1941-51.

121. Liauw, B.W.-H., H.S. Afsari, and R. Vafabakhsh, *Conformational rearrangement during activation of a metabotropic glutamate receptor.* Nature chemical biology, 2021: p. 1-22.

122. Bayburt, T.H. and S.G. Sligar, *Membrane protein assembly into Nanodiscs.* FEBS letters, 2010. **584**(9): p. 1721-1727.

123. Hagn, F., M.L. Nasr, and G. Wagner, *Assembly of phospholipid nanodiscs of controlled size for structural studies of membrane proteins by NMR.* Nature Protocols, 2018. **13**(1): p. 79-98.

124. Stefanski, K.M., et al., *PIP2 promotes conformation-specific dimerization of the EphA2 membrane region.* Journal of Biological Chemistry, 2021. **296**: p. 100149.

125. Berezhna, S.Y., et al., *Single-molecule Förster resonance energy transfer reveals an innate fidelity checkpoint in DNA polymerase I.* Journal of the American Chemical Society, 2012. **134**(27): p. 11261-11268.

126. Gutiérrez-de-Terán, H., et al., *The role of a sodium ion binding site in the allosteric modulation of the A2A adenosine G protein-coupled receptor.* Structure, 2013. **21**(12): p. 2175-2185.

127. Schrodinger, LLC, *The PyMOL Molecular Graphics System, Version 1.8*. 2015.

128. Sastry, G.M., et al., *Protein and ligand preparation: parameters, protocols, and influence on virtual screening enrichments.* Journal of computer-aided molecular design, 2013. **27**(3): p. 221-234.

129. Schrödinger, L., *MacroModel*. 2021: New York, NY.

130. Esguerra, M., et al., *GPCR-ModSim: A comprehensive web based solution for modeling G-protein coupled receptors.* Nucleic Acids Research, 2016. **44**(W1): p. W455-62.

131. Hess, B., et al., *GROMACS 4: Algorithms for Highly Efficient, Load-Balanced, and Scalable Molecular Simulation.* Journal of chemical theory and computation, 2008. **4**(3): p. 435-447.

132. Robertson, M.J., J. Tirado-Rives, and W.L. Jorgensen, *Improved Peptide and Protein Torsional Energetics with the OPLSAA Force Field.* Journal of chemical theory and computation, 2015. **11**(7): p. 3499-3509.

133. Berger, O., O. Edholm, and F. Jähnig, *Molecular dynamics simulations of a fluid bilayer of dipalmitoylphosphatidylcholine at full hydration, constant pressure, and constant temperature.* Biophysical journal, 1997. **72**(5): p. 2002-2013.

134. Chakrabarti, N., et al., *An Iris-Like Mechanism of Pore Dilation in the CorA Magnesium Transport System.* Biophysj, 2010. **98**(5): p. 784-792.

135. Berendsen, H.J., et al., *Interaction models for water in relation to protein hydration*, in *Intermolecular forces*. 1981, Springer. p. 331-342.

136. Dodda, L.S., et al., *LigParGen web server: an automatic OPLS-AA parameter generator for organic ligands.* Nucleic Acids Research, 2017. **45**(W1): p. W331-W336.

137. Hoover, W., *Canonical dynamics: Equilibrium phase-space distributions.* Physical review. A, General physics, 1985. **31**(3): p. 1695-1697.

138. Nosé, S., *A unified formulation of the constant temperature molecular dynamics methods.* Journal of Chemical Physics, 1984. **81**(1): p. 511-519.

139. Hess, B., et al., *LINCS: A linear constraint solver for molecular simulations.* Journal of Computational Chemistry, 1997. **18**(12): p. 1463-1472.

140. McGibbon, R.T., et al., *MDTraj: A Modern Open Library for the Analysis of Molecular Dynamics Trajectories.* Biophysj, 2015. **109**(8): p. 1528-1532.

141. Pauszek III, R.F., et al., *Single-molecule view of coordination in a multi-functional DNA polymerase.* Elife, 2021. **10**: p. e62046.

142. Cheng, Y.-C. and W.H. Prusoff, *Relationship between the inhibition constant (Ki) and the concentration of inhibitor which causes 50 per cent inhibition (I50) of an enzymatic reaction.* Biochemical Pharmacology, 1973. **22**(23): p. 3099-3108.

143. Yao, X.J., et al., *The effect of ligand efficacy on the formation and stability of a GPCR-G protein complex.* Proceedings of the National Academy of Sciences, 2009. **106**(23): p. 9501-9506.

144. Mahoney, J.P. and R.K. Sunahara, *Mechanistic insights into GPCR–G protein interactions.* Current Opinion in Structural Biology, 2016. **41**: p. 247-254.

145. Parnot, C., et al., *Lessons from constitutively active mutants of G protein-coupled receptors.* Trends in Endocrinology & Metabolism, 2002. **13**(8): p. 336-343.

146. Bond, R.A. and A.P. IJzerman, *Recent developments in constitutive receptor activity and inverse agonism, and their potential for GPCR drug discovery.* Trends in Pharmacological Sciences, 2006. **27**(2): p. 92-96.

147. Tehan, B.G., et al., *Unifying Family A GPCR Theories of Activation.* Pharmacology & Therapeutics, 2014. **143**(1): p. 51-60.

148. Parma, J., et al., *Somatic mutations in the thyrotropin receptor gene cause hyperfunctioning thyroid adenomas.* 1993. **365**.

149. Schipani, E., K. Kruse, and H. Jüppner, *A constitutively active mutant PTH-PTHrP receptor in Jansen-type metaphyseal chondrodysplasia.* Science, 1995. **268**(5207): p. 98-100.

150. Allen, L.F., et al., *G-protein-coupled receptor genes as protooncogenes: constitutively activating mutation of the alpha 1B-adrenergic receptor enhances mitogenesis and tumorigenicity.* Proceedings of the National Academy of Sciences, 1991. **88**(24): p. 11354-11358.

151. Atwood, Scott X., et al., *Smoothened Variants Explain the Majority of Drug Resistance in Basal Cell Carcinoma.* Cancer Cell, 2015. **27**(3): p. 342-353.

152. Arvanitakis, L., et al., *Human herpesvirus KSHV encodes a constitutively active G-protein-coupled receptor linked to cell proliferation.* Nature, 1997. **385**(6614): p. 347-350.

153. Paulsen, S.J., et al., *Epstein-Barr Virus-Encoded BILF1 Is a Constitutively Active G Protein-Coupled Receptor.* Journal of Virology, 2005. **79**(1): p. 536-546.

154. Standfuss, J., et al., *The structural basis of agonist-induced activation in constitutively active rhodopsin.* Nature, 2011. **471**(7340): p. 656-660.

155. Krumm, B.E., et al., *Structure and dynamics of a constitutively active neurotensin receptor.* Scientific Reports, 2016. **6**(1): p. 38564.

156. Cui, M., et al., *Crystal structure of a constitutive active mutant of adenosine A $_{2A}$ receptor.* IUCrJ, 2022. **9**(3): p. 333-341.

157. Jenner, P., et al., *Istradefylline – a first generation adenosine A2A antagonist for the treatment of Parkinson's disease.* Expert Review of Neurotherapeutics, 2021. **21**(3): p. 317-333.

158. Zheng, J., X. Zhang, and X. Zhen, *Development of Adenosine A $_{2A}$ Receptor Antagonists for the Treatment of Parkinson's Disease: A Recent Update and Challenge.* ACS Chemical Neuroscience, 2019. **10**(2): p. 783-791.

159. Yu, F., et al., *Adenosine A $_{2A}$ Receptor Antagonists for Cancer Immunotherapy: Miniperspective.* Journal of Medicinal Chemistry, 2020. **63**(21): p. 12196-12212.

160. Hatfield, S.M. and M. Sitkovsky, *A2A adenosine receptor antagonists to weaken the hypoxia-HIF-1α driven immunosuppression and improve immunotherapies of cancer.* Current Opinion in Pharmacology, 2016. **29**: p. 90-96.

161. Gessi, S., et al., *Adenosine receptors and cancer.* Biochimica et Biophysica Acta (BBA) - Biomembranes, 2011. **1808**(5): p. 1400-1412.

162. Mizumura, T., et al., *Activation of adenosine A_{2A} receptor by lipids from docosahexaenoic acid revealed by NMR.* Science Advances, 2020. **6**(12): p. eaay8544.

163. Sušac, L., et al., *A2A adenosine receptor functional states characterized by 19F-NMR.* Proceedings of the National Academy of Sciences, 2018. **115**(50): p. 12733-12738.

164. Ferré, G., et al., *Global insights into the fine tuning of human A2AAR conformational dynamics in a ternary complex with an engineered G protein viewed by NMR.* Cell Reports, 2022. **41**(12): p. 111844.

165. Wei, S., et al., *Slow conformational dynamics of the human A2A adenosine receptor are temporally ordered.* Structure, 2022. **30**(3): p. 329-337.e5.

166. Lamichhane, R., et al., *Biased Signaling of the G-Protein-Coupled Receptor β2AR Is Governed by Conformational Exchange Kinetics.* Structure, 2020. **28**(3): p. 371-377 e3.

167. Maslov, I., et al., *Sub-millisecond conformational dynamics of the A2A adenosine receptor revealed by single-molecule FRET.* Communications Biology, 2023. **6**(1): p. 362.

168. Jaakola, V.-P., et al., *The 2.6 Angstrom Crystal Structure of a Human A $_{2A}$ Adenosine Receptor Bound to an Antagonist.* Science, 2008. **322**(5905): p. 1211-1217.

169. Zhou, Q., et al., *Common activation mechanism of class A GPCRs.* eLife, 2019. **8**: p. e50279.

170. White, K.L., et al., *Structural connection between activation microswitch and allosteric sodium site in GPCR signaling.* Structure, 2018. **26**(2): p. 259-269.

171. Thakur, N., et al., *Production of human A_{2A}AR in lipid nanodiscs for 19F-NMR and single-molecule fluorescence spectroscopy.* STAR Protocols, 2022. **3**(3): p. 101535.

172. Jacobson, K.A., et al., *Adenosine A(2A) receptor antagonists: from caffeine to selective non-xanthines.* Br J Pharmacol, 2022. **179**(14): p. 3496-3511.

173. Massink, A., et al., *Sodium ion binding pocket mutations and adenosine A2A receptor function.* Mol Pharmacol, 2015. **87**(2): p. 305-13.

174. Katritch, V., et al., *Allosteric sodium in class A GPCR signaling.* Trends Biochem Sci, 2014. **39**(5): p. 233-44.

175. Zhang, M., et al., *Cryo-EM structure of an activated GPCR-G protein complex in lipid nanodiscs.* Nat Struct Mol Biol, 2021. **28**(3): p. 258-267.

176. Westfield, G.H., et al., *Structural flexibility of the G alpha s alpha-helical domain in the beta2-adrenoceptor Gs complex.* Proc Natl Acad Sci U S A, 2011. **108**(38): p. 16086-91.

177. Vafabakhsh, R., J. Levitz, and E.Y. Isacoff, *Conformational dynamics of a class C G-protein-coupled receptor.* Nature, 2015. **524**(7566): p. 497-501.

178. Hagn, F., et al., *Optimized Phospholipid Bilayer Nanodiscs Facilitate High-Resolution Structure Determination of Membrane Proteins.* Journal of the American Chemical Society, 2013. **135**(5): p. 1919-1925.

179. Carpenter, B. and C.G. Tate, *Engineering a minimal G protein to facilitate crystallisation of G protein-coupled receptors in their active conformation.* Protein Engineering Design and Selection, 2016. **29**(12): p. 583-594.

180. Freedman, D. and P. Diaconis, *On the histogram as a density estimator: L2 theory.* Zeitschrift für Wahrscheinlichkeitstheorie und Verwandte Gebiete, 1981. **57**(4): p. 453-476.

181. Sillen, A. and Y. Engelborghs, *The Correct Use of "Average" Fluorescence Parameters.* Photochemistry and Photobiology, 1998. **67**(5): p. 475-486.

182. Lavington, S. and A. Watts, *Lipid nanoparticle technologies for the study of G protein-coupled receptors in lipid environments.* Biophys Rev, 2020. **12**(6): p. 1287-302.

183. Taghon, G.J., et al., *Predictable cholesterol binding sites in GPCRs lack consensus motifs.* Structure, 2021. **29**(5): p. 499-506 e3.

184. McGraw, C., et al., *Cholesterol Dependent Activity of the Adenosine A(2A) Receptor Is Modulated via the Cholesterol Consensus Motif.* Molecules, 2022. **27**(11).

185. Yao, Z. and B. Kobilka, *Using synthetic lipids to stabilize purified beta2 adrenoceptor in detergent micelles.* Anal Biochem, 2005. **343**(2): p. 344-6.

186. Szundi, I., et al., *Styrene-maleic acid copolymer effects on the function of the GPCR rhodopsin in lipid nanoparticles.* Biophys J, 2021. **120**(20): p. 4337-4348.

187. Orekhov, P.S., et al., *Mechanisms of Formation, Structure, and Dynamics of Lipoprotein Discs Stabilized by Amphiphilic Copolymers: A Comprehensive Review.* Nanomaterials (Basel), 2022. **12**(3).

188. Oluwole, A.O., et al., *Solubilization of Membrane Proteins into Functional Lipid-Bilayer Nanodiscs Using a Diisobutylene/Maleic Acid Copolymer.* Angew Chem Int Ed Engl, 2017. **56**(7): p. 1919-1924.

189. Hawkins, O.P., et al., *Membrane protein extraction and purification using partially-esterified SMA polymers.* Biochim Biophys Acta Biomembr, 2021. **1863**(12): p. 183758.

190. Tedesco, D., et al., *Application of the SMALP technology to the isolation of GPCRs from low-yielding cell lines.* Biochim Biophys Acta Biomembr, 2021. **1863**(9): p. 183641.

191. Ayub, H., et al., *GPCRs in the round: SMA-like copolymers and SMALPs as a platform for investigating GPCRs.* Arch Biochem Biophys, 2024. **754**: p. 109946.

192. Voskoboynikova, N., et al., *Evaluation of DIBMA nanoparticles of variable size and anionic lipid content as tools for the structural and functional study of membrane proteins.* Biochim Biophys Acta Biomembr, 2021. **1863**(6): p. 183588.

193. Hoffmann, C., et al., *Conformational changes in G-protein-coupled receptors-the quest for functionally selective conformations is open.* Br J Pharmacol, 2008. **153 Suppl 1**(Suppl 1): p. S358-66.

194. Jastrzebska, B., *GPCR: G protein complexes--the fundamental signaling assembly.* Amino Acids, 2013. **45**(6): p. 1303-14.

195. De Filippo, E., et al., *Role of extracellular cysteine residues in the adenosine A2A receptor.* Purinergic Signal, 2016. **12**(2): p. 313-29.

196. Naranjo, A.N., et al., *Conserved disulfide bond is not essential for the adenosine A2A receptor: Extracellular cysteines influence receptor distribution within the cell and ligand-binding recognition.* Biochim Biophys Acta, 2015. **1848**(2): p. 603-14.

197. Nguyen, K.D.Q., et al., *Homo-oligomerization of the human adenosine A(2A) receptor is driven by the intrinsically disordered C-terminus.* Elife, 2021. **10**.

198. Voskoboynikova, N., et al., *Lipid Dynamics in Diisobutylene-Maleic Acid (DIBMA) Lipid Particles in Presence of Sensory Rhodopsin II.* Int J Mol Sci, 2021. **22**(5).

199. Wei, S., et al., *Slow conformational dynamics of the human A(2A) adenosine receptor are temporally ordered.* Structure, 2022. **30**(3): p. 329-337 e5.

200. Dore, A.S., et al., *Structure of the adenosine A(2A) receptor in complex with ZM241385 and the xanthines XAC and caffeine.* Structure, 2011. **19**(9): p. 1283-93.

201. Piirainen, H., et al., *Human adenosine A2A receptor binds calmodulin with high affinity in a calcium-dependent manner.* Biophys J, 2015. **108**(4): p. 903-917.

202. Borroto-Escuela, D.O., et al., *The coming together of allosteric and phosphorylation mechanisms in the molecular integration of A2A heteroreceptor complexes in the dorsal and ventral striatal-pallidal GABA neurons.* Pharmacol Rep, 2021. **73**(4): p. 1096-1108.

203. Birnbaumer, L. and A.R. Zurita, *On the roles of Mg in the activation of G proteins.* J Recept Signal Transduct Res, 2010. **30**(6): p. 372-5.

204. Danielczak, B., et al., *A bioinspired glycopolymer for capturing membrane proteins in native-like lipid-bilayer nanodiscs.* Nanoscale, 2022. **14**(5): p. 1855-1867.

205. Glueck, D., et al., *Electroneutral Polymer Nanodiscs Enable Interference-Free Probing of Membrane Proteins in a Lipid-Bilayer Environment.* Small, 2022. **18**(47): p. e2202492.

206. Bronson, J.E., et al., *Learning rates and states from biophysical time series: a Bayesian approach to model selection and single-molecule FRET data.* Biophys J, 2009. **97**(12): p. 3196-205.

207. Wright, P.T., S. Schobesberger, and J. Gorelik, *Studying GPCR/cAMP pharmacology from the perspective of cellular structure.* Front Pharmacol, 2015. **6**: p. 148.

208. Sassone-Corsi, P., *The cyclic AMP pathway.* Cold Spring Harb Perspect Biol, 2012. **4**(12).

209. Goulding, J., L.T. May, and S.J. Hill, *Characterisation of endogenous A(2A) and A(2B) receptor-mediated cyclic AMP responses in HEK 293 cells using the*

GloSensor biosensor: Evidence for an allosteric mechanism of action for the A(2B)-selective antagonist PSB 603. Biochem Pharmacol, 2018. **147**: p. 55-66.

210. Chen, G. and D. Obal, *Detecting and measuring of GPCR signaling - comparison of human induced pluripotent stem cells and immortal cell lines.* Front Endocrinol (Lausanne), 2023. **14**: p. 1179600.

211. Hesketh, S.J., et al., *Styrene maleic-acid lipid particles (SMALPs) into detergent or amphipols: An exchange protocol for membrane protein characterisation.* Biochim Biophys Acta Biomembr, 2020. **1862**(5): p. 183192.

212. Wei, S., et al., *Single-molecule visualization of human A(2A) adenosine receptor activation by a G protein and constitutively activating mutations.* Commun Biol, 2023. **6**(1): p. 1218.

213. Eggenreich, L., et al., *Lipid exchange among electroneutral Sulfo-DIBMA nanodiscs is independent of ion concentration.* Biol Chem, 2023. **404**(7): p. 703-713.

APPENDIX

Appendix I

A version of this appendix was originally published by Shushu Wei, Naveen Thakur, Arka P Ray, Beining Jin, Samuel Obeng, Christopher R McCurdy, Lance R McMahon, Hugo Gutiérrez-de-Terán, Matthew T Eddy, Rajan Lamichhane on Structure in November 2021. (Website: https://www.cell.com/structure/fulltext/S0969-2126(21)004172?_returnURL=https%3A%2F%2Flinkinghub.elsevier.com%2Fretrieve%2Fpii%2FS0969212621004172%3Fshowall%3Dtrue)

For this study, Shushu Wei implemented and supervised the project, conducted single-molecule experiments, collected and analyzed data, and wrote and edited the manuscript. Naveen Thakur and Arka P Ray conducted A_{2A}AR expression, labeling, and purification. Samuel Obeng, Christopher R. McCurdy, and Lance R. McMahon conducted radioligand binding experiments. Hugo Gutiérrez-de-Terán performed simulations. Rajan Lamichhane and Matthew T. Eddy acquired funding, supervised experiments and data analysis, and contributed to writing the manuscript with input from all co-authors.

Figure S1. Related to Figure 9. Sample preparation characterization and pharmacological validation of A_{2A}AR[A289C]-Cy3 in lipid nanodiscs.

(A) Representative analytical size exclusion chromatogram of A_{2A}AR-Cy3 in lipid nanodiscs shows a single homogenous preparation.

(B) Image of a representative SDS-PAGE characterization of A_{2A}AR preparations. The lane labeled “MWS” contains a standard molecular weight ladder with three different molecular weights annotated. The lanes labeled “1”, “2”, and “3” contain purified A_{2A}AR in lipid nanodiscs, the MSP1D1 scaffold protein only and A_{2A}AR purified in detergent micelles, respectively.

(C–F) Radioligand binding activity measurements of A_{2A}AR-Cy3 in lipid nanodiscs. Homologous competition binding with (C) the antagonist ZM241385, and competition binding experiments with (D) the agonist NECA, (E) agonist CGS21680 and (F) antagonist XAC. Morphine was included in each experiment as a negative control. The measured KD or Ki values are indicated in each panel. All error bars indicate s.e.m for 3 independent trials.

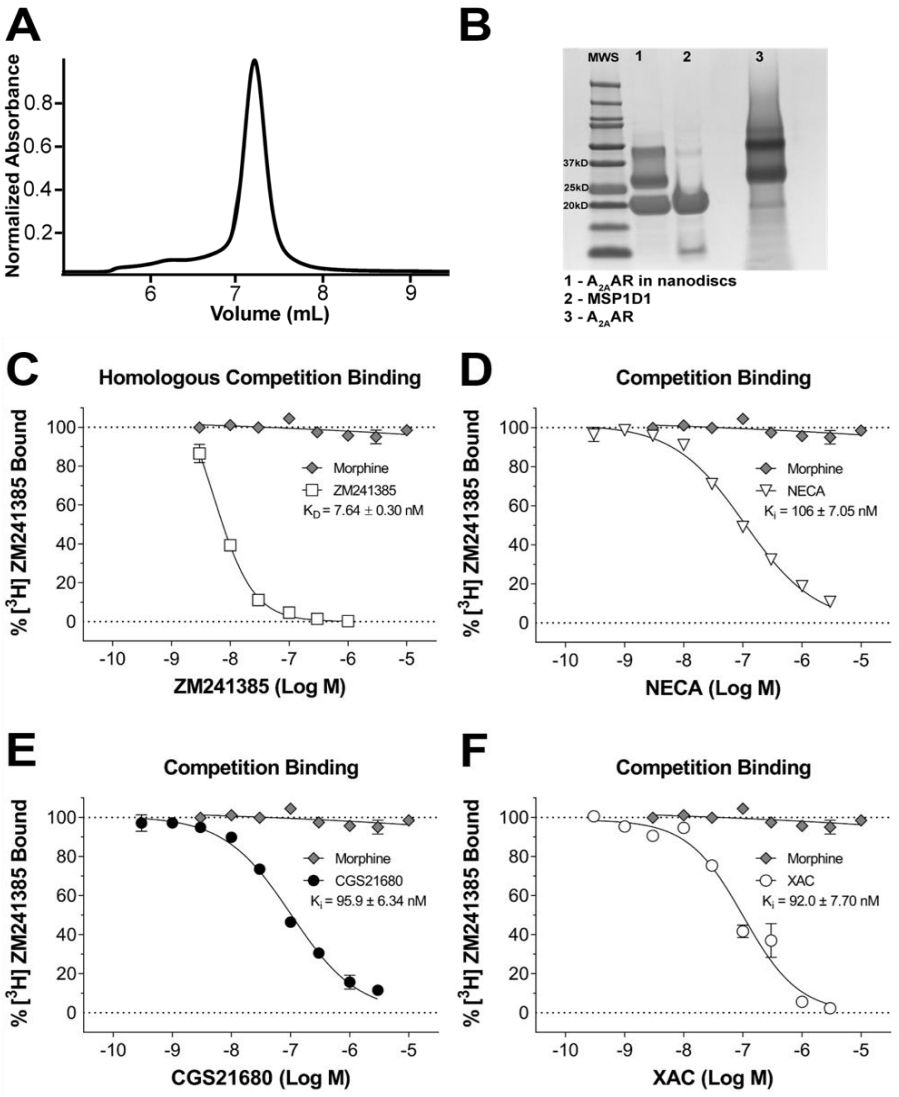

Figure S1. Related to Figure 9. Sample preparation characterization and pharmacological validation of A_{2A}AR[A289C]-Cy3 in lipid nanodiscs.

Figure S2. Related to Figure 9. Experimental design to study conformational dynamics of A_{2A}AR by single-molecule fluorescence and representative TIRF field-of-view images.

(A) Schematic showing Cy3 (green sphere)-labeled A_{2A}AR (red cylinders) in a nanodisc (lipids shown in orange and membrane scaffold protein shown in green) immobilized to a microscope slide using biotin (orange circles) and streptavidin (grey semi-circles). The microscope slides were passivated with poly-ethylene glycol (black wavy lines) to decrease non-specific interactions between the surface and the labeled nanodiscs. A 532 nm laser (green line) was used to excite the Cy3 fluorophore indirectly by creating the evanescent wave from the total internal reflection of the laser beam. This image was prepared with BioRender.

(B) A representative TIRF field-of-view image from immobilized nanodiscs containing A_{2A}AR-Cy3. Each bright spot corresponds to the fluorescence emission from a single Cy3-labeled A_{2A}AR molecule in lipid nanodiscs.

(C) Corresponding TIRF field-of-view image from a control experiment without bound streptavidin. Significantly fewer fluorescent spots are observed as compared to (B).

(D) A TIRF field-of-view image from a control experiment of a sample containing only imaging buffer.

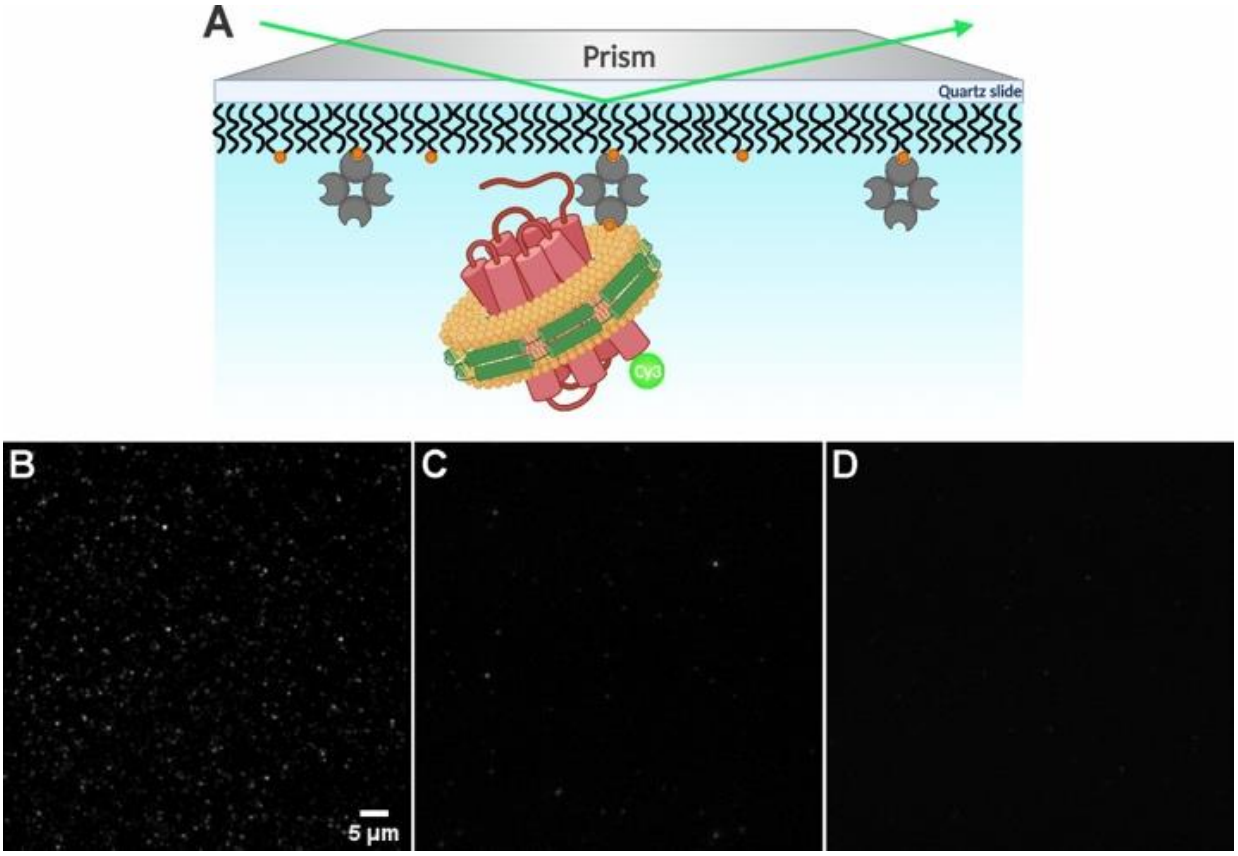

Figure S2. Related to Figure 9. Experimental design to study conformational dynamics of A_{2A}AR by single-molecule fluorescence and representative TIRF field-of-view images.

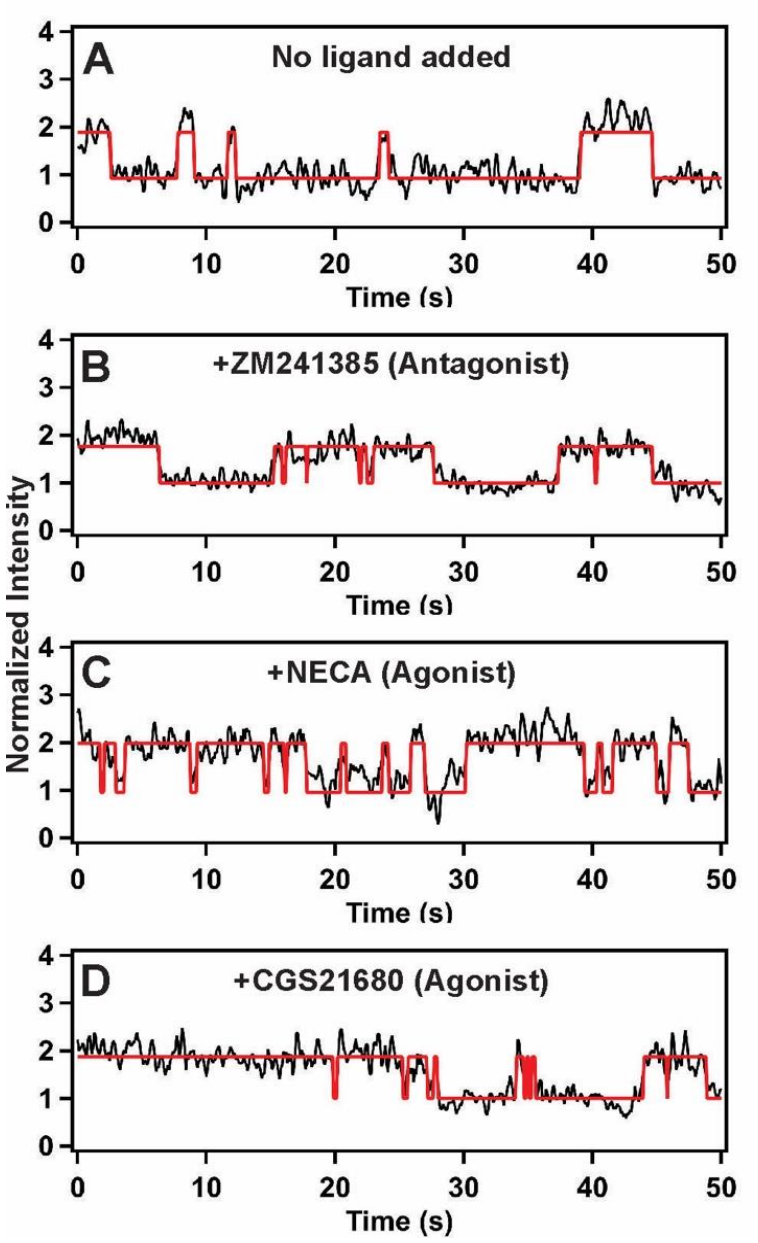

Figure S3. Related to Figure 10.

Representative fluorescence intensity trajectories from individual Cy3-labeled $A_{2A}AR$ single molecules in complexes with different ligands as annotated and with no ligand added (apo). Example trajectory fits showing reversible transitions between two states are presented.

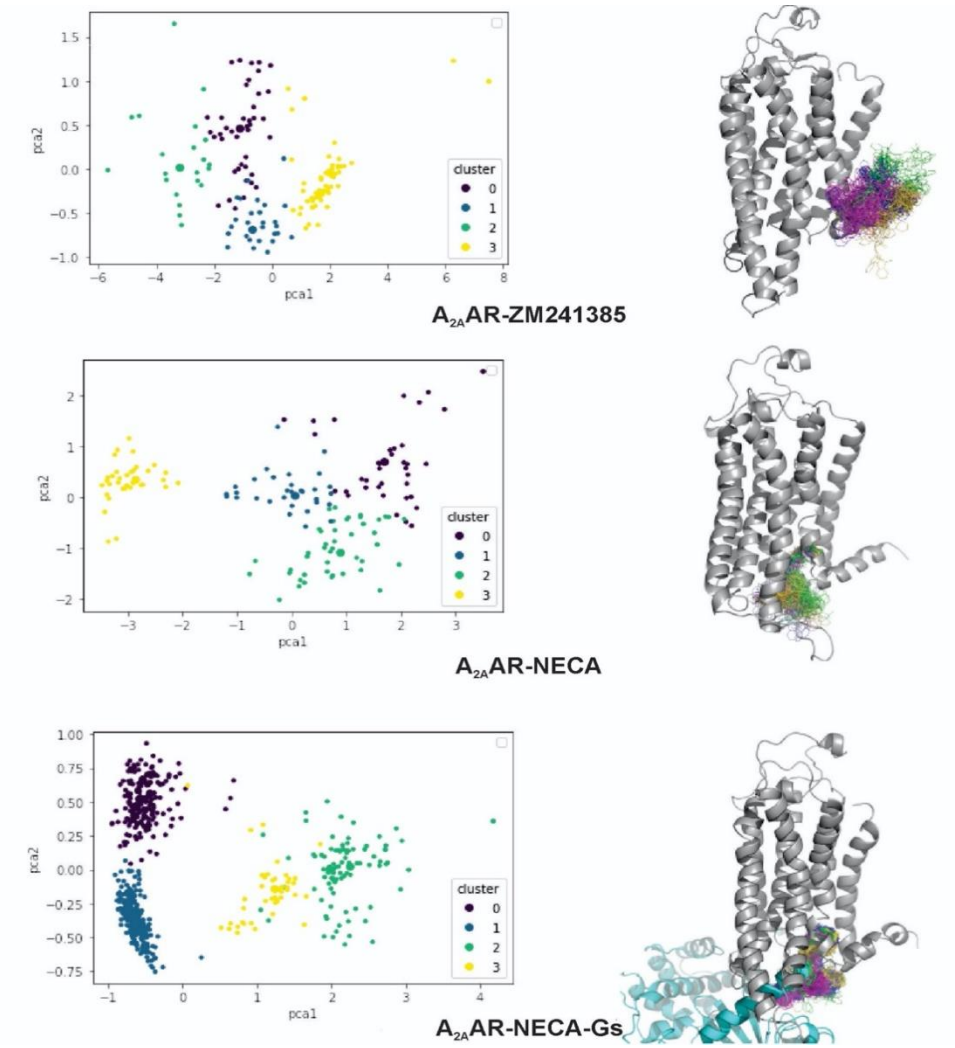

Figure S4. Related to Figure 10.

Principal component analysis (PCA) and cluster analysis (Affinity Propagation method, preference=-25, damping=.9) of the configurations visited by the dye during the pulled triplicate MD simulations on each relevant state (total simulation time 1.5 μS for each state). Analysis was performed with MDtraj. Four well defined clusters are defined in each case (left panels), and the 3D representation of these configurations on the starting structure of the receptor (grey ribbon representation) is shown on the corresponding right panels.

Table S1. Related to Figure 12. Percentage of time spent by A_{2A}AR-Cy3 molecules in one state before transitioning to a different state.

In each column, the percent time spent in state i before transitioning to state j was calculated by dividing the time spent at each transition state by the total time spent in all states for all molecules.

	State Transition					
A_{2A}AR Sample	1 to 2	2 to 1	2 to 3	3 to 2	1 to 3	3 to 1
APO	59.1%	28.8%	6.1%	5.3%	0.4%	0.3%
ZM241385	51.7%	35.7%	5.4%	5.7%	0.8%	0.7%
NECA	42.5%	31.1%	10.9%	13.7%	0.5%	1.3%
CGS21680	44.5%	28.8%	12.7%	11.7%	1.1%	1.2%

Table S2. Comparing state three transition events and the distributions of molecules showing the two and three states. Related to Figure 12.

	State 3 transition events		Distribution of molecules	
A_{2A}AR Sample	**Average time**	**Number of events %**	**Two states**	**Three states**
APO	1.1	10.6%	69%	31%
ZM241385	1.2	10.3%	70%	30%
NECA	1.4	17.4%	38%	62%
CGS21680	1.1	18.3%	40%	60%

Appendix II

A version of this appendix was originally published by Shushu Wei, Niloofar Gopal Pour, Sriram Tiruvadi-Krishnan, Arka Prabha Ray, Naveen Thakur, Matthew T. Eddy, Rajan Lamichhane on Communication Biology in November 2023. (Website: https://www.nature.com/articles/s42003-023-05603-6)

In this research, Shushu Wei implemented and supervised the project, conducted single-molecule experiments, collected, and analyzed data, and wrote and edited the manuscript. Niloofar Gopal Pour and Naveen Thakur conducted the expression, labeling, and purification of A_{2A}AR wild type and three different mutants. Besides, they also did the size exclusion chromatography and ligand binding assay. Sriram Tiruvadi-Krishnan modified customer written program and analyzed data, especially analyzed kinetic data. Rajan Lamichhane and Matthew T. Eddy supervised experiments and data analysis and contributed to writing the manuscript with input from all co-authors.

Figure S5. Analytical size exclusion chromatograms and SDS-PAGE image of purified A_{2A}AR[A289C] samples.

(A-C) Size exclusion chromatograms for A_{2A}AR[A289C,D52N] without ligand added (apo) and in complexes with NECA or ZM241385 in lipid nanodiscs. (D-F) Size exclusion chromatograms for A_{2A}AR[A289C,I92N] without ligand added (apo) and in complexes with NECA or ZM241385 in lipid nanodiscs. (G-I) Size exclusion chromatograms for A_{2A}AR[A289C,R291Q] without ligand added (apo) and in complexes with NECA or ZM241385 in lipid nanodiscs. (J) SDS-PAGE image of purified apo A_{2A}AR[A289C] and the three apo A_{2A}AR variants in detergent and lipid nanodisc preparations, shown for lanes: (1) A_{2A}AR[A289C] in DDM/CHS micelles, (2) A_{2A}AR[A289C,D52N] in DDM/CHS micelles, 3 A_{2A}AR[A289C,I92N] in DDM/CHS micelles, (4) A_{2A}AR[A289C,R291Q] in DDM/CHS micelles, (5) A_{2A}AR[A289C,I92N] in lipid nanodiscs, (6) A_{2A}AR[A289C,R291Q] in lipid nanodiscs, (7)A_{2A}AR[A289C,D52N] in lipid nanodiscs, (8) A_{2A}AR[A289C] in lipid nanodiscs, (9) MSP1D1. “MWS” is the employed molecular weight standard.

.

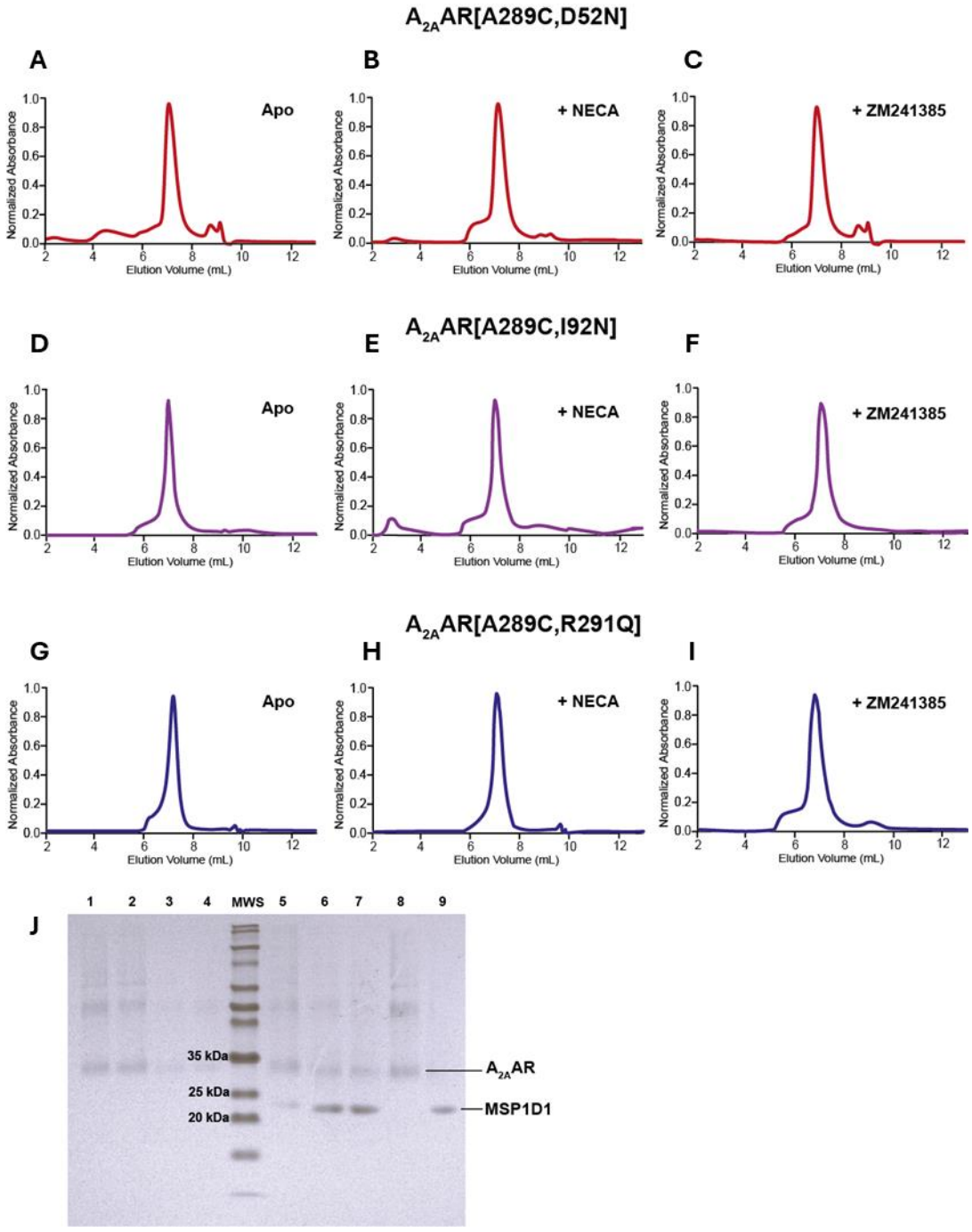

Figure S5. Analytical size exclusion chromatograms and SDS-PAGE image of purified A_{2A}AR[A289C] samples.

.

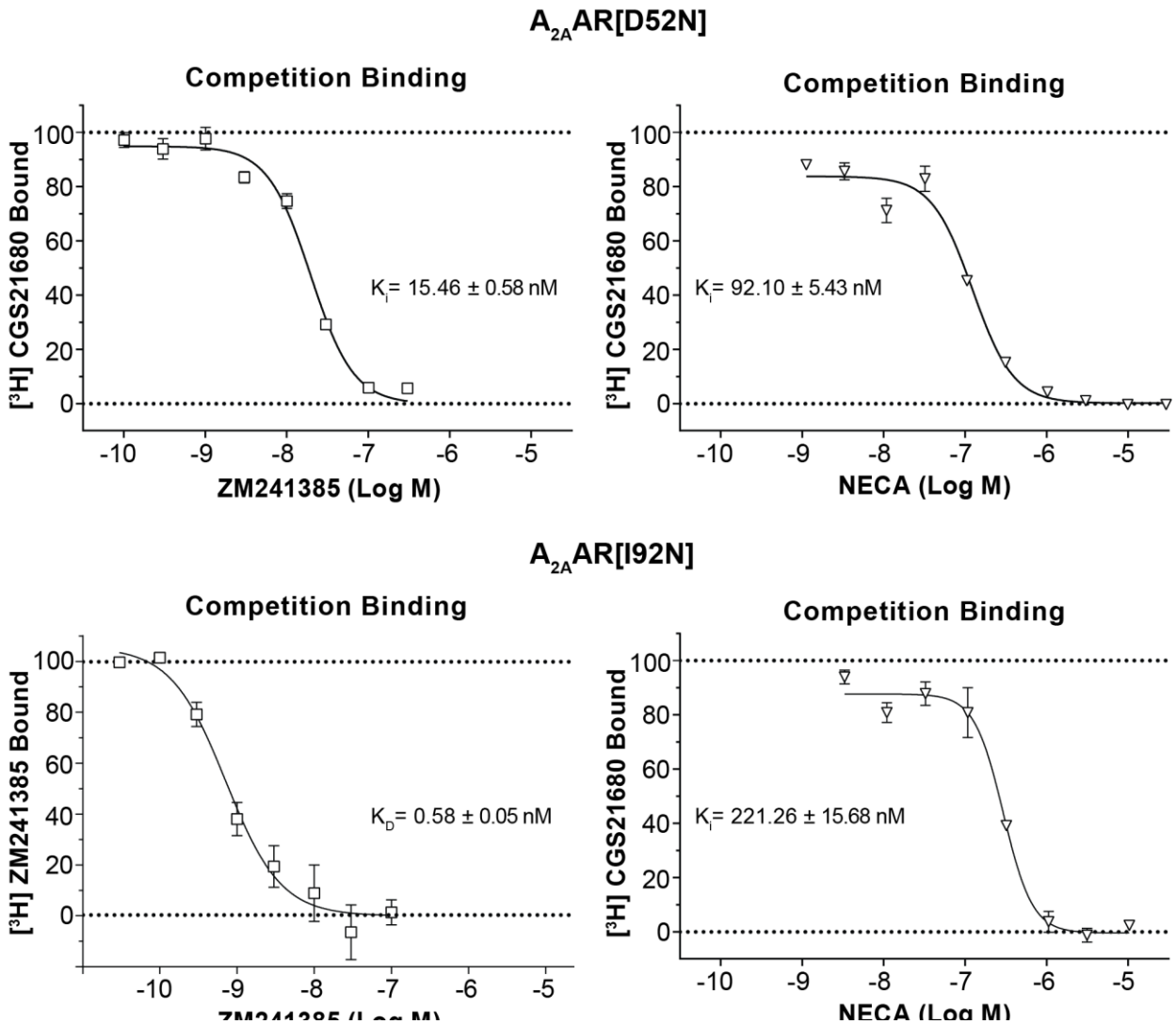

Figure S6. Pharmacological activity of A_{2A}AR[D52N] and A_{2A}AR[I92N] in lipid nanodiscs.

Competition binding experiments with the antagonist ZM241385 are shown in the left panels, and competition binding experiments with the agonist NECA are shown in the right panels. The measured KD or KI values are shown in each panel. Error bars indicate the s.e.m for n > 3 independent trials.

Figure S7. Dynamic single-molecule fluorescence time trajectories.

Dynamic single-molecule fluorescence time trajectories for (A-C) A_{2A}AR, (D-F) A_{2A}AR[D52N], (G-I) A_{2A}AR[I92N], and (j-l) A_{2A}AR[R291Q] in the absence of added ligand (apo) and for complexes with the antagonist ZM241385 and agonist NECA. The Cy3 intensity is normalized by the mean value of the lowest intensity state. The intensity trajectories (black) are fitted by a three-state hidden Markov model (red).

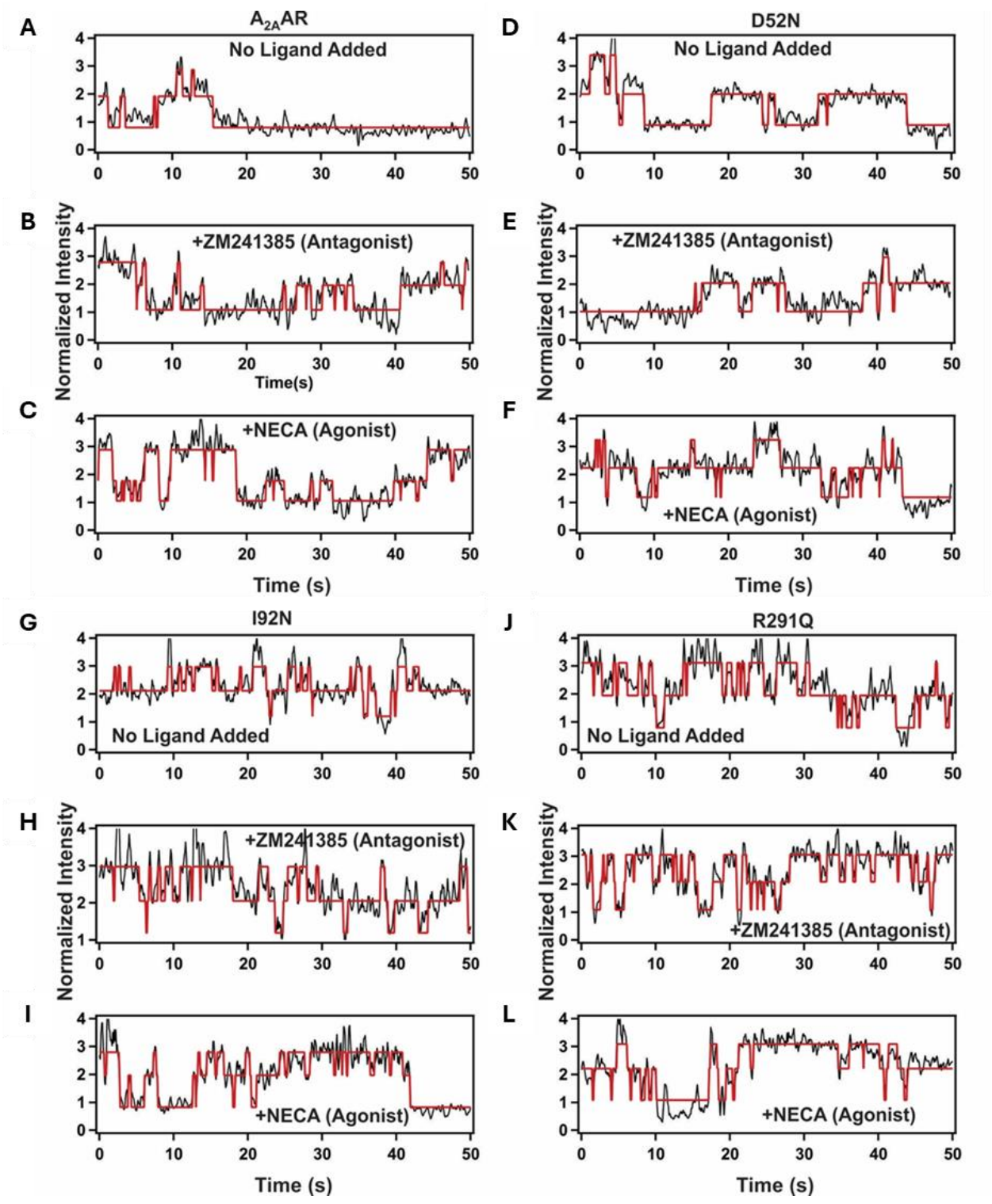

Figure S7. Dynamic single-molecule fluorescence time trajectories.

Figure S8. Dynamic single-molecule fluorescence time trajectories in the presence of mini-G_S.

Dynamic single-molecule fluorescence time trajectories in the presence of mini-G_S for (A-C) A_{2A}AR, (D-F) A_{2A}AR[D52N], (G-I) A_{2A}AR[I92N], and (J-L) A_{2A}AR[R291Q] in the absence of added ligand (apo) and for complexes with the antagonist ZM241385 and agonist NECA. The Cy3 intensity is normalized by the mean value of the lowest intensity state. The intensity trajectories (black) are fitted by a three-state hidden Markov model (red).

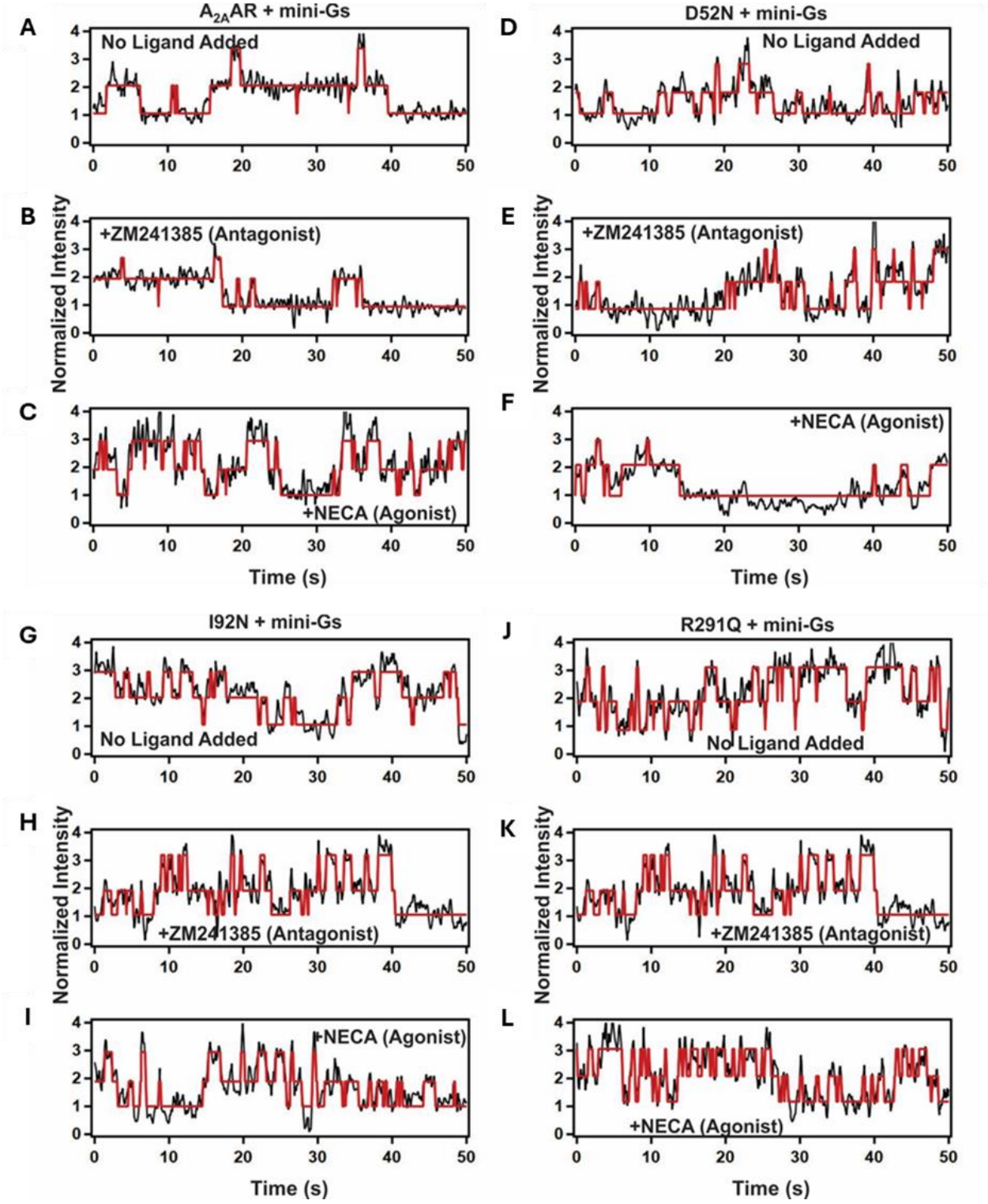

Figure S8. Dynamic single-molecule fluorescence time trajectories in the presence of mini-Gs.

Figure S9. Dwell time histograms.

(A-C) Representative dwell-time histograms for transitions of A2AAR between state 1 and 2 are plotted for different conditions in the absence of mini-Gs. The solid red lines are the corresponding best fits to a bi-exponential function. (D-F) Representative dwell time histograms for transitions of A2AAR between state 2 and 3 are plotted for different conditions in the absence of mini-Gs. The solid red lines are the corresponding best fits to a mono-exponential function. "N" corresponds to the number of transitions analyzed.

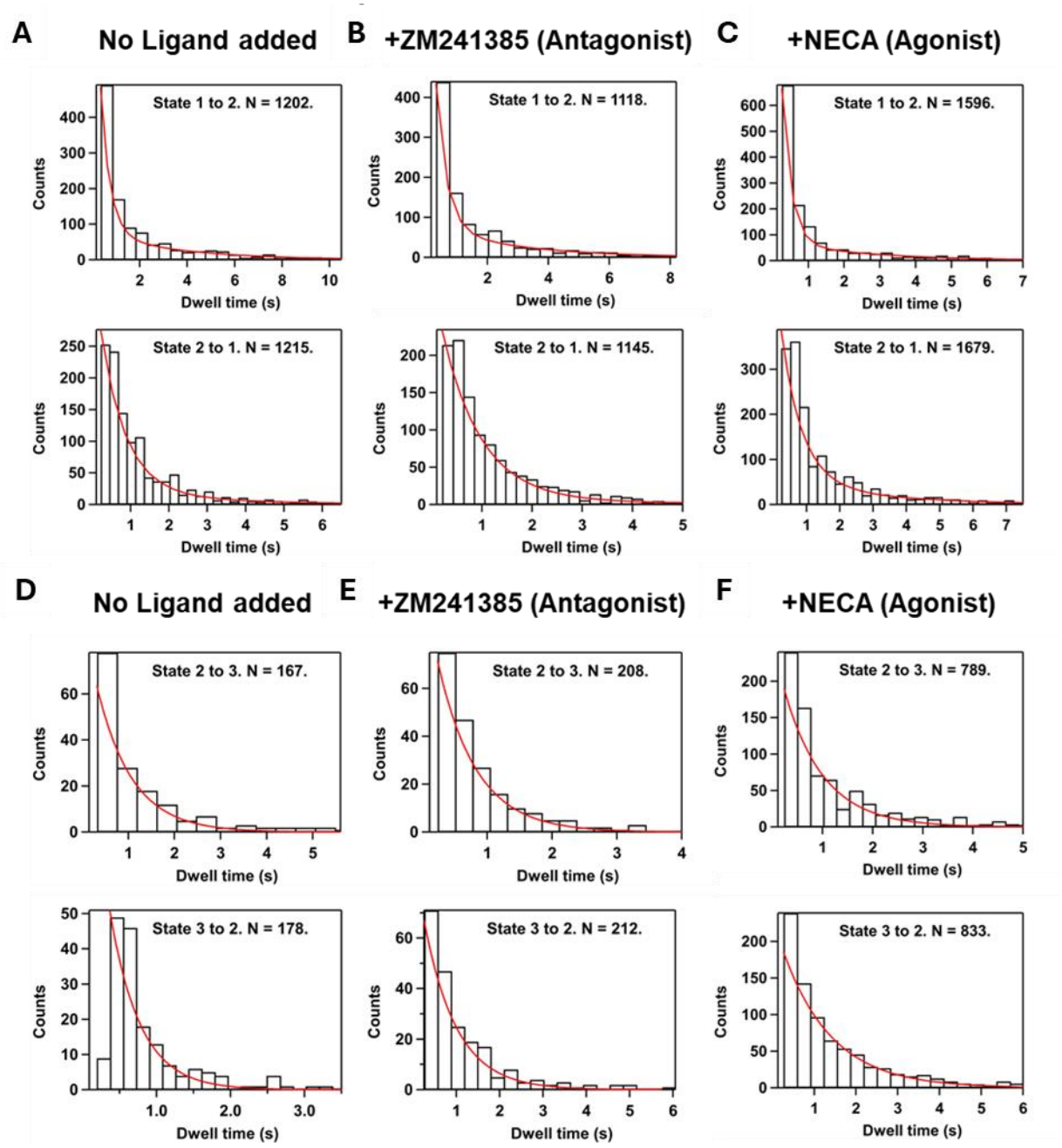

Figure S9. Dwell time histograms.

Figure S10. Dwell time analysis.

(A and B) Mean occupancy times in states 1, 2 and 3 of A2AAR and its variants are plotted for different conditions in the absence (A) and in the presence (B) of mini-GS. Error bars indicate the standard error of the mean.

(C and D) The average rate constant k for transitions of $A_{2A}AR$ between states 1 and 2 are shown for various conditions in the absence (C) and in the presence (D) of mini-GS. Error bars indicate the standard deviation. (E and F) The rate constant k for transitions of $A_{2A}AR$ between states 2 and 3 are shown for various conditions in the absence (E) and in the presence (F) of mini-G_S. Error bars indicate the standard deviation.

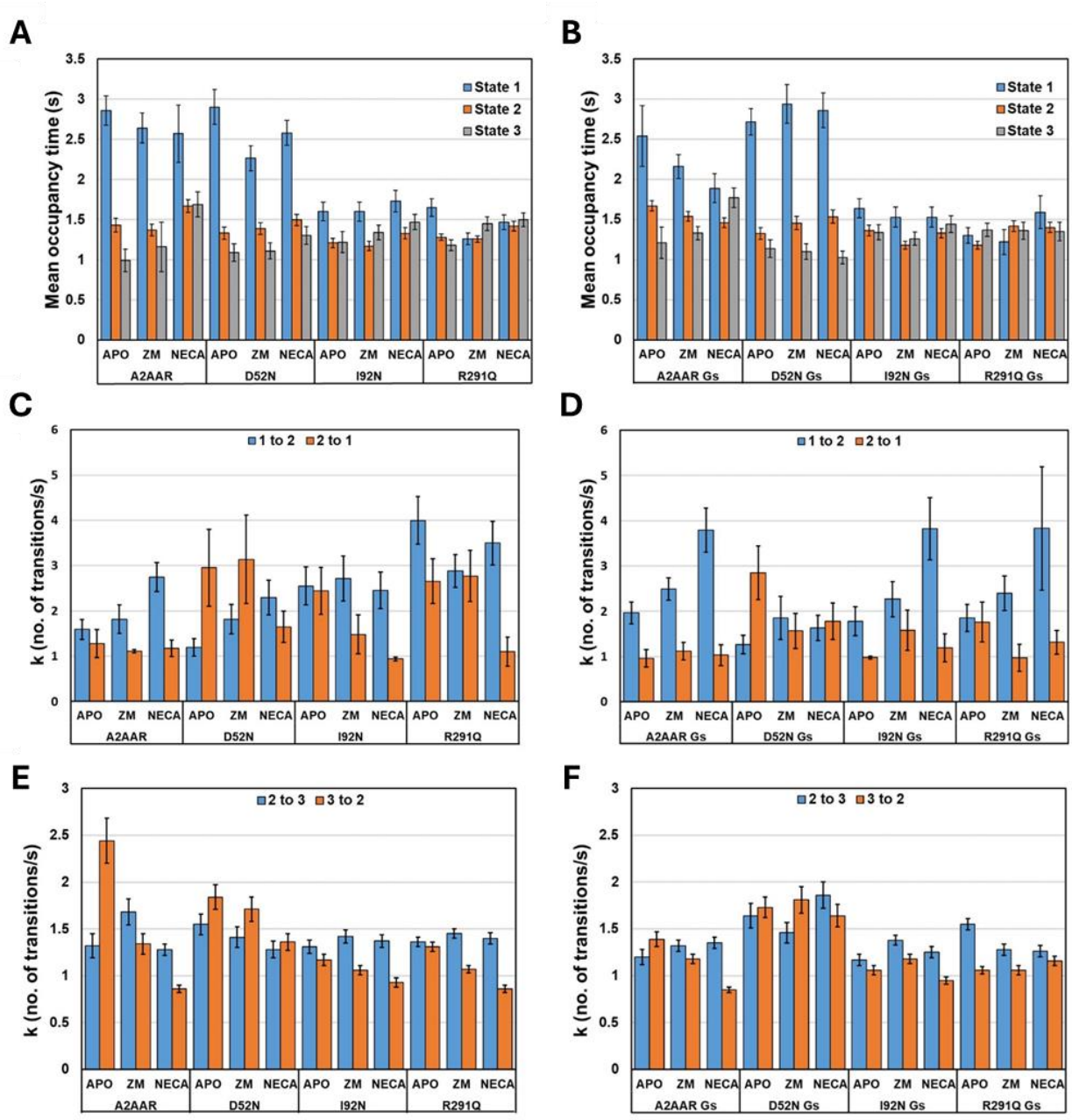

Figure S10. Dwell time analysis.

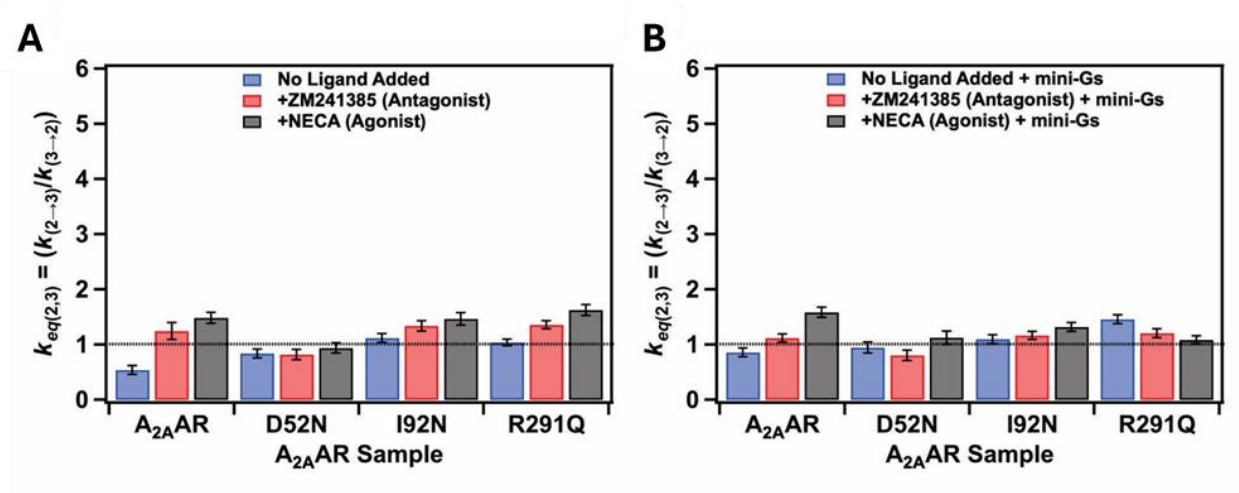

Figure S11. An expanded view of Figure 7 panels C and D

Here shown with the same Y axis range as Figure 7 panels (A) and (B).

Table S3. Oligonucleotide sequences for generating A_{2A}AR variants from the A_{2A}AR[A289C] template plasmid.

Primer Name	Sequence (Oligonucleotide, 5' to 3')	Source
A_{2A}AR_D52N_F	TTTGTGGTGTCACTGGCGGCGGCCAACATCGCA GTGGGTGTGCTCGCCATCC	IDT
A_{2A}AR_D52N_R	GGATGGCGAGCACACCCACTGCGATGTTGGCC GCCGCCAGTGACACCACAAA	IDT
A_{2A}AR_I92N_F	GTCCTCACGCAGAGCTCCAACTTCAGTCTCCTG GCCATCGCCATTGACCG	IDT
A_{2A}AR_I92N_R	CGGTCAATGGCGATGGCCAGGAGACTGAAGTTG GAGCTCTGCGTGAGGAC	IDT
A_{2A}AR_D52N_F	GTTGTGAATCCCTTCATTTACTGTTACCAAATCC GCGAGTTCCGCCAGAC	IDT
A_{2A}AR_D52N_R	GTCTGGCGGAACTCGCGGATTTGGTAACAGTAA ATGAAGGGATTCACAAC	IDT

Table S4. Relative areas of observed fluorescence emission intensity states, "1", "2", and "3" in the absence and presence of mini-GS.

Error bars indicate the standard deviation.

Sample	A_{2A}AR WT			D52N			I92N			R291Q		
	1	**2**	**3**	**1**	**2**	**3**	**1**	**2**	**3**	**1**	**2**	**3**
Apo	63% ± 1.10 %	37% ± 1.40 %	n/a	66 %± 2.50 %	26% ± 1.90 %	8%± 3.20 %	39 %± 0.70 %	43% ± 0.70 %	18% ± 1.10 %	40 %± 0.70 %	45% ± 0.70 %	15% ± 1.00 %
ZM241385	63% ± 0.90 %	37% ± 1.10 %	n/a	60 %± 1.70 %	31% ± 1.30 %	9%± 2.00 %	41 %± 1.00 %	40% ± 0.80 %	19% ± 1.10 %	34 %± 1.00 %	48% ± 0.90 %	18% ± 0.80 %
NECA	49% ± 0.70 %	37% ± 0.70 %	14% ± 1.00 %	59 %± 1.90 %	32% ± 1.40 %	9%± 2.10 %	39 %± 1.00 %	41% ± 0.90 %	20% ± 1.40 %	33 %± 0.60 %	45% ± 0.60 %	22% ± 0.80 %

Sample	A_{2A}AR WT + G_S			D52N + G_S			I92N + G_S			R291Q + G_S		
	1	**2**	**3**	**1**	**2**	**3**	**1**	**2**	**3**	**1**	**2**	**3**
Apo	54% ± 1.00 %	38% ± 1.0 %	8% ± 1.4 %	64% ± 2.80 %	28% ± 2.10 %	7% ± 3.10 %	35% ± 0.60 %	47% ± 0.60 %	18% ± 0.80 %	30% ± 0.70 %	45% ± 0.60 %	25% ± 0.90 %
ZM241385	49% ± 1.00 %	43% ± 0.90 %	8%± 1.10 %	66% ± 3.10 %	27% ± 2.40 %	7%± 3.40 %	35% ± 1.00 %	47% ± 0.90 %	18% ± 1.30 %	28% ± 1.00 %	54% ± 0.80 %	18% ± 1.10 %
NECA	38% ± 1.00 %	41% ± 0.90 %	21% ± 1.20 %	62% ± 1.40 %	31% ± 1.10 %	7%± 1.80 %	32% ± 0.60 %	48% ± 0.80 %	20% ± 1.00 %	33% ± 0.70 %	50% ± 0.60 %	17% ± 0.80 %

Table S5. Number of dynamic molecules analyzed.

Sample	A_{2A}AR WT		D52N		I92N		R291Q	
	-Gs	+Gs	-Gs	+Gs	-Gs	+Gs	-Gs	+Gs
Apo	149	163	166	156	140	148	237	172
ZM241385	153	220	156	151	144	163	208	138
NECA	160	160	155	153	148	153	190	162

Table S6. Percentage of molecules transitioning between state 1 and state 3.

Sample	A_{2A}AR WT		D52N		I92N		R291Q	
	1 to 3	3 to 1	1 to 3	3 to 1	1 to 3	3 to 1	1 to 3	3 to 1
Apo	0.40%	0.40%	1.30%	1.50%	1.60%	2.10%	0.80%	1.50%
ZM241385	0.60%	0.90%	0.30%	0.50%	2.30%	3.00%	1.20%	1.70%
NECA	0.60%	0.90%	0.70%	1.40%	2.00%	2.50%	1.40%	2.70%

Sample	A_{2A}AR WT + G_S		D52N + G_S		I92N + G_S		R291Q + G_S	
	1 to 3	3 to 1	1 to 3	3 to 1	1 to 3	3 to 1	1 to 3	3 to 1
Apo	0.50%	0.90%	0.80%	1.60%	2.20%	3.40%	1.90%	3.30%
ZM241385	1.10%	1.40%	1.30%	2.20%	1.70%	2.50%	1.30%	1.40%
NECA	0.70%	1.40%	1.20%	1.70%	2.20%	1.70%	1.30%	1.40%

Table S7. Mean-occupancy times ± standard error of the mean in seconds of observed fluorescence emission intensity states, "1", "2", and "3" in the absence and presence of mini-G_S.

Sample	$A_{2A}AR$ WT			D52N			I92N			R291Q		
	1	**2**	**3**	**1**	**2**	**3**	**1**	**2**	**3**	**1**	**2**	**3**
Apo	2.86 ± 0.18	1.43 ± 0.09	0.99 ± 0.14	2.90 ± 0.22	1.33 ± 0.08	1.09 ± 0.11	1.60 ± 0.12	1.21 ± 0.06	1.22 ± 0.13	1.65 ± 0.11	1.28 ± 0.04	1.18 ± 0.07
ZM241385	2.64 ± 0.19	1.37 ± 0.07	1.16 ± 0.31	2.26 ± 0.16	1.39 ± 0.07	1.11 ± 0.10	1.60 ± 0.12	1.17 ± 0.06	1.34 ± 0.09	1.26 ± 0.07	1.26 ± 0.04	1.45 ± 0.09
NECA	2.57 ± 0.36	1.67 ± 0.08	1.69 ± 0.16	2.58 ± 0.15	1.50 ± 0.07	1.30 ± 0.11	1.73 ± 0.13	1.33 ± 0.07	1.47 ± 0.09	1.47 ± 0.09	1.42 ± 0.06	1.50 ± 0.08

Sample	$A_{2A}AR$ WT + G_S			D52N + G_S			I92N + G_S			R291Q + G_S		
	1	2	3	1	2	3	1	2	3	1	2	3
Apo	2.54 ± 0.38	1.67 ± 0.06	1.21 ± 0.20	2.72 ± 0.16	1.33 ± 0.07	1.14 ± 0.11	1.64 ± 0.12	1.36 ± 0.07	1.34 ± 0.09	1.30 ± 0.10	1.18 ± 0.05	1.37 ± 0.08
ZM241385	2.16 ± 0.15	1.54 ± 0.06	1.33 ± 0.08	2.94 ± 0.24	1.45 ± 0.08	1.10 ± 0.10	1.53 ± 0.12	1.18 ± 0.05	1.26 ± 0.08	1.22 ± 0.16	1.42 ± 0.07	1.36 ± 0.10
NECA	1.89 ± 0.18	1.46 ± 0.06	1.77 ± 0.12	2.86 ± 0.22	1.54 ± 0.08	1.03 ± 0.08	1.53 ± 0.13	1.33 ± 0.06	1.44 ± 0.10	1.59 ± 0.21	1.40 ± 0.06	1.35 ± 0.11

Table S8. The equilibrium rate constant ratios (k_{eq} ± standard deviation) calculated for each state transition are tabulated.

Sample	**A_{2A}AR WT** **1↔2**	**D52N** **1↔2**	**I92N** **1↔2**	**R291Q** **1↔2**
Apo	1.24 ± 0.35	0.40 ± 0.13	1.04 ± 0.28	1.51 ± 0.34
ZM241385	1.64 ± 0.29	0.58 ± 0.21	1.83 ± 0.63	1.04 ± 0.25
NECA	2.34 ± 0.45	1.39 ± 0.37	2.61 ± 0.45	3.17 ± 1.02
Sample	A_{2A}AR WT + Gs 1↔2	D52N + Gs 1↔2	I92N + Gs 1↔2	R291Q + Gs 1↔2
Apo	2.05 ± 0.49	0.45 ± 0.12	1.82 ± 0.33	1.05 ± 0.31
ZM241385	2.22 ± 0.44	1.18 ± 0.42	1.44 ± 0.47	2.47 ± 0.86
NECA	3.68 ± 0.95	0.92 ± 0.26	3.21 ± 1.02	2.92 ± 1.19
Sample	A_{2A}AR 2↔3	D52N 2↔3	I92N 2↔3	R291Q 2↔3
Apo	0.54 ± 0.08	0.84 ± 0.08	1.12 ± 0.08	1.04 ± 0.06
ZM241385	1.25 ± 0.15	0.82 ± 0.09	1.34 ± 0.09	1.36 ± 0.07
NECA	1.49 ± 0.10	0.94 ± 0.09	1.47 ± 0.11	1.63 ± 0.10
Sample	A_{2A}AR + Gs 2↔3	D52N + Gs 2↔3	I92N + Gs 2↔3	R291Q + Gs 2↔3
Apo	0.86 ± 0.08	0.95 ± 0.10	1.10 ± 0.08	1.46 ± 0.08
ZM241385	1.12 ± 0.07	0.81 ± 0.09	1.17 ± 0.07	1.21 ± 0.08
NECA	1.59 ± 0.09	1.13 ± 0.12	1.32 ± 0.08	1.09 ± 0.07

Table S9. Mono-exponential and bi-exponential fitting results from the dwell time analysis of $A_{2A}AR$ without ligand added (apo) and with ligands in the absence of mini-G_S.

"A" is the reported amplitude and "sd" the calculated standard deviation, as described in the Methods section.

States	A ± sd (%)		k ± sd (1/s)		Reduced χ^2
$A_{2A}AR$—APO					
1 to 2	100		0.90 ± 0.04		2.41
	92.3 ± 9.7	7.7 ± 0.9	2.54 ± 0.2	0.29 ± 0.02	0.63
2 to 1	100		1.14 ± 0.04		0.47
	93.7 ± 5.7	6.3 ± 2.4	1.55 ± 0.1	0.36 ± 0.06	0.27
2 to 3	100		1.32 ± 0.13		1.4
	95.0 ± 19.1	5.0 ± 4.0	2.1 ± 0.45	0.29 ± 0.18	0.43
3 to 2	100		2.44 ± 0.24		0.58
	99.3 ± 21.4	0.7 ± 0.9	2.7 ± 0.36	0.22 ± 0.32	0.51
$A_{2A}AR$—NECA					
1 to 2	100		1.98 ± 0.07		1.99
	95.4 ± 8.4	4.6 ± 0.5	3.87 ± 0.26	0.39 ± 0.02	0.6
2 to 1	100		0.92 ± 0.03		1.82
	89.0 ± 5.6	11.0 ± 2.2	1.63 ± 0.13	0.36 ± 0.03	0.94
2 to 3	100		1.28 ± 0.06		1.29
	82.2 ± 11.6	17.8 ± 4.7	3.13 ± 0.58	0.71 ± 0.08	0.73
3 to 2	100		0.86 ± 0.04		0.57
	67.2 ± 13.4	32.8 ± 7.0	2.66 ± 0.78	0.64 ± 0.06	0.28
$A_{2A}AR$—ZM241385					
1 to 2	100		0.92 ± 0.04		1.36
	91.5 ± 10.7	8.5 ± 1.2	2.91 ± 0.30	0.36 ± 0.03	0.45
2 to 1	100		1.11 ± 0.04		0.53
	97.9 ± 5.3	2.1 ± 1.0	1.30 ± 0.07	0.22 ± 0.06	0.34
2 to 3	100		1.68 ± 0.14		0.38
	73.0 ± 61.6	27 ± 74.8	2.50 ± 2.03	1.15 ± 0.88	0.35
3 to 2	100		1.34 ± 0.11		0.81
	94.8 ± 14.7	5.2 ± 14.9	1.67 ± 0.47	0.45 ± 0.66	0.7

Table S10. Mono-exponential and bi-exponential fitting results from the dwell time analysis of A_{2A}AR[R291Q] without ligand added (apo) and with ligands in the absence of mini-G_S.

States	A ± sd (%)		k ± sd (1/s)		Reduced χ^2
A_{2A}AR[R291Q]—APO					
1 to 2	100		1.18 ± 0.04		3.32
	93.3 ± 11.8	6.7 ± 0.5	6.57 ± 0.53	0.62 ± 0.03	1.04
2 to 1	100		1.05 ± 0.03		2.07
	88.2 ± 17.4	11.8 ± 1.2	4.19 ± 0.51	0.71 ± 0.03	1.04
2 to 3	100		1.36 ± 0.05		1.12
	72.4 ± 15.1	27.6 ± 18.2	2.25 ± 0.60	0.92 ± 0.18	0.97
3 to 2	100		1.31 ± 0.05		1.21
	91.9 ± 48.4	8.1 ± 1.2	6.07 ± 1.37	0.97 ± 0.06	0.42
A_{2A}AR[R291Q]—NECA					
1 to 2	100		1.75 ± 0.06		2.26
	93.0 ± 10.0	7.0 ± 0.8	5.22 ± 0.42	0.65 ± 0.04	0.63
2 to 1	100		0.94 ± 0.03		1.24
	84.0 ± 7.0	16.0 ± 7.6	1.43 ± 0.18	0.50 ± 0.08	0.91
2 to 3	100		1.40 ± 0.06		1.34
	84.3 ± 11.8	15.7 ± 3.3	3.66 ± 0.58	0.76 ± 0.07	0.55
3 to 2	100		0.86 ± 0.04		1.74
	89.1 ± 11.7	10.9 ± 13.2	1.11 ± 0.19	0.42 ± 0.17	1.59
A_{2A}AR[R291Q]—ZM241385					
1 to 2	100		1.61 ± 0.05		1.71
	89.4 ± 7.7	10.6 ± 1.1	4.49 ± 0.35	0.72 ± 0.04	0.94
2 to 1	100		1.07 ± 0.03		2.15
	87.7 ± 19.2	12.3 ± 1.3	4.41 ± 0.59	0.76 ± 0.04	1.36
2 to 3	100		1.45 ± 0.05		2.31
	74.5 ± 10.2	25.5 ± 11.1	2.71 ± 0.60	0.94 ± 0.14	1.93
3 to 2	100		1.07 ± 0.04		0.39
	72.5 ± 12.0	27.5 ± 14.0	1.90 ± 0.45	0.72 ± 0.12	0.3

Table S11. Mono-exponential and bi-exponential fitting results from the dwell time analysis of A_{2A}AR[I92N] without ligand added (apo) and with ligands in the absence of mini-G_s.

States	A ± sd (%)		k ± sd (1/s)		Reduced χ^2
A_{2A}AR[I92N]—APO					
1 to 2	100		1.37 ± 0.06		1
	90.4 ± 10.6	9.6 ± 1.4	3.99 ± 0.41	0.58 ± 0.04	0.39
2 to 1	100		1.67 ± 0.07		1.85
	93.3 ± 14.1	6.7 ± 1.5	3.16 ± 0.35	0.59 ± 0.06	1.04
2 to 3	100		1.31 ± 0.07		0.96
	76.9 ± 23.4	23.1 ± 5.9	4.28 ± 1.43	0.93 ± 0.10	0.53
3 to 2	100		1.17 ± 0.06		1.07
	77.5 ± 53.1	22.5 ± 58.9	1.55 ± 0.73	0.78 ± 0.51	1.05
A_{2A}AR[I92N]—NECA					
1 to 2	100		1.75 ± 0.08		2.14
	93.2 ± 9.6	6.8 ± 1.2	3.47 ± 0.32	0.49 ± 0.04	0.81
2 to 1	100		0.94 ± 0.04		0.98
	96.0 ± 5.9	4.0 ± 3.8	1.12 ± 0.10	0.31 ± 0.13	0.87
2 to 3	100		1.37 ± 0.07		0.94
	74.0 ± 37.0	26.0 ± 5.3	5.77 ± 2.51	1.08 ± 0.10	0.56
3 to 2	100		0.93 ± 0.05		0.93
	79.6 ± 11.1	20.4 ± 9.3	1.82 ± 0.42	0.53 ± 0.09	0.44
A_{2A}AR[I92N]—ZM241385					
1 to 2	100		1.42 ± 0.06		1.45
	89.5 ± 11.8	10.5 ± 1.6	4.24 ± 0.50	0.67 ± 0.05	0.64
2 to 1	100		1.10 ± 0.04		1.35
	77.5 ± 8.5	22.5 ± 7.1	2.29 ± 0.41	0.67 ± 0.08	0.75
2 to 3	100		1.42 ± 0.07		0.5
	78.1 ± 21.9	21.9 ± 4.4	5.12 ± 1.40	1.00 ± 0.09	0.24
3 to 2	100		1.06 ± 0.05		1.07
	95.9 ± 7.1	4.1 ± 4.7	1.25 ± 0.14	0.33 ± 0.17	0.92

Table S12. Mono-exponential and bi-exponential fitting results from the dwell time analysis of A_{2A}AR[D52N] without ligand added (apo) and with ligands in the absence of mini-G_S.

States	A ± sd (%)		k ± sd (1/s)		Reduced χ^2
A_{2A}AR[D52N]—APO					
1 to 2	100		0.86 ± 0.04		1.36
	93.3 ± 9.0	6.7 ± 1.2	1.67 ± 0.14	0.24 ± 0.02	0.42
2 to 1	100		1.26 ± 0.05		1.12
	85.2 ± 25.4	14.8 ± 2.1	5.00 ± 0.99	0.88 ± 0.06	0.58
2 to 3	100		1.55 ± 0.11		0.28
	93.4 ± 392	6.6 ± 1.8	9.58 ± 12.6	1.27 ± 0.15	0.15
3 to 2	100		1.84 ± 0.13		0.44
	91.5 ± 22.3	8.5 ± 4.8	3.39 ± 0.73	0.79 ± 0.20	0.29
A_{2A}AR[D52N]—NECA					
1 to 2	100		0.98 ± 0.05		3
	94.7 ± 14.4	5.3 ± 0.7	3.33 ± 0.33	0.35 ± 0.02	0.86
2 to 1	100		1.01 ± 0.04		1.03
	85.4 ± 10.6	14.6 ± 2.9	2.51 ± 0.33	0.55 ± 0.05	0.46
2 to 3	100		1.28 ± 0.09		1.52
	87.6 ± 27.7	12.4 ± 4.7	3.38 ± 0.92	0.69 ± 0.12	0.53
3 to 2	100		1.36 ± 0.09		0.87
	90.7 ± 16.9	9.3 ± 4.9	2.40 ± 0.48	0.54 ± 0.13	0.36
A_{2A}AR[D52N]—ZM241385					
1 to 2	100		0.80 ± 0.04		3.81
	92.5 ± 14.5	7.5 ± 1.0	2.81 ± 0.32	0.34 ± 0.02	0.68
2 to 1	100		1.12 ± 0.04		1
	86.8 ± 31.2	13.2 ± 1.6	5.51 ± 1.17	0.82 ± 0.05	0.53
2 to 3	100		1.41 ± 0.11		0.73
	96.1 ± 649	3.9 ± 1.1	10.1 ± 18.7	1.12 ± 0.14	0.46
3 to 2	100		1.71 ± 0.13		0.63
	91.3 ± 18.2	8.7 ± 9.0	2.61 ± 0.66	0.72 ± 0.31	0.49

Table S13. Mono-exponential and bi-exponential fitting results from the dwell time analysis of $A_{2A}AR$ without ligand added (apo) and with ligands in the presence of mini-G_S.

States	A ± sd (%)		k ± sd (1/s)		Reduced χ^2
$A_{2A}AR$—APO with Mini-G_S					
1 to 2	100		1.19 ± 0.05		2.89
	93.6 ± 7.9	6.4 ± 0.7	2.97 ± 0.21	0.33 ± 0.02	0.93
2 to 1	100		0.78 ± 0.02		1.34
	84.3 ± 5.7	15.7 ± 4.6	1.32 ± 0.14	0.39 ± 0.04	0.72
2 to 3	100		1.20 ± 0.08		1.55
	80.9 ± 24.6	19.1 ± 4.9	4.11 ± 1.27	0.78 ± 0.09	0.73
3 to 2	100		1.39 ± 0.08		0.52
	83.3 ± 19.2	16.7 ± 23.2	2.01 ± 0.62	0.78 ± 0.35	0.42
$A_{2A}AR$—NECA with Mini-G_S					
1 to 2	100		2.45 ± 0.09		1.74
	95.0 ± 10.3	5.0 ± 0.5	5.40 ± 0.40	0.57 ± 0.03	0.66
2 to 1	100		0.86 ± 0.03		1.9
	84.9 ± 5.9	15.1 ± 5.3	1.37 ± 0.15	0.43 ± 0.05	1.43
2 to 3	100		1.35 ± 0.06		2.1
	84.9 ± 33.6	15.1 ± 1.9	7.56 ± 1.96	1.01 ± 0.06	1.26
3 to 2	100		0.85 ± 0.03		1.29
	87.7 ± 7.0	12.3 ± 4.2	1.43 ± 0.17	0.38 ± 0.05	0.5
$A_{2A}AR$—ZM241385 with Mini-G_S					
1 to 2	100		1.60 ± 0.05		2.09
	94.4 ± 6.4	5.6 ± 0.5	3.66 ± 0.20	0.39 ± 0.02	0.55
2 to 1	100		0.89 ± 0.02		1.28
	81.8 ± 5.0	18.2 ± 4.1	1.60 ± 0.15	0.48 ± 0.04	0.65
2 to 3	100		1.32 ± 0.06		1.16
	78.6 ± 27.4	21.4 ± 3.3	6.13 ± 1.77	1.00 ± 0.07	0.59
3 to 2	100		1.18 ± 0.05		0.54
	91.5 ± 9.5	8.5 ± 10.4	1.51 ± 0.22	0.55 ± 0.23	0.44

Table S 14. Mono-exponential and bi-exponential fitting results from the dwell time analysis of A_{2A}AR[R291Q] without ligand added (apo) and with ligands in the presence of mini-G_S.

States	A ± sd (%)		k ± sd (1/s)		Reduced χ^2
A_{2A}AR[R291Q]—APO with Mini-G_S					
1 to 2	100		1.47 ± 0.05		1.48
	91.5 ± 5.9	8.5 ± 1.8	2.44 ± 0.18	0.52 ± 0.05	0.56
2 to 1	100		1.24 ± 0.04		0.75
	85.7 ± 10.6	14.3 ± 4.5	2.38 ± 0.34	0.69 ± 0.08	0.47
2 to 3	100		1.55 ± 0.06		1.07
	63.7 ± 13.0	36.3 ± 15.7	3.23 ± 1.19	1.16 ± 0.16	0.92
3 to 2	100		1.06 ± 0.04		1.23
	90.4 ± 7.5	9.6 ± 6.9	1.43 ± 0.19	0.45 ± 0.12	0.96
A_{2A}AR[R291Q]—NECA with Mini-G_S					
1 to 2	100		1.32 ± 0.05		1.22
	89.0 ± 19.8	11.0 ± 1.2	6.77 ± 1.03	0.85 ± 0.05	0.59
2 to 1	100		1.00 ± 0.03		0.96
	84.8 ± 6.3	15.2 ± 3.8	1.88 ± 0.21	0.49 ± 0.05	0.49
2 to 3	100		1.26 ± 0.06		0.8
	82.3 ± 40.3	17.7 ± 2.6	7.14 ± 2.43	0.97 ± 0.07	0.48
3 to 2	100		1.16 ± 0.05		2.11
	98.9 ± 6.5	1.1 ± 1.0	1.29 ± 0.08	0.13 ± 0.12	1.79
A_{2A}AR[R291Q]—ZM241385 with Mini-G_S					
1 to 2	100		1.93 ± 0.07		1.42
	92.8 ± 7.5	7.2 ± 1.4	3.22 ± 0.26	0.56 ± 0.05	0.39
2 to 1	100		0.87 ± 0.03		1.16
	92.0 ± 5.7	8.0 ± 4.0	1.17 ± 0.11	0.33 ± 0.07	0.77
2 to 3	100		1.28 ± 0.06		0.64
	69.6 ± 15.4	30.4 ± 9.5	3.36 ± 1.12	0.93 ± 0.11	0.45
3 to 2	100		1.06 ± 0.05		1.22
	96.4 ± 7.1	3.6 ± 3.6	1.26 ± 0.12	0.30 ± 0.15	1.01

Table S15. Mono-exponential and bi-exponential fitting results from the dwell time analysis of A_{2A}AR[I92N] without ligand added (apo) and with ligands in the presence of mini-G_S.

States	A ± sd (%)		k ± sd (1/s)		Reduced χ^2
A_{2A}AR[I92N]—APO with Mini-G_S					
1 to 2	100		1.37 ± 0.06		1.93
	93.5 ± 7.7	6.5 ± 1.2	2.46 ± 0.20	0.36 ± 0.04	0.5
2 to 1	100		0.98 ± 0.03		0.84
	99.0 ± 5.1	1.0 ± 1.0	1.06 ± 0.06	0.18 ± 0.11	0.74
2 to 3	100		1.17 ± 0.06		0.44
	81.1 ± 12.0	18.9 ± 7.8	2.41 ± 0.53	0.66 ± 0.11	0.2
3 to 2	100		1.06 ± 0.05		1.36
	97.4 ± 7.7	2.6 ± 4.1	1.18 ± 0.13	0.29 ± 0.23	1.32
A_{2A}AR[I92N]—NECA with Mini-G_S					
1 to 2	100		1.43 ± 0.06		2.3
	91.6 ± 16.0	8.4 ± 0.9	6.25 ± 0.74	0.73 ± 0.04	1.01
2 to 1	100		0.99 ± 0.03		0.58
	83.3 ± 6.8	16.7 ± 6.4	1.61 ± 0.21	0.52 ± 0.07	0.31
2 to 3	100		1.25 ± 0.06		1.74
	74.6 ± 25.9	25.4 ± 4.1	5.29 ± 1.68	0.97 ± 0.07	1.23
3 to 2	100		0.95 ± 0.04		0.8
	98.8 ± 5.9	1.2 ± 1.5	1.02 ± 0.07	0.19 ± 0.14	0.76
A_{2A}AR[I92N]—ZM241385 with Mini-G_S					
1 to 2	100		1.27 ± 0.05		1.91
	86.7 ± 10.2	13.3 ± 1.8	3.73 ± 0.43	0.64 ± 0.04	0.85
2 to 1	100		1.10 ± 0.04		0.5
	81.4 ± 11.6	18.6 ± 5.8	2.27 ± 0.40	0.68 ± 0.08	0.26
2 to 3	100		1.38 ± 0.05		0.84
	97.2 ± 6.3	2.8 ± 5.1	1.52 ± 0.15	0.46 ± 0.35	0.77
3 to 2	100		1.18 ± 0.05		0.71
	95.8 ± 6.5	4.2 ± 4.6	1.39 ± 0.14	0.40 ± 0.18	0.55

Table S16. Mono-exponential and bi-exponential fitting results from the dwell time analysis of A_{2A}AR[D52N] without ligand added (apo) and with ligands in the presence of mini-G_S.

States	A ± sd (%)		k ± sd (1/s)		Reduced χ^2
A_{2A}AR[D52N]—APO with Mini-G_S					
1 to 2	100		0.85 ± 0.04		1.55
	91.9 ± 9.8	8.1 ± 1.3	1.84 ± 0.18	0.28 ± 0.02	0.54
2 to 1	100		1.33 ± 0.05		0.86
	89.8 ± 17.0	10.2 ± 1.5	4.29 ± 0.56	0.72 ± 0.05	0.31
2 to 3	100		1.64 ± 0.13		0.58
	94.4 ± 128	5.6 ± 1.5	8.31 ± 4.31	1.14 ± 0.14	0.18
3 to 2	100		1.73 ± 0.11		0.64
	90.5 ± 224	9.5 ± 2.4	9.62 ± 8.47	1.43 ± 0.16	0.49
A_{2A}AR[D52N]—NECA with Mini-G_S					
1 to 2	100		1.05 ± 0.05		1.84
	93.8 ± 12.6	6.2 ± 0.9	2.35 ± 0.24	0.29 ± 0.02	0.52
2 to 1	100		1.05 ± 0.04		1.14
	84.7 ± 12.7	15.3 ± 3.1	2.76 ± 0.42	0.60 ± 0.05	0.51
2 to 3	100		1.86 ± 0.14		1.17
	91.8 ± 19.8	8.2 ± 7.4	2.92 ± 0.69	0.78 ± 0.29	0.87
3 to 2	100		1.64 ± 0.12		0.8
	90.5 ± 17.7	9.5 ± 7.7	2.63 ± 0.62	0.71 ± 0.24	0.44
A_{2A}AR[D52N]—ZM241385 with Mini-G_S					
1 to 2	100		0.84 ± 0.04		1.98
	91.8 ± 19.8	8.2 ± 1.5	2.79 ± 0.44	0.39 ± 0.04	0.91
2 to 1	100		1.17 ± 0.05		0.97
	91.2 ± 9.2	8.8 ± 3.0	2.02 ± 0.23	0.47 ± 0.07	0.54
2 to 3	100		1.45 ± 0.11		0.56
	94.4 ± 14.9	5.6 ± 7.7	1.91 ± 0.40	0.52 ± 0.31	0.4
3 to 2	100		1.81 ± 0.14		1.07
	92.1 ± 20.9	7.9 ± 4.8	3.03 ± 0.66	0.67 ± 0.18	0.62

Appendix III

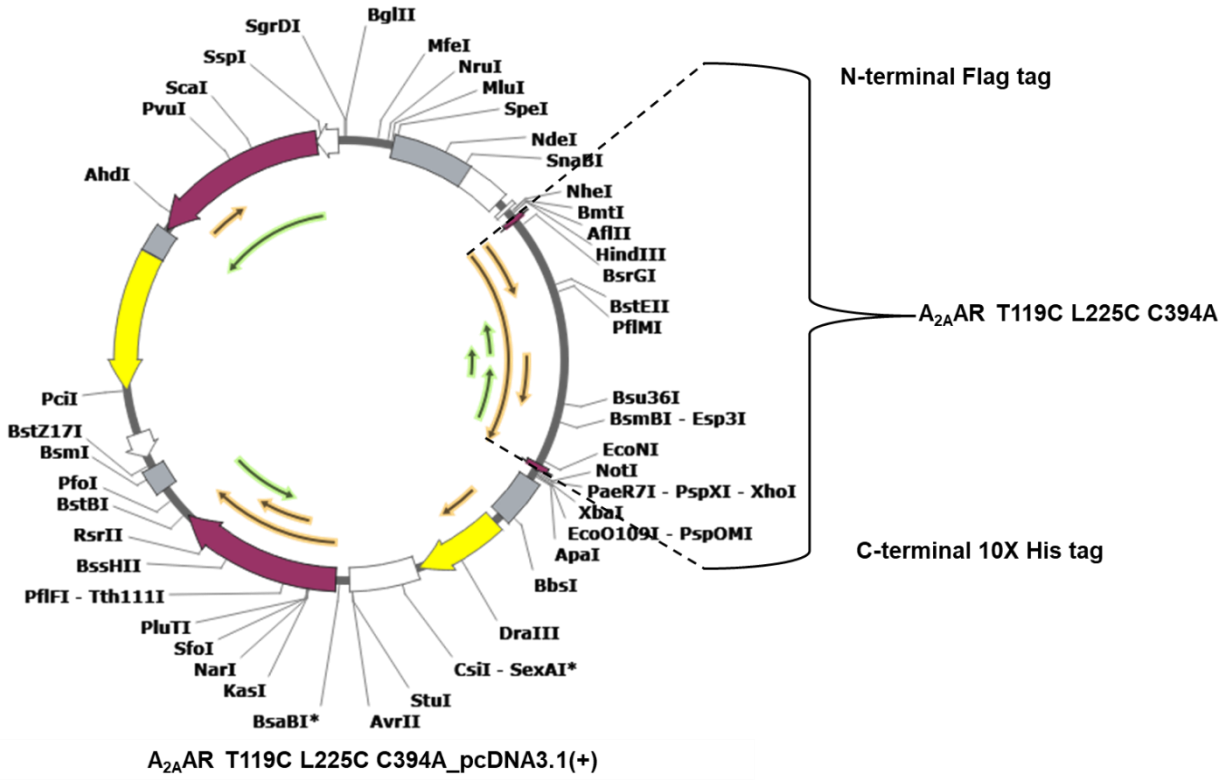

Figure S12. The plasmid map of $A_{2A}AR$ [T119C L225C C394A] in pcDNA3.1(+).

The $A_{2A}AR$ [T119C L225C C394A], with N-terminal Flag tag and C-terminal His tag, is inserted into the high-expression level pcDNA3.1(+) vector for mammalian cell lines. The restriction endonuclease sites for $A_{2A}AR$ insertion are HindIII and NotI.

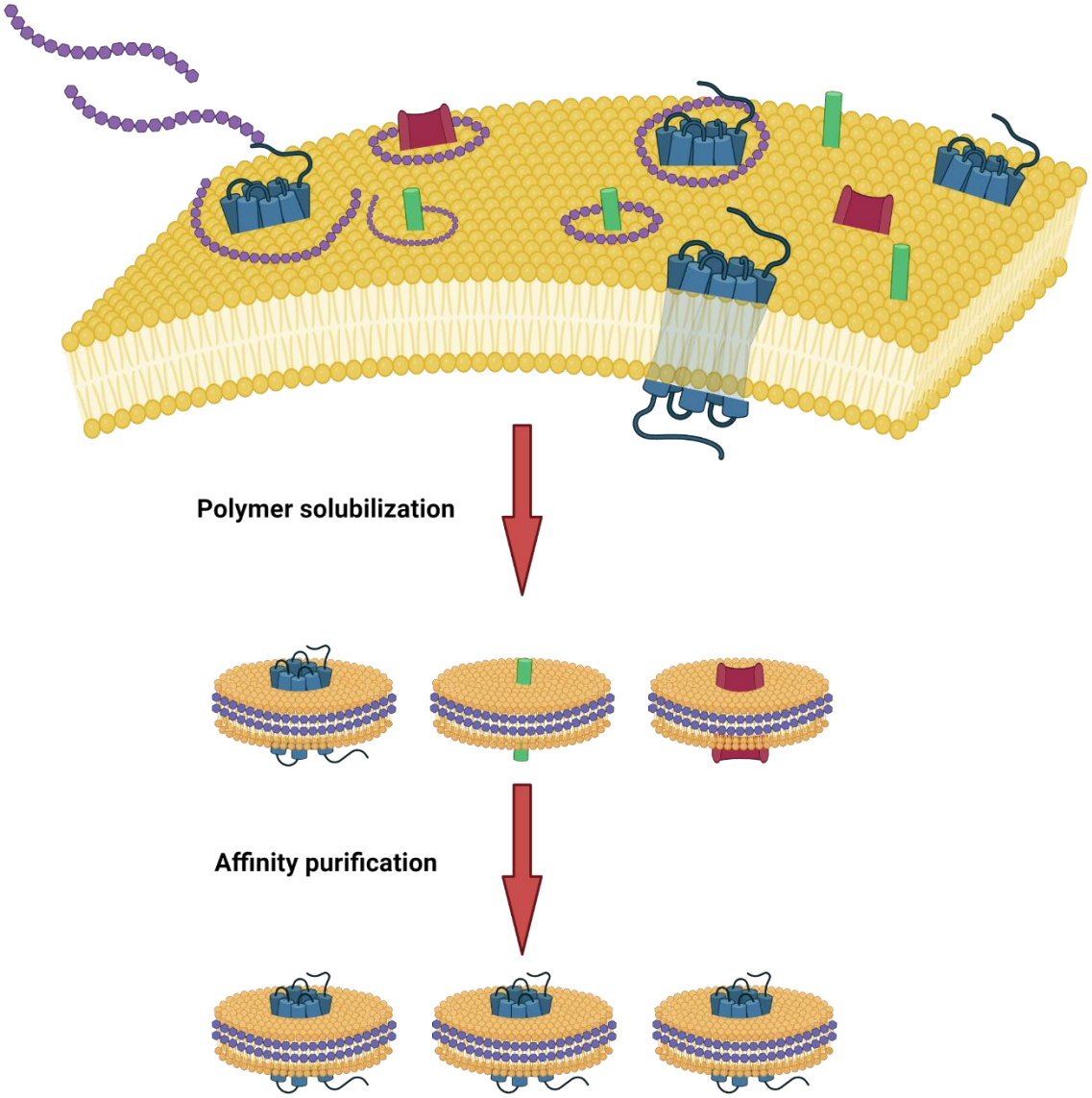

Figure S13. Schematic depicting the process of solubilization, stabilization, and purification of $A_{2A}AR$ in polymer lipid particles (LPs).

Illustration demonstrating how SMA/DIBMA solubilizes membrane proteins from the plasma membrane. The solubilized target membrane proteins, $A_{2A}ARs$ with Flag tag and His tag, are stabilized within polymer LPs, can be selectively purified using affinity binding.

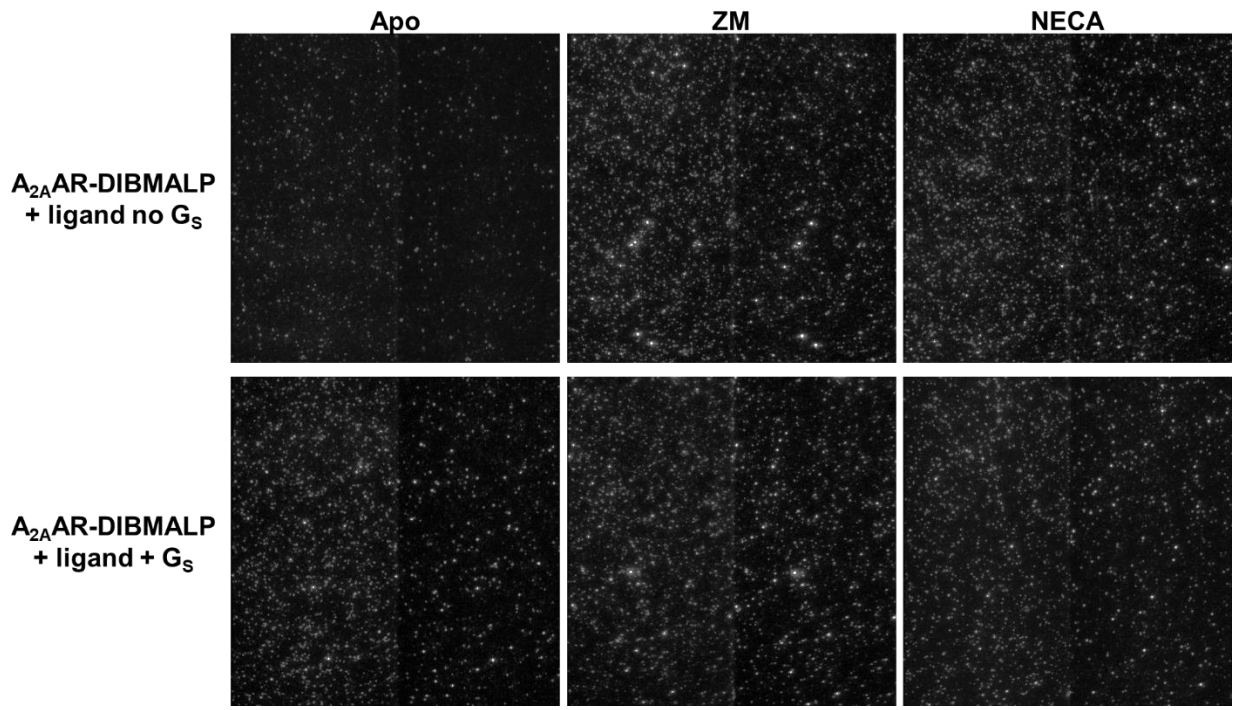

Figure S14. Representative single-molecule TIRF images of labeled A_{2A}AR-DIBMALPs.

Representative TIRF field-of-view images from immobilized labeled A_{2A}AR-DIBMALPs. Each bright spot in the left channel represents fluorescence emission from the donor, Alexa-555. The signal from the right channel represents the acceptor, Alexa-647, which is excited by the donor emission. Notably, super bright spots are aggregates of labeled A_{2A}AR-DIBMALPs.

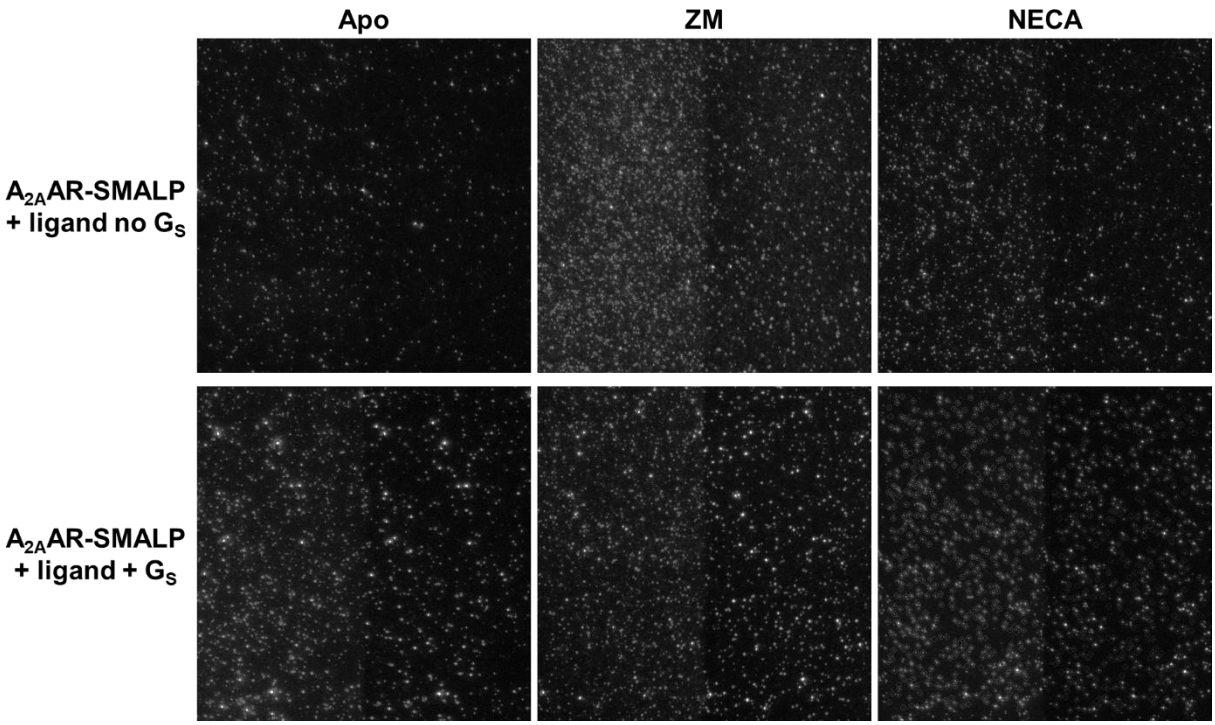

Figure S15. Representative single-molecule TIRF images of labeled A_{2A}AR-SMALPs.

Representative TIRF field-of-view images from immobilized labeled A_{2A}AR-SMALPs. The signal from the left channel represents the donor, while the signal from the right channel represents the acceptor. It should be noted that the significant bright spots observed are aggregates of labeled A_{2A}AR-SMALPs.

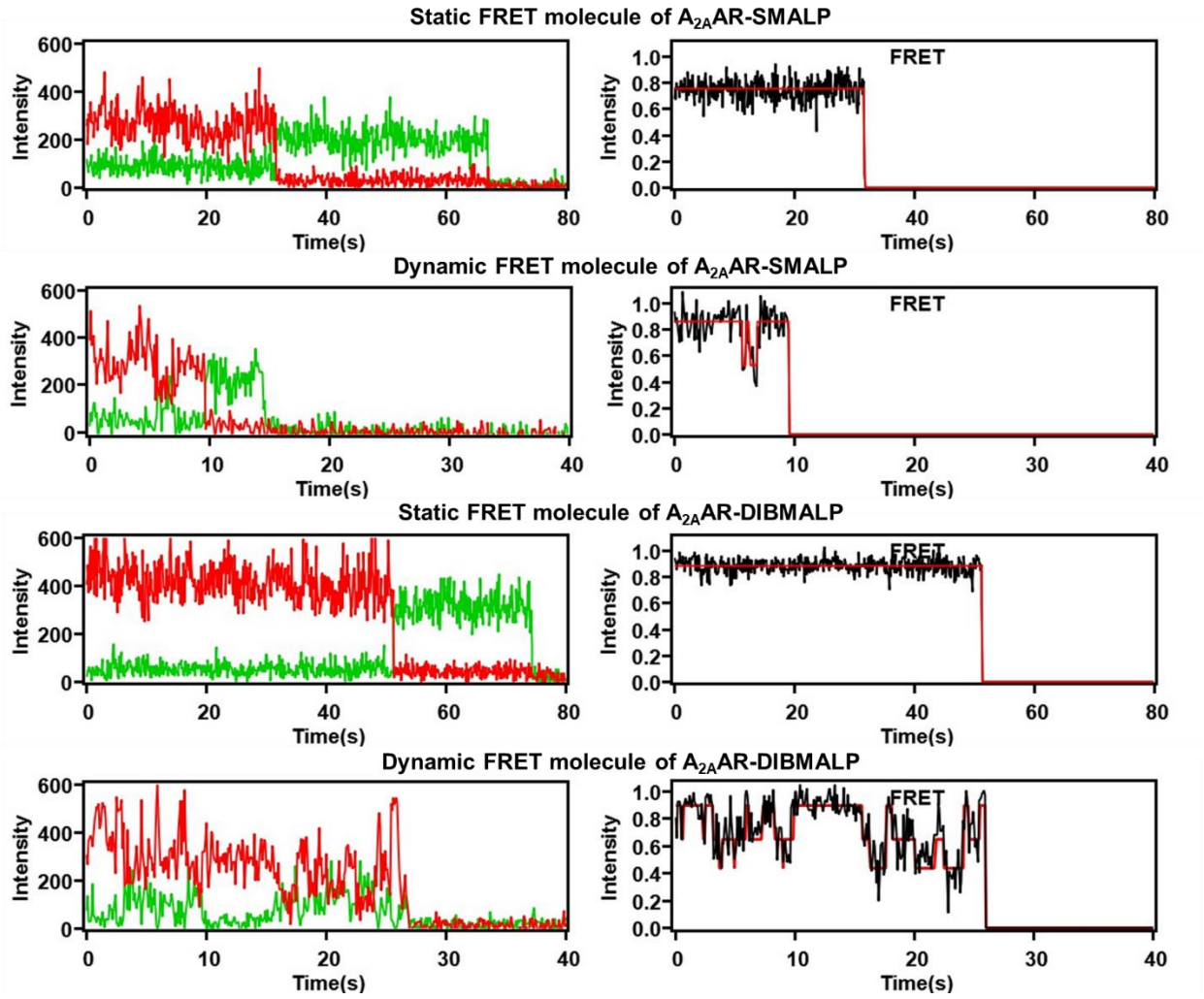

Figure S16. Representative single-molecule FRET traces of A_{2A}AR in polymer LPs.

As indicated in the legends of the figure, shown on the right side are representative static and dynamic FRET traces (black) with hidden Markov model fitting (red). The anti-correlated donor (green) and acceptor (red) trajectories are displayed on the left side.

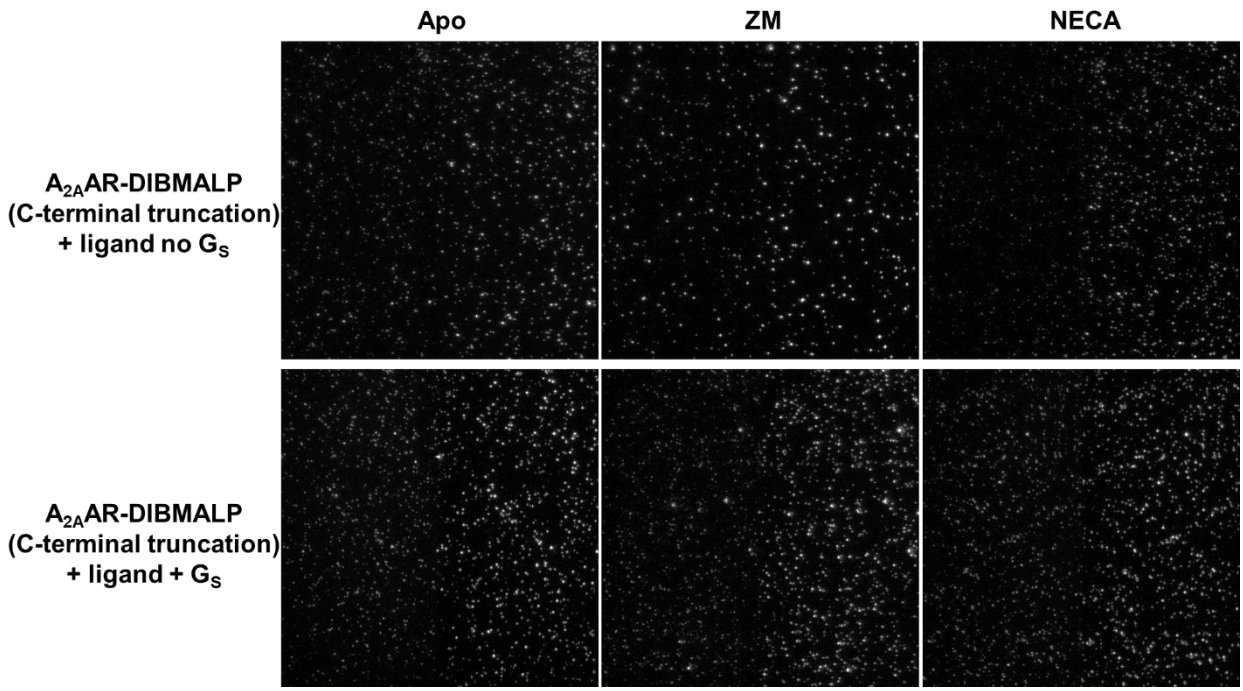

Figure S17. Representative single-molecule TIRF images of labeled C-terminal truncated A_{2A}AR-DIBMALPs.

Representative TIRF field-of-view images from immobilized labeled C-terminal truncated A_{2A}AR-DIBMALPs. The signal from the left channel represents the donor, while the signal from the right channel represents the acceptor. It is observed that aggregates of labeled A_{2A}AR-DIBMALPs still exist.

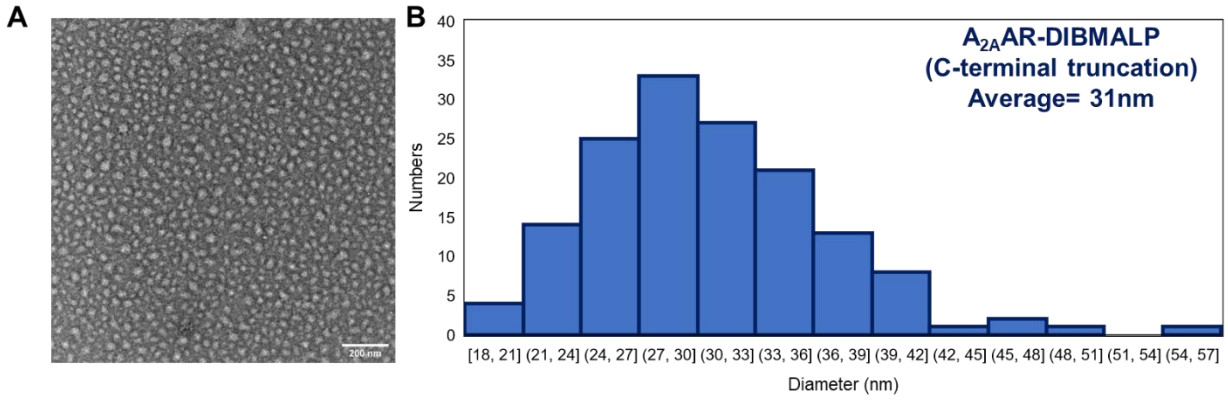

Figure S18. Transmission electron microscopy (TEM) imaging and analysis of C-terminal truncated A_{2A}AR- DIBMALPs size.

(A) TEM image of uranyl acetate-stained C-terminal truncated A_{2A}AR-DIBMALPs. (B) Diameter distribution of C-terminal truncated A_{2A}AR-DIBMALPs, with an average diameter of around 31 nm.

Table S17. Three 5' primers for A_{2A}AR_pcDNA3.1(+) sequencing.

Primer	Sequence
U913NGE200-2-seq1F	AACTACATGGTGTACTTCAA
U913NGE200-2-seq2F	CACGGTCCACATGCCAGAAG
PCDNA3.1F	CTAGAGAACCCACTGCTTAC

VITA

Shushu Wei was born in 1996 in Beijing, China. After graduating from high school in 2014, she attended Jilin University in Jilin province, China, where she obtained a Bachelor's degree in Pharmaceutical Engineering from the Life Science department in 2018. Subsequently, Shushu joined the Ph.D. program in the Biochemistry & Cellular and Molecular Biology (BCMB) department at the University of Tennessee, Knoxville (UTK). During her doctoral studies, Shushu Wei conducted extensive research on the single-molecular-level dynamics of the A_{2A} adenosine receptor, and she had her defense on April 9, 2024.